OSOM: Predictability, Variability, and Response To Parameterizations Quantified Using Information Theory

by

Aakash Bhalchandra Sane

School of Engineering

Brown University

Submitted in partial fulfillment of the requirements

for the Degree of Doctor of Philosophy in the

School of Engineering at Brown University

Providence, Rhode Island, USA

October, 2021

This dissertation by Aakash Bhalchandra Sane is accepted in its present form

by the School of Engineering as satisfying the

dissertation requirement for the degree of Doctor of Philosophy.

Date _____ _____

Dr. Baylor Fox-Kemper, Advisor

Recommended to the Graduate Council

Date _____ _____

Dr. Martin Maxey, Reader

Date _____ _____

Dr. Shreyas Mandre, Reader

Date _____ _____

Dr. Leah Johnson, Reader

Approved by the Graduate Council

Date _____ _____

Dr. Andrew G. Campbell, Dean of the Graduate School

Curriculum Vitae

Aakash Sane completed his bachelor's studies in Aerospace Engineering from the Indian Institute of Space Science and Technology in 2012. He came to Brown University in fall 2015 and obtained his first Master of Science degree from the School of Engineering's Fluids and Thermal Sciences program in May, 2017. Aakash started his doctoral studies at Brown University in 2017 and obtained a second Master of Science degree from Brown University in Earth, Environment, and Planetary Sciences in May, 2021.

Publications:

Sane, A., Fox-Kemper, B., Ullman, D. (2021)."Internal vs Forced Variability metrics for Geophysical Flows using Information theory.", In: *Journal of Climate*, (*submitted*) preprint: https://doi.org/10.1002/essoar.10505545.1

Sane, A., Fox-Kemper, B., Ullman, D., Kincaid, C. (2021) "Consistent Predictability of the Ocean State Ocean Model (OSOM) Using Information Theory and Flushing Timescales." *Journal of Geophysical Research: Oceans* https://doi.org/10.1029/2020JC016875

Sane, A., Mandre, S., & Kim, I. (2018)."Surface tension of flowing soap films." *Journal of Fluid Mechanics*, 841. https://doi.org/10.1017/jfm.2018.28 Article selected for JFM - Focus on Fluids section, May 2018

Barbosa de Castilho, C. J., Fuller, M. E., Sane, A., Liu, J. T. C. (2018). "Nanofluid flow and heat transfer in boundary layers: the influence of concentration diffusion on heat transfer enhancement." *Heat Transfer Engineering*, 1-13. https://doi.org/10.1080/01457632.2018.1442298)

Orenstein, P., Fox-Kemper, B., Johnson, L., Li, Q., and A. Sane, A., Evaluating coupled climate model parameterizations via skill at reproducing the monsoon intraseasonal oscillation. In: *Journal of climate*, (*submitted*)

Awards:

- Co-Principal Investigator, Rhode Island Research Alliance Grant, January 2020
  Project Title: Large Scale Projection Mapping as a Collaborative Platform for Communication and Discourse using Oceanographic data and Physical Modeling of Narragansett Bay.
  Award funding (total): $61,141.39

- Graduate Travel Award, 2017 and 2019, Brown University
- International Travel Award, 2018, Brown University
- Student Academic Career Prep Fund Award, 2021, National Association of Geoscience Teachers

Research Talks:

- Predictability of ROMS-Ocean State Ocean Model using Information Theory: RI NSF EPSCoR Research Symposium, University of Rhode Island. (Invited talk) *April 2021*
- Internal vs Forced Variability metrics for Geophysical Flows using Information theory (On demand, Interactive): Presented at the American Physical Society - Division of Fluid Dynamics (APS-DFD) 73nd Annual Meeting. *November 2020*
- Predictability of ROMS-Ocean State Ocean Model using Information Theory (Poster): Presented at the European Geophysical Union. Meeting, Austria, (online live chat version) *May 2020*
- Predictability of ROMS-Ocean State Ocean Model using Information Theory (Poster): Presented at the Ocean Sciences Meeting, San Diego *February 2020*
- Predictability of ROMS-Ocean State Ocean Model using Information Theory (Talk): Presented at the American Physical Society - Division of Fluid Dynamics (APS-DFD) 72nd Annual Meeting. *November 2019*
- Predictability of ROMS-OSOM (Poster): Presented at Gordon Conference on Coastal Ocean Dynamics *June 2019*
- Predictability of ROMS-OSOM (Poster): Presented at 22nd Conference on Atmospheric and Oceanic Fluid Dynamics *May 2019*
- Air-Sea Interaction in The Bay of Bengal: From Monsoons to Mixing - Workshop held at ICTS, Bangalore *18 Feb-23 Feb 2019*
- Measurement of Surface Tension in a flowing Soap Film: Presented at the American Physical Society - Division of Fluid Dynamics (APS-DFD) 69th Annual Meeting. *November 2017*
- Effective dilution of surfactants due to thinning of the soap film: Presented at the American Physical Society - Division of Fluid Dynamics (APS-DFD) 70th Annual Meeting. *November 2016*

Reviewer:

- Reviewer for the journal: Theoretical and Computational Fluid Dynamics (Springer)
- Expert Reviewer for the First Order Draft of the IPCC Special Report on the Ocean and Cryosphere in a Changing Climate (SROCC).

- Expert Reviewer for the Second Order Draft (SOD) of the Working Group I (WGI) contribution to the Sixth Assessment Report (AR6).

Teaching Experience:

- Teaching Assistant: Introduction to Oceanography (Undergraduate level course) *Feb. - May 2018*
- Teaching assistant: Fluid Mechanics (Graduate level course) *Sept. - Dec. 2018*
- Teaching assistant: Fluid Mechanics (Undergraduate level course) *Sept. - Dec. 2017*

Research Cruise:

- Participated in research cruise as part of the project: "Monsoon Intra-seasonal Oscillations in the Tropical Indian Ocean and the Bay of Bengal (MISO-BOB)" *India, Bay of Bengal, June 3 - 23, 2018*

Acknowledgements

I am grateful to Prof. Baylor Fox-Kemper for being a great mentor and a wonderful advisor. He has been extremely supportive and has shown me that research can be enjoyable. He is also a phenomenal teacher and I consider myself fortunate to have learned geophysical fluids from him.

I want to thank my thesis committee members Drs. Shreyas Mandre, Martin Maxey, and Leah Johnson for helping and giving me advice whenever needed. It is impossible to have a better set of instructors of fluid mechanics than Prof. Martin Maxey and Prof. Shreyas Mandre. Also, thanks to Dr. Dave Ullman for helping with the ROMS package, otherwise my doctoral program would have lasted for one more year.

To all my friends and peers within and outside of Brown University, thank you for making my graduate experience a fulfilling one. I am much obliged to all of my ardent friends, especially Ajit Kanale and Kedar Phadke from my undergraduate college for keeping in touch before and during these worrying times of the pandemic.

I will remain forever indebted to my parents for shaping me into who I am. My achievements lie on the foundations of their sacrifice and hard work. Finally, I was amazed by the patience and endurance displayed by my wife, Manasi, in her attempts to understand my research talks. Her love and support have been paramount for completing my studies.

Abstract

The Ocean State Ocean Model (OSOM) spans the Rhode Island waterways from the Long Island Shelf to the region around Nantucket, including Narragansett Bay, Mt. Hope Bay, major rivers and the Block Island Shelf. In this work, the OSOM has been implemented in the Regional Ocean Modeling System to set up a forecasting system and understand the physical aspects of the regional oceanic circulation. Ensemble simulations have been performed by perturbing the initial conditions of the model. This data, when evaluated with information theory-derived metrics, quantifies the predictability of the OSOM to infer the temporal persistence of anomalies. The predictability timescales informs the effectiveness of a forecasting system and prepare for coupling with biogeochemistry and fishery models with extensively varying timescales. The predictability of the OSOM is $\sim$ 7 to 40 days, varying with parameters, region, and season.

In this work, a new metric is proposed using two quantities from Information Theory - Shannon entropy and Mutual Information - to measure grid point internal and forced variability in ensemble ocean, atmosphere, and climate models. The proposed metric delineates intrinsic and extrinsic variability by measuring the visited probability distribution, as opposed to a variance metric that captures only its second statistical moment. The proposed metric respond to correlated fields, applies to any data without assuming its probability distribution, is insensitive to outliers and changes of units or scale. Additionally, Shannon Entropy and Mutual Information has been applied to measure sensitivity of temperature and salinity affected by modifying the external forcing conditions.

The OSOM has been used to compare three different turbulence models, two of which are standard one- or two-equation models, while the third is a modified one-equation model that

includes effects of a symmetric instability due to horizontal gradients of the buoyancy and Coriolis effects. The results from the two-equation model are the most statistically distant from the other two, as given by the Mutual Information measure, while those from the one-equation models are close. These results suggest that possible SI effects on turbulence parameterization are limited in the present context.

This work highlights Information Theory as a useful tool by demonstrating its use in analyzing outputs from ocean and climate models. These metrics rank the potential impacts of improving boundary forcings, mixing parametrizations and forcing conditions across multiple variables.

Contents

List of Tables

List of Figures

Chapter 1

Introduction

Recently, interest towards regional modelling has been growing due to the relevance of coastal systems and their impacts on our daily lives. As models become sophisticated, questions such as how accurate they are, how far can they predict the future state, how close do they capture variability arise. I apply metrics from information theory on a regional model to answer these questions. The methods described in this text, even though applied to a regional model, are general and can be used on global models. As our primary motivation has been to understand the water bodies in and around Rhode Island our regional model focuses on a particular region of the Northeast coast of the USA.

OSOM is a coastal model implementation of Narragansett Bay and surrounding regions. The region has been modeled to understand various physical and biogeochemical processes and their impact on the health of the bay. In the current chapter, I have explained the basic concepts of information theory for the uninformed reader and Chapter 2 serves as an introduction to OSOM. I relate the various times scales (predictability and flushing timescale) of OSOM and provide a

probable explanation governing the physical process setting the time scales. To find predictability, an ensemble having initial conditions drawn from a single spin up run is compared with an ensemble possessing perturbed initial conditions. The former has been referred as the climatology ensemble and the later as the forecast ensemble. I use information theory to compare the statistical distance between the two ensembles. In Chapter 3, I have derived an information theoretic metric to measure variability in a non-parametric way. The metric was applied to the OSOM ensemble and a global large ensemble climate model dataset to reveal the proportion of intrinsic and extrinsic variability in ensemble models. Along with the metric, Chapter 3 establishes the use of Shannon entropy and mutual information to solve a problem in coastal dynamics: measuring the sensitivity of field variables due to altered or degraded forcing conditions. In Chapter 4, OSOM is realized in CROCO, which stands for Coastal and Regional Ocean COmmunity model (provided by https://www.croco-ocean.org), and I have simulated three vertical mixing schemes to check their level of agreement. Information theory metrics reveal the statistical distances between various physical parameters under the influence of different parameterizations. Chapter 5 concludes the text.

Within the statistical framework of communication theory, ocean model is a communication channel where forcings and initial conditions send “messages" and the observer has to decipher the correct “message" in the presence of noise. We could attribute the noise to the model assumptions or nonlinearities in the governing equations. I use this analogy of ocean model as a communication channel and apply concepts from information theory to analyze predictability and variability of a realistic coastal ocean model of Narragansett Bay and surrounding oceanic regions.

Narragansett Bay becomes hypoxic under detrimental conditions, leading to the prevalence of

oxygen dead zones and fish kills. Physical and biogeochemical factors conducive to hypoxia are poorly understood (Codiga et al., 2009). Rivers transport nutrients (e.g. Nixon et al., 2008) into the bay, leading to eutrophication, a process in which water bodies become enriched with minerals and nutrients. Nutrients lead to algal blooms causing rapid depletion of dissolved oxygen (DO), culminating in dead zones and fish kills. A pathway to restore DO levels at a specific location is to replace the water parcel with oxygen rich DO. Another mechanism is absorbing oxygen through atmosphere and mixing oxygen rich surface water with deep water. On the contrary, stagnant water masses would hinder or delay replacing water parcels while density stratification will prevent mixing. Flushing by river runoff would affect nutrient and DO transport. A detailed hydrodynamic model with high skill is essential which can predict the physical conditions affecting the flushing and mixing. An accurate model would not only be useful for forecasting of physical parameters, but would lead to developments for incorporating biogeochemical modeling. Hence, the Narragansett Bay and surrounding water bodies are modeled using Regional Ocean Modeling System (ROMS) and Coastal and Regional Ocean COmmunity model (CROCO) with a long-term goal of establishing a forecasting system.

An ensemble modeling approach has been used to find the forecasting (predictability) time scales. Finding forecasting timescales of a coastal ocean model with perturbed initial conditions is explained in Chapter 2 and is the first study of its kind. Forecasting timescale is fundamental, as it enables an understanding of the model's predictability limits. The statistical concepts from information theory have been used to find the predictability time scales of a coastal model of the Narragansett Bay. Previous literature on using information theory measures has focused on atmospheric weather prediction. In the present study, I will apply it to a coastal model where I define

predictability as detecting anomaly persistence due to the perturbations in the initial conditions.

Ensemble models show variability because of initial conditions, intrinsic chaos, and external forcings. Predictability is related to variability in the initial conditions, while intrinsic chaos and external forcings govern the variability after forecasting timescales. Chapter 3 highlights estimating variability in ensemble models due to intrinsic factors and extrinsic forcings by using a novel metric devised using known measures from information theory. In the literature, information theory has been used to analyze variability by making parametric assumptions (Gaussian assumptions) about the probability distributions.

I will explain how to understand and estimate variability using non-parametric approaches from information theory. In the analogy of communication channel, intrinsic variability is equivalent to the channel noise. It is an inherent feature of the system arising out of nonlinearities. Extrinsic variability is due to extrinsic forcings. Extrinsic forcings evolve the state variables, similar to changing the sent message. I will explain these concepts in Chapter 3. I will derive a metric using information theory, which estimates intrinsic and extrinsic variability in the unit of bits in the first part of Chapter 3. In the second part of Chapter 3, I have used Shannon entropy and mutual information to compare effects of differences in the external forcings. In coastal models, it is important to understand the sensitivity of physical quantities to the external forcing. For example, does the river runoff from observations give the same upper surface salinity as the time-averaged river runoff? To know this difference, I apply mutual information between the two fields to know the 'cost' of using a degraded river runoff. Mutual information is suitable for such applications because it quantifies the information retained by switching to a different forcing in the unit of bits.

In Chapter 4, the effect of different mixing parameterizations on quantities such as surface

temperature, boundary layer depth, Ertel potential vorticity will be evaluated using well-known concepts from information theory: Shannon entropy and mutual information. This is equivalent to altering the inner workings of a communication channel in order to reduce “noise", that is getting an accurate representation of real world physics in ocean models.

In the current chapter, I have defined the governing equations used in ocean modeling which make up the ‘communication channel’ followed by an introduction to information theory. Predictability, variability, and mixing have been explained subsequently.

1.1 Ocean modelling: primitive equations

The governing equations used to model oceans comprises the Reynolds Averaged Navier-Stokes (RANS) equations. There is always an averaging involved, with RANS being the most common. A detailed derivation of averaging and RANS can be found in any standard graduate level fluids mechanics textbook (e.g. Cushman-Roisin and Beckers, 2011; Kundu et al., 2016). I have summarized the equations with Boussinesq approximations below. The variables u, v, p, ρ are Reynolds averaged quantities. ρ is density perturbation. $\mathbf{u}$ is the velocity vector. Reynolds averaging enables to focus on the temporaly averaged quantities without the need to resolve all the scales.

$$\text{Continuity equation: } \nabla \cdot \mathbf{u} = \mathbf{0} \tag{1.1}$$

$$\text{x - momentum: } \frac{Du}{Dt} - fv = -\frac{1}{\rho_o}\frac{\partial p}{\partial x} + \frac{\partial}{\partial x}\left(\nu_H \frac{\partial u}{\partial x}\right) + \frac{\partial}{\partial y}\left(\nu_H \frac{\partial u}{\partial y}\right) + \frac{\partial}{\partial z}\left(\nu_Z \frac{\partial u}{\partial z}\right) \tag{1.2}$$

$$\text{y - momentum: } \frac{Dv}{Dt} + fu = -\frac{1}{\rho_o}\frac{\partial p}{\partial y} + \frac{\partial}{\partial x}\left(\nu_H \frac{\partial v}{\partial x}\right) + \frac{\partial}{\partial y}\left(\nu_H \frac{\partial v}{\partial y}\right) + \frac{\partial}{\partial z}\left(\nu_Z \frac{\partial v}{\partial z}\right) \tag{1.3}$$

$$\text{z - momentum (hydrostatic) : } 0 = \frac{\partial p}{\partial z} - \rho g \tag{1.4}$$

$$\text{tracer equation: } \frac{D\phi}{Dt} = \frac{\partial}{\partial x}\left(\kappa_H \frac{\partial \phi}{\partial x}\right) + \frac{\partial}{\partial y}\left(\kappa_H \frac{\partial \phi}{\partial y}\right) + \frac{\partial}{\partial z}\left(\kappa_Z \frac{\partial \phi}{\partial z}\right) + F \tag{1.5}$$

$$\rho = \rho\,(T, S) \tag{1.6}$$

x, y are the horizontal coordinates, z is the vertical coordinate, u, v, w are velocities in x, y, z direction respectively, t is time, D/Dt is the material derivative. f is the coriolis parameter given by $f = 2\Omega \sin\theta$, Ω is rotation rate of the Earth in rad/s and θ is the latitude , ρ is density anomaly from a reference density ρ_o and p is pressure anomaly from a reference pressure p_o (Cushman-Roisin and Beckers, 2011). F is the forcing term and is applicable when $\phi = T, S$. Equation 1.6 is the equation of state and provides a linkage between active tracers T, S and the momentum equations. κ is diffusivity and ν is the viscosity and are parameterized to close the

difference equations. The governing equations can be thought of as a 'communication channel' and the channel noise is due to the nonlinear terms in the momentum equations and approximation in turbulence parameterizations. The equations are discretized and the resulting difference equations are solved using numerical techniques. Some of the numerical methods and procedures alongwith boundary conditions for solving them can be found in Cushman-Roisin and Beckers (2011).

1.2 Communication Channel and Information Theory

A communication channel is a medium used for transmitting information. An ocean or atmospheric model was viewed as a communication channel in the work by Leung and North (1990). In communication theory, it is used when an entity A wants to communicate a message to a receiver B using a code such that the usage of the channel is optimized or the effort in communicating is minimized. A typical channel is shown in Figure 1.1. It comprises an encoder, a channel, and a decoder. The encoder converts the message into a set of symbols which can pass through the channel and decoder converts them back into the message. The channel can add noise and the aim of B is to decipher what message A intended to sent. Figure 1.1 shows a sketch of a typical communciation channel shown in information theory texts and Figure 1.2 sketches the anology for an ocean model.

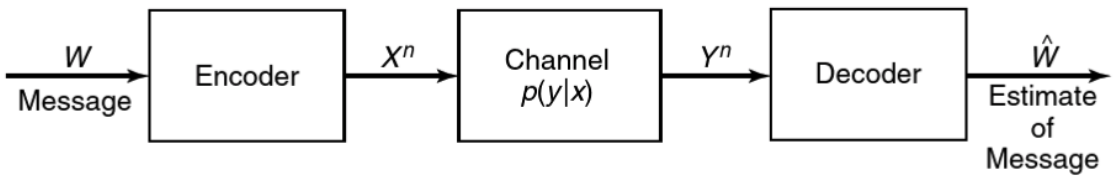

Figure 1.1: Communication channel Cover and Thomas (2012)

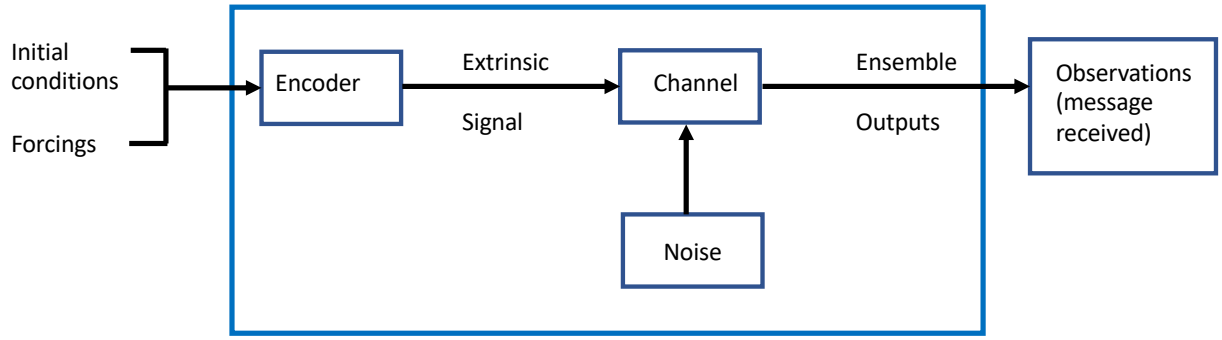

Figure 1.2: Ocean model as a communication channel. Initial conditions and forcings set the trajectory for evolution of model variables. The message (forcings and initial conditions) gets converted to extrinsic signal via the 'encoder'. The channel adds intrinsic noise which might depend on the signal. The observer receives the output. To decipher the "message", the signal has to be transmitted repeatedly to minimize noise. This is equivalent to ensemble modeling, where repeated simulations are performed to get an accurate representation of the processes. This analogy has its limits. In a typical communication channel, the observer has to decipher the correct message sent but in an ocean model, the observer can only guess the extrinsic signal due to repeated experiments and may not reconstruct the forcing fields and initial conditions.

A simple example can be construed which can explain communication channel as well the concept of variability. Let us say that A wants to communicate a single alphabet from the set $X \in (a, b, c, d, e, f, g, h)$ to B using a communication channel which can only send either of two symbols 0 or 1, an unlimited number of times. What would be the shortest length of message for communicating a number, say c, over this communication channel? A simple method would be to send 0 if the number belongs to (a, b, c, d) or 1 if it belongs to (e, f, g, h). Subsequently, 0 if the number belongs to (a, b) or 1 if it is among (c, d). Finally, 0 if it is c and 1 if it is d. Hence, the message sent will be 010. It is known *a-priori* by B that A can send any of the numbers with equal probability of 0.125.

0				1			
0		1		0		1	
0	1	0	1	0	1	0	1
a	b	c	d	e	f	g	h

Table 1.1: Coding for the set $a, b, c...h$. To send any letter, two symbols are required: 0 or 1. A sequence requiring only three symbols is needed to be sent to send one letter. In other words, the receiver needs three symbols (or three bits) to decipher the message. Two symbols implies logarithm to the base 2 is used in entropy evaluations.

Table 1.1 visualizes this procedure. Hence we need to send a message of 3 characters to convey a single letter out of 8. If we were playing a game of twenty questions, we would need 3 questions to obtain the right answer. For our communication system, we need exactly 3 units to convey every letter without ambiguities, so 3 characters contain *information* about the entire set. Three selections (010) of the two symbols(0,1) are required to convey a letter out of 2^3 possibilities. A natural question is can we quantify information in a set of possibilities and if yes, what is the right measure for it.

Hartley (1928) identified the logarithm function as a measure of information. If there are N objects in a set and all are equally probable in their occurrence, then the amount of information is given by $\log_2 N$. When base is 2, the information is in the unit of bits, standing for binary digits as termed by J. W. Tukey (Shannon, 1948). The meaning of the term information is not knowledge that we gain by reading a text or interacting with any media, but it means information we gain when one message is received among several possibilities. Hartley's measure assumed that all the objects have equal probability, that is the N elements belong to a uniform distribution and each element i has probability $p_i = 1/N$. Hence, as per Hartley, the information gained after an outcome having probability p_i is $\log N = \log(1/p_i)$. Claude E. Shannon in his classic paper of 1948 (Shannon, 1948) generalized it for any probability distribution. The Information content $h(x)$ in an outcome x having probability $p(x)$ is given by (Cover and Thomas, 2012)

$$h(x) = \log_2 \frac{1}{p(x)}, \tag{1.7}$$

this is informtion gained by knowing x. As per Shannon, the average information content in all the

elements x_i belonging to the set x is given by

$$H(x) = \sum_i p(x_i) \log_2 \frac{1}{p(x_i)}. \tag{1.8}$$

Shannon's article (Shannon, 1948) states the properties required by a measure of information or uncertainty and gives proof that equation 1.8 is the only qualifying measure.

Usually in the information theory literature the term $H(x)$ is written as $H(x) = -\sum_{i=1}^{N} p(x_i) \log_2 p(x_i)$ but I will use $\log_2 (1/p(x_i))$ as it is more intuitive and avoids any ambiguity because of the negative sign. $H(x)$ is the average amount of bits required to convey an element x over repeated use of the communication channel. For the receiver B, before A sent a message, B had some uncertainty as to what would be the message. After B has received the message, the uncertainty was reduced by an amount $H(x)$. B needs $H(x)$ bits to decode the message accurately or with some error due to channel noise.

The average information entropy $H(x)$, will be referred as entropy. It should not be confused with the entropy used in statistical thermodynamics. The term $\log_2 (1/p(x_i))$ can be interpreted in various ways. The term $\log_2 (1/p(x_i))$ measures the uncertainty in the sense that high probability events have low uncertainty because there is a high chance they will occur. Low probability events have higher uncertainty as they might not occur at all. The prefix $p(x)$ weighs the information in x with its probability. Higher probability events are given more weight than lower probability events because the former occur more than the later.

Once a low probability event has passed, we gain a lot of information. The entropy term also measures the amount of surprise. Higher probability events cause lesser surprise than low

probability events. There are multiple interpretations of $H(x)$. It can be thought as uncertainty, or certainty. Entropy can also be considered as freedom, measurement of disorder, lack of information and gain of information simultaneously. Brissaud (2005) has given the various interpretations of Shannon entropy. An interpretation of Shannon entropy is that of freedom. Shannon entropy describes how much freedom a variable has in occupying any of its possible "states". For example, in the set X considered earlier, the variable x could take any of the alphabets from a to h. Hence, x was free to take any of the 8 states or it required 3 bits to specify the amount of states it can occupy. For a fresh set Y which consists of only two letters a and b, it would require 1 bit to specify y or there would be 2^1 states that y could take. We can easily see that x has more variability than y.

Traditionally, variability has been thought of as how much spread exists in the underlying data. This has led to the second statistical moment, variance, for measuring the variability. Variance is defined as the expectation of the square of deviation of a variable from its mean value. Although variance estimation requires knowledge of probabilities, it is convenient to use arithmetic variance, which only uses the value. Existing literature is abundant in using arithmetic variance because of its ease of use. There are multiple downsides of using variance or arithmetic variance such as outliers get more weight, clustering of values is neglected, only Gaussian distribution is favored. Estimating variability by using Shannon entropy avoids these pitfalls.

Variability is an important interpretation of Shannon entropy as it can be used to estimate variability in a non parametric way. Carcassi et al. (2019) has detailed how Shannon entropy characterizes variability for data sets which are *non Euclidean*. In the example explained in Table 1.1, Shannon entropy measures variability of the set X. The letters contained in X can be replaced with temperature over the city of Providence to obtain its variability. Each letter in X can

be thought of as a range of temperature for example, $a \in [0, 5], b \in [5, 10], ...h \in [35, 40]$ with equal probabilities for all alphabets. As the temperature can fall into any of the 8 bins with equal probability, the variability measured using Shannon entropy is 3 bits. In other words, 3 bits are required to pinpoint the temperature value from the whole range of possibilities. Shannon entropy is the average number of bits required to go from the collection of objects to a particular object. Inversely, Shannon entropy is the number of bits of freedom required to attain any of the possible states.

A second important term presented by Shannon is mutual information. Mutual information involves comparison between two variables $x \in X$ and $y \in Y$. For discrete probability distributions, it is given by

$$I(X;Y) = \sum_{i=1}^{N} \sum_{j=1}^{N} p\left(x_i, y_j\right) \log_2 \left(\frac{p\left(x_i, y_j\right)}{p\left(x_i\right) p\left(y_j\right)} \right) \tag{1.9}$$

Mutual information is the common information or common (un)certainty between two variables. It is the information that the observer receives on average about the sent messages in the presence (or absence) of noise. This can be demonstrated using the previous example where A communicates with B with the channel adding noise. Figure 1.3 shows joint distribution between messages sent (set X) and messages received (set Y). Each symbol was sent 100 times over the communication channel. For example, the symbol f was sent, but the channel added noise and instead of sending f correctly 100 times, it sent f 50 times and e 50 times. The Shannon entropy of choosing f is 3 bits, given by the sequence 101. The receiver did not know *a-priori* that f was sent. The receiver only sees 100 or 101 corresponding to e or f with equal probability. Only the

first two symbols 10 are common to 100 and 101, and the third symbol, which is either 0 or 1, must be due to the channel noise. Hence, the pointwise mutual information for this particular example is 2 bits. Adding and averaging all the pointwise mutual information for all the elements gives the mutual information of this communication channel.

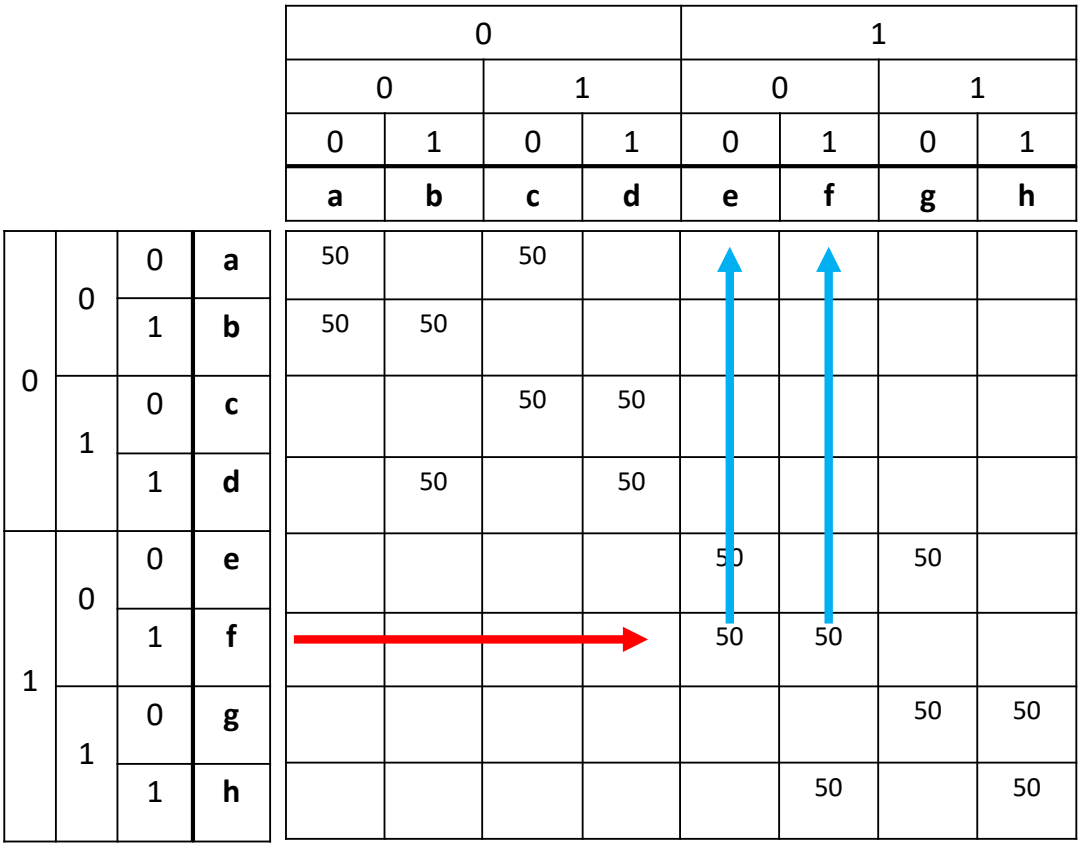

Figure 1.3: Joint distribution of events shown on the left margin and their observations through a noisy communication channel shown at the top margin. Each event a to h occurs 100 times and is correctly sent 50 times. When f is sent (101), either e or f are received given by (100) or (101). The first two bits are correct and third bit is noise. This gives the pairwise mutual information as 2 bits and noise as 1 bits. As soon as e or f is received by the receiver, the receiver gets 2 bits of information about the message sent. The diagonal represents error free transmission and off diagional elements represent noise for this case.

1.3 Estimating entropies

Estimating Shannon entropy and mutual information is not straightforward. Information entropies are sensitive to binning because binning is equivalent to accuracy of measurement. For example, a thermometer measuring temperature with an accuracy of $\pm 1^{\circ}C$ will have higher uncertainty than a thermometer having an accuracy $\pm 0.1^{\circ}C$. Difficulty arises in estimating the probability distributions from the raw data. Throughout this thesis, entropies are estimated by using discrete probability distributions obtained by binning the raw data. This approach is called the histogram approach and is the most common approach. Using histogram binning approach causes biases in estimating Shannon entropy and mutual information (Papana and Kugiumtzis, 2008). Throughout this manuscript, I have employed equidistant partitioning to estimate probability distributions from raw data. Work here involves comparing the value of entropies between two time series or grid points. As the binning has been kept consistent for the time series data (or spatially varying data), the biases in estimating entropy won't affect the qualitative interpretation of the results. Wherever it is important to quantify entropies, sensitivity to binning has been checked and reported.

1.4 Predictability and Variability

The variability observed in an ocean model is due to three factors: differences in initial conditions, external forcings (atmospheric, tidal, etc.), and intrinsic chaos due to the non-linear and chaotic nature of fluid flow. In phase space, the state moves along a trajectory whose trend is determined by initial conditions, forcings, and variability. With no dissipation and external forcing, the trajectory would remain confined because of an invariance, say E, of energy conservation (Lorenz,

1963). Due to intrinsic chaos, two initial conditions which are very close in the phase space would separate after some time scale as observed in the Lorenz system of equations (Lorenz, 1963) but would still be on the surfaces of constant E. This time scale is the predictability time scale τ. Within this time scale, the initial conditions dominate variability. When forcing is introduced, the trajectory will change to a different E and in case of strong damping due to high diffusivities, DE/Dt will be negative lowering E leading to a change in the trajectory. In coastal models, this damping is usually observed to be very strong and hence, unlike the Lorenz system, even a large anomaly in the initial conditions will cause the trajectories to get attracted towards paths that are same as those with relatively small perturbations. ROMS-OSOM shows this kind of predictability in which an anomaly, small or large, in the initial conditions decays with the same time scale τ depending on region of the estuary and season (winter or summer). Beyond the predictability time scale τ, the forecast ensembles merge with the climatology ensembles, implying the trajectories in phase space of forecast ensembles forget about the anomaly in the initial conditions. After time τ, there is no extra information in forecast ensembles than there is in climatology ensembles and it is futile to run the forecast simulations because they yield the same output with same information as that in climatology.

In the literature, idealized studies have been performed and predictability time scales have been found using the information theory metric (e.g. Kleeman, 2002). The idealized studies are not expensive and can have large number of ensemble members. In realistic regional models like OSOM, it is not possible to have large ensemble members to obtain probability distribution from state vector of individual members. To circumvent this issue, a running window approach was utilized which allowed wider sampling. In the running window, the Shannon entropy $H(X)$

of the values of model mean of climatology members (MCM) was found. This was compared with the mutual information $I(X;Y)$ between MCM and the values of the model member for the forecast ensemble within that running window. $I(X;Y)$ between forecast and climatology measures how much information is shared between the time series with the anomaly and the time series without the anomaly. Lower $I(X;Y)$ implies the forecast shows independence from climatology. $H(X) - I(X,Y)$ measures how many bits are needed to close the gap between the forecast and the climatology. After time τ, $I(X;Y)$ shows higher values implying that the forecast is statistically similar to climatology marking the end of the predictability period and start of the projections period. The running window approach, even though approximate, mitigates the lack of large number of ensemble members.

Generally, strong damping occurs in coastal models and the ocean flow represented by ROMS-OSOM displayes low to modest chaos. This is because the lateral diffusivities in ROMS are large, which give rise to less chaotic tracer fields (temperature, salinity). If an anomaly gets introduced, say a perturbation in the state vector, the perturbation can diminish due to two reasons: (1) Intrinsic variability (chaos) will cause the anomaly to mix and dissipate (2) the anomaly will flush out of the boundaries. As the intrinsic chaos is low, the most plausible explanation for reduction of anomaly is the flushing mechanism of the bay. The time scale associated with flushing mechanism is the flushing time scale and is given by V/Q where V is the volume of the quantity under consideration and Q is the flux of the quantity. The flushing time scale is estimated easily, though it requires accurate knowledge of the volume and fluxes. It is a physical property of the estuary unlike a predictability time scale which is a feature of the numerical ocean model. As the predictability time scale might be governed by flushing of the anomaly, the connection between these two time

scales has been explored in Chapter 2.

Once the predictability time scale τ passes, the variability is set only due to intrinsic and extrinsic factors and is the focus of Chapter 3. An information theory based metric has been proposed to estimate the relative contributions of intrinsic and extrinsic variability. The metric uses Shannon entropy and mutual information. In addition to applying it here to the OSOM ensemble, it has been applied to idealized random vectors and ensemble simulation output from the GFDL-ESM2M large ensemble (Rodgers et al., 2015; Deser et al., 2020).

1.5 Mixing parametrizations

Mixing is a process in which different fluid parcels mix with each other. To accurately understand and predict the physical processes, it is pertinent to have the correct parameterizations. Mixing can be because of molecular diffusion or tubulent eddy mixing, the later being the dominant one. Parameterizing the effects of turbulent mixing is required because the model resolution limits the scales at which processes can be resolved. Mixing will occur along both horizontal and vertical directions and is represented by the viscous and diffusive (ν and κ) terms in Equations 1.2 - 1.6. The subscript H terms of nu, κ are associated with horizontal mixing and the subscript Z terms with vertical mixing. In ROMS, the lateral mixing eddy viscosity and diffusivity terms are set as constant values and numerical discretization schemes cause large numerical viscosities. In geophysical models, the aspect ratio (ratio of vertical length scale of motion to horizontal scale of motion) is very small and this leads to higher vertical velocity shear as compared to horizontal shears (Cushman-Roisin and Beckers, 2011). This simplifies the turbulence models as turbulent eddy viscosity/diffusion is predominantly in the vertical direction.

Diapycnal mixing, mostly vertical, causes exchange between the surface parcels and the water column beneath it. This exchange can be of water mass, temperature, salinity, or any other active or passive tracer. For example, wind driven cooling during nighttime will cause the formation of a cold layer at the surface and the cold parcels will sink because of buoyancy loss. ROMS-OSOM uses the General Lenght Scheme (GLS) to represent mixing. As will be shown in Chapter 2, GLS scheme works with reasonable accuracy and model matches observational data from buoys. To check sensitivity of different schemes, OSOM was modelled using CROCO and compared by activating GLS scheme (Umlauf and Burchard, 2003), KPP scheme (Large et al., 1994), and modifed KPP scheme. The modified KPP scheme paramterizes the effects of symmetric instability (Bachman et al., 2017) (hereby called SI scheme). The physical processes observed in all the three simulations of CROCO-OSOM should be the same, but the results show otherwise. Metrics from information theory have been used to quantify these differences. Shannon entropy and mutual information are well suited for the comparison because they capture all the correlations. Information theory metrics capture the amount of common information or missing information in two data sets. For example, if the mutual information between GLS and KPP is less than between KPP and SI for surface temperature, it indicates the extent of information lost when using GLS over KPP. The scheme details (in brief), methodology to compare the three simulations, and results have been described in Chapter 4.

Chapter 2

Predictability

Preface to Chapter 2

Chapter 2 is a verbatim version of a manuscript accepted in the Journal of Geophysical Research-Oceans (Sane, Fox-Kemper, Ullman, Kincaid, and Rothstein, Sane et al.). The title of the submitted article is: "Consistent Predictability of the Ocean State Ocean Model (OSOM) using Information Theory and Flushing Timescales". The authors of the manuscript are: Aakash Sane, Baylor Fox-Kemper, Dave Ullman, Christopher Kincaid, Lewis Rothstein. AS and BFK are affiliated with Brown University and DU, CK, and LR are affiliated with University of Rhode Island. The manuscript can be found at the permanent DOI: https://doi.org/10.1029/2020JC016875.

DU was involved in setting up the initial model: creating forcing and grid files and evaluating the performance of model with respect to observations. CK and LR were involved with the earlier version of OSOM. AS and BFK contributed in setting up ensemble runs, applying information

theoretic metric and writing the manuscript. AS applied the total exchange flow formulation to find the flushing time scales.

Abstract

The Ocean State Ocean Model OSOM is an application of the Regional Ocean Modeling System spanning the Rhode Island waterways, including Narragansett Bay, Mt. Hope Bay, larger rivers, and the Block Island Shelf circulation from Long Island to Nantucket. This paper discusses the physical aspects of the estuary (Narragansett and Mount Hope Bays and larger rivers) to evaluate physical circulation predictability. This estimate is intended to help decide if a forecast and prediction system is warranted, to prepare for coupling with biogeochemistry and fisheries models with widely disparate timescales, and to find the spin-up time needed to establish the climatological circulation of the region. Perturbed initial condition ensemble simulations are combined with metrics from information theory to quantify the predictability of the OSOM forecast system–i.e., how long anomalies from different initial conditions persist. The predictability timescale in this model agrees with readily estimable timescales such as the freshwater flushing timescale evaluated using the total exchange flow (TEF) framework, indicating that the estuarine dynamics rather than chaotic transport is the dominant model behavior limiting predictions. The predictability of the OSOM is ~7 to 40 days, varying with parameters, region, and season.

Plain Language Summary

A new model of waterways near Rhode Island is introduced and examined. The model is intended for studying the physical circulation of this region and its ecosystem changes. This study uses a variety of metrics to assess for how long a forecast with this model might be useful (i.e., how long the model's initial state determines its behavior) and relatedly how long to run (or spin up) the model to have poorly known initial conditions not affect the result systematically.

2.1 Introduction

Coastal marine forecast systems are in use or development in a number of regions worldwide (e.g. Wilkin et al., 2018; Moore et al., 2011; Lellouche et al., 2018; Pinardi and Coppini, 2010; Mel and Lionello, 2014; Raboudi et al., 2019). As each region is unique, the length of forecast window and relative levels of forced to internal variability differ among these systems. The Ocean State Ocean Model (OSOM) is a new model in development, which is an extension and synthesis of past prototype models (Bergondo, 2004; Bergondo and Kincaid, 2007; Liu et al., 2016; Wertman, 2018; Ullman, 2019; McManus et al., 2020) being evaluated for potential use as a forecast system. In this evaluation, key questions are: How often should a forecast be made? How far into the future can forecasts be skillful? How long does the model take to spin up? How accurate must surface and boundary forcing be to arrive at useful forecasts, given that these data would also be predictions (e.g., from numerical weather prediction models)? Which regional societal challenges are better framed as changes to the region's climatology (i.e., projections) rather than as predictable futures that depend on the model's initial conditions (i.e., forecasts)? In this paper, a framework for addressing these questions is developed by adapting methods from information theory and ensemble-based

measures of predictability, internal variability, and forced variability. The OSOM is taken as a test example of these methods and, as a coastal model in development with unique characteristics, the specific results of this study are useful for the future development of this particular model.

Forecasting hydrodynamic parameters is pertinent for an estuary as they play a vital role in controlling the physical as well as biogeochemical changes. An important aspect of forecasting is finding the predictability/forecasting timescales that limit the degree to which initial conditions govern the future behavior of the numerical model for individual parameters. These timescales quantify the persistence of anomalies and are a feature of the numerical model. Predictability is a measure of a model's ability to forecast or predict the evolution of anomalies in the future from initial conditions given prescribed external forcing. By contrast, changing forcing due to climate change (e.g., Xiu et al., 2018), altered topography via erosion or dredging (Hayward et al., 2018), changes to wastewater treatment or power plant effluent (Mustard et al., 1999), etc., are *external* factors affecting boundary conditions rather than initial conditions whose impact can be assessed using *projections* of future climatology with altered boundary conditions over a variety of plausible initial conditions. Thus, *predictability* measures a model's potential to *predict* or *forecast* a future state which is distinct from climatology, which is distinct from *projecting* the changes to climatology forced from changes to boundary conditions. The state of the system in a forecast can be only considered in a probabilistic way and hence predictability is a property involving two distributions (DelSole, 2004): predictability quantifies the departure of a forecast distribution from the climatology distribution (Shukla, 1981; Leung and North, 1990). Quantifying this departure involves measurement of uncertainty in the forecast signal. The uncertainties in the initial conditions can be thought of as anomalies which eventually are forgotten by the model, or

overwhelmed by chaotic variability or the influence of boundary conditions as time proceeds until the forecast statistical distribution becomes indistinguishable from the climatology distribution. Beyond this time scale a forecast provides no additional information beyond climatology, and forecasts are then no more useful than projections of the future climatological range of possibilities.

This article has three purposes: (1) To describe the OSOM; (2) To use ensemble simulations to find predictability timescales; (3) To find estuarine flushing timescales for fresh and saline water masses and compare these to (2). The model is forced by winds, tides, river runoff, evaporation, precipitation and also forced by heat fluxes and open boundary conditions. So, unlike the numerical weather prediction models for which the information theory techniques applied here were developed, the OSOM is a forced model where much of the variability comes from external forcing that may determine the trend of the evolution of the state parameters, or alternatively internal variability (e.g., hydrodynamic instabilities and chaos) may dominate. A companion paper in review by Sane et al., 2021 develops a non-parametric information theory approach to quantifying the amount of internal vs. forced variability similar to the ensemble approach of (Llovel et al., 2018), and uses this metric to quantify the relative importance of different choices in boundary forcing. As the balance of sources of variability depends on forcing, resolution, classes of flow, etc., the magnitude of the forced vs. intrinsic variability depends on the specifics of the model, rather than being a general description of the waterways under study. So, too, do the predictability metrics describe the specific model being studied rather than the system. However, here a comparison to traditional estuarine flushing timescales serves to illustrate that the model is governed by physical principles, so quantifying these based on the real–rather than simulated–world may nonetheless be useful in establishing physical guidelines underlying limits on predictability.

Metrics from information theory provide a natural way of quantifying distances between two probability distributions (Cover and Thomas, 2012). Information theory metrics have been used in myriad ways in other fields (e.g., electronic communications, image processing, and molecular biology). Using information theory metrics for weather prediction and climate projection is well established (Leung and North, 1990; Schneider and Griffies, 1999; Roulston and Smith, 2002; Kleeman, 2002; DelSole, 2004; Haven et al., 2005), but they are not commonly used in coastal modeling. DelSole (2004) relates the requirement to quantify uncertainty with the usage of metrics from information theory. The most commonly used metrics are entropy, relative entropy, and mutual information (Shannon, 1948), although other variants are also useful (Kleeman, 2002; Leung and North, 1990). A key advantage for use of these metrics in coastal modeling is that they can be ascribed to a variety of physical or biogeochemical variables; here we examine salinity, temperature, and kinetic energy over regions and at observation locations, but in future work we will examine biogeochemical variables in the OSOM.

An important time scale for an estuary is the flushing time scale (Knudsen, 1900), which is defined as the average time of a parcel of fluid inside the estuary (e.g., Monsen et al., 2002), and thus also the average retention time of water masses in the estuary. As the numerical model represents the physical domain, there is an inherent relation between the forecasting timescales and the flushing time scale, because eventually tracer anomalies present in the initial conditions will be flushed from the estuary, and the flushing timescale is an estimate of how long this process will take (assuming the anomalies are conserved on each water parcel). Here these timescales are found for the OSOM, a model developed specifically for Narragansett Bay and connected waterways.

Narragansett Bay (NB) is a medium-sized estuary and a natural harbor. As per the classification

of estuaries based on physical and hydrological attributes, NB is a class 8 estuary (a moderate area, volume, and freshwater flow estuary that is deep and salty: Engle et al., 2007). It is a prime example of a coastal plain estuary, also known as a drowned river valley, which is the most common type of estuary in temperate climates. In winter, it is mostly a well-mixed estuary. In summer, it is a partially-mixed estuary. The bay covers an area of $\sim$ 400 km^2 (Pilson, 1985). It is 16 km wide (East-West), 32 km long (North-South), and has 412 km of shoreline. The Bay extends from the Providence and Seekonk rivers in the north to Rhode Island Sound in the South. To the east, it connects to Mount Hope Bay, fed by the Taunton River and connected by the Sakonnet River to Rhode Island Sound. The whole of the Narragansett Bay, Mount Hope Bay, associated rivers, and Rhode Island Sound is simulated in OSOM (Figure 2.1), but the emphasis in this paper is variables within NB and Mount Hope Bay. The average depth of NB is 8 m and the deepest point is 60 m. The bathymetry varies with steep slopes in the Rhode Island Sound towards the open ocean and along the dredged navigation channels. The Bay provides a natural habitat for many living things and is of commercial and ecological importance to the local community. Commercial fishing and shell fishing are important economic activities and the Bay has also been used for recreational sports such as a harbor for the America's Cup and the Volvo Ocean Race sailing competitions. Recently pollution has impacted these activities; bacteria and viruses have caused beach closures, harmful algal blooms, and shell fishing bans, and hypoxia is frequent and sometimes induces large fish kills. OSOM will be used to simulate the physics of the Bay and predict the physical and biogeochemical conditions conducive to these events, as well as to assess the impact of different management and mitigation practices. The predictability timescales studied here help reveal the utility of the model to forecast the physical conditions for harmful events.

This article has been structured as follows: Section 2 provides detail of the computational model OSOM. Section 3 describes the theory of using mutual information to find predictability timescales. Section 4 contains the ensemble simulation setup for forecasting and climatology sets. Application of mutual information to the ensembles has also been described in Section 4. Section 5 states the results for various cases and also gives the flushing timescales obtained via OSOM.

2.2 Ocean State Ocean Model

The Ocean State Ocean Model (OSOM) is an application of the Regional Oceanic Modelling System - ROMS (Shchepetkin and McWilliams, 2005). The curvilinear terrain-following coordinate system employed in ROMS is well suited for coastal applications since the bathymetric variations in coastal systems and estuaries are large. The model has curvilinear varying horizontal resolution as well, from $\sim$ 50 m towards the north to around 200 m in the south of the modelled domain. The horizontal grid consists of 1000×1100 grid cells and 15 terrain-following sigma levels in the vertical. The Generic Length Scale (GLS) scheme (Umlauf and Burchard, 2003), with parameters chosen for the $\kappa - \epsilon$ closure (Warner et al., 2005a), is used to represent unresolved turbulence. Salinity and temperature have been evolved using 'Multidimensional Positive Definite Advection Transport Algorithm' known as MPDATA in ROMS (for example Kalra et al., 2019).

The offshore forcing at the open boundaries is provided by surface elevation and depth-averaged velocity using 9 tidal constituents (M2, S2, N2, K2, K1, O1, Q1, M4, M6) from the eastcoast tidal constituent database (Mukai et al., 2002) and, at subtidal timescales, with low-pass filtered output of the hindcast version of the Northeast Coastal Ocean Forecast System (NECOFS), a regional model covering the northeast U. S. coastal ocean (Beardsley and Chen, 2014). The surface elevation and

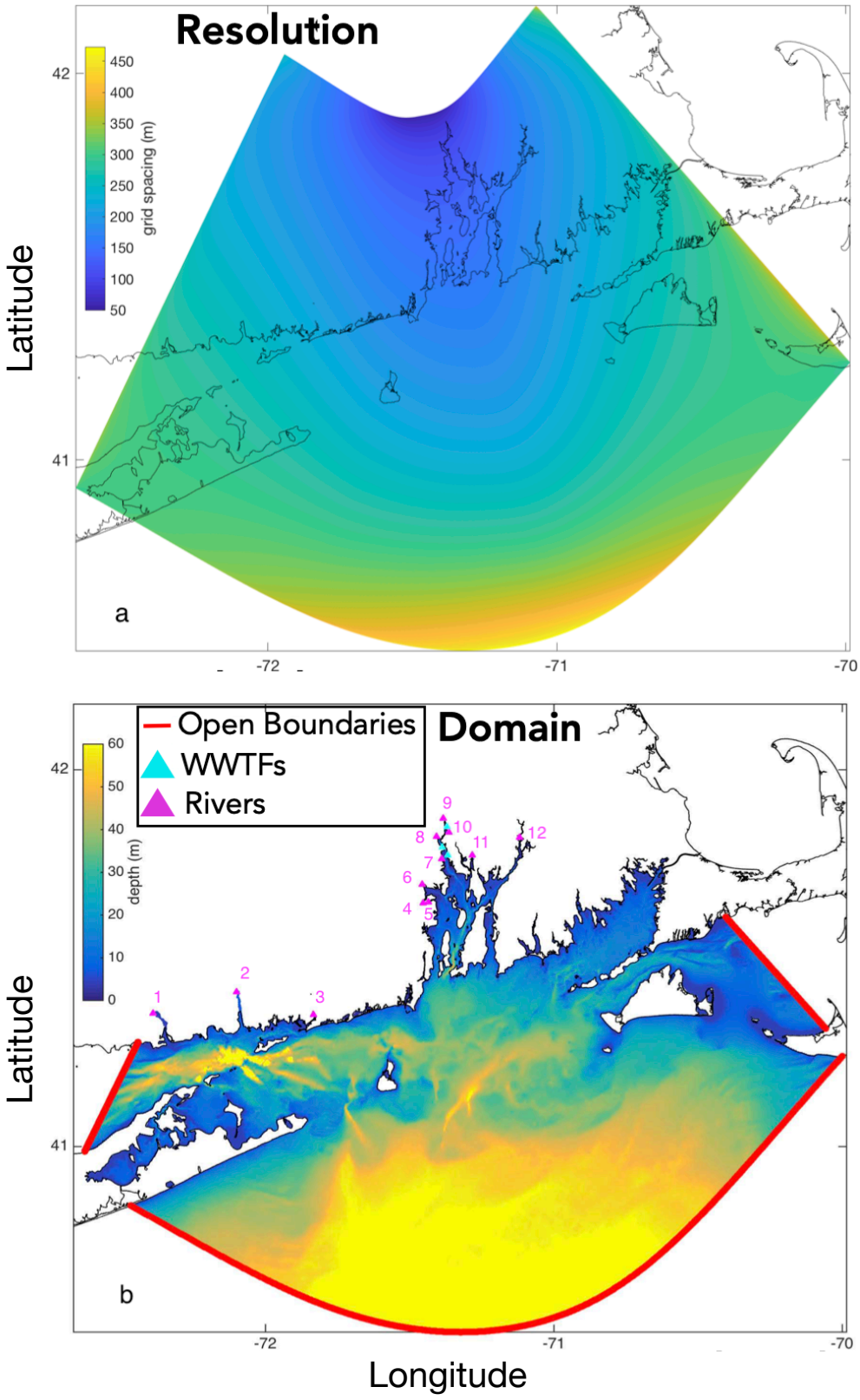

Figure 2.1: a. ROMS OSOM horizontal grid resolution, which is the geometric average of that in the ζ direction ($\sim$ East - West direction) and in the η direction ($\sim$ North - South direction). The finest resolution is in northern Narragansett Bay and resolution decreases towards the open ocean. b. Bathymetry: The Narragansett Bay and Mount Hope Bay are regions of shallow bathymetry and depth increases across the Rhode Island Sound towards the open ocean. Wastewater Treatment Facilities (WWTFs) are shown in blue. Important rivers are highlighted in magenta: 1. Connecticut River, 2. Thames River, 3. Pawcatuck River, 4. Maskerchugg River, 5. Hunt River, 6. Hardig Brook, 7. Pawtuxet River, 8. Woonasquatucket and Moshassuck River, 9. Blackstone River, 10 Ten Mile River, 11. Palmer River, 12. Taunton River.

depth-averaged velocity forcing are implemented using the Chapman (1985) and Flather (1976) methodologies respectively. The depth-dependent velocity, temperature, and salinity at the open boundaries are forced using the Marchesiello et al. (2001) combined radiation and nudging open boundary condition using low-pass filtered NECOFS output. The nudging timescales vary with stronger nudging on inflow (timescale of 1.6h) than on outflow (timescale of 24h).

Surface heat and momentum fluxes are estimated from meteorological variables obtained from models and local observations using the updated COARE bulk formulae (Fairall et al., 2003). All meteorological forcing except for winds are assumed to be spatially uniform over the model domain. Spatially variable winds for the region were obtained from the North American Mesoscale (NAM) analyses, a data-assimilating, high resolution (12 km) meteorological simulation (https://www.ncei.noaa.gov/data/north-american-mesoscale-model/access/historical/analysis). Air temperature and barometric pressure were estimated by averaging the measurements at the six stations of the Narragansett Bay PORTS system (http://www.co-ops.nos.noaa.gov/ports.html). Precipitation and relative humidity are from observations at T. F. Green Airport, in Warwick, RI. Net shortwave and downward longwave radiative fluxes were taken from the nearest ocean gridpoint of NOAA's North American Regional Reanalysis model (http://www.emc.ncep.noaa.gov/mmb/rreanl). Upward longwave radiation was computed based on the ocean surface temperature in the model simulations.

Freshwater discharge from local rivers and the major waste water treatment facilities (WWTF) discharging into NB were applied as point source inflows. The discharges of many of the rivers are measured at United States Geological Survey (USGS) gauging stations (Hunt, Palmer, Moshassuck, Woonasquatucket, Blackstone, Ten Mile, Pawtuxet, Taunton, Pawcatuck, Connecticut, Quinebaug,

Yantic, and Shetucket Rivers). The Moshassuck and Woonasquatucket Rivers, which discharge into the upper Providence River, were combined in the model. Likewise the gauged discharges of the Quinebaug, Yantic, and Shetucket Rivers were combined to form the model Thames River. For the small rivers entering Greenwich Bay (Maskerchugg River and Hardig Brook) which are presently not gauged, historical flow measurements were used with simultaneous measurements from the nearby Hunt River to develop a linear regression model predicting the discharge of the former from gauged measurements from the latter river. The gauging stations varied in their proximity to the locations at which the rivers discharge into the model domain. In order to account for the river discharge from the portion of the watershed downstream of the gauging station, the measured discharges were scaled up using estimates of the drainage areas upstream and downstream of the gauge under the assumption that discharge/drainage area downstream is equal to its value upstream of the gauge. Discharges from four WWTFs (Fields Point, Bucklin Point, East Providence, and East Greenwich) in the upper/mid Bay region were obtained from the plant operators.

The WWTF point sources were implemented at a single ROMS gridpoint but the discharges for the rivers are spread over 2–5 gridpoints to reduce the tendency for model instability. River forcing in ROMS requires, in addition to the river discharge discussed above, specification of the vertical profile of the river inflow transport and the concentration of tracers in the inflowing water. The vertical profile of the river inflow was specified as linearly varying with zero transport at the bottom. Salinity of the inflowing water was set to 0. In the simulations discussed here, the river water temperature was also set to 0 which eventually leads to artificially cold rivers, but experimentation versus using more realistic temperatures reveals modestly lower temperatures at the observation sites in the Bay over the integration times used (especially in winter). Setting river

temperature to 0 only affected the temperatures in zone 1 and 5 for winter where rivers have more influence (Figure 2.5 illustrates zone boundaries). The cold bias found was about 4-6 K in zone 1 and 1-2 K in zone 5. The temperature at the grid points closest to buoys were not affected as all the observation locations shown in Figure 2.2 are sufficiently away from river sources. However, it is recommended for future operational simulations that time varying river water temperature be estimated using a regression equation involving air temperature as well as water temperature on the previous day.

2.2.1 Basic model validation

The model output has been compared with buoy data obtained from the Rhode Island Data Discovery Center (http://ridatadiscoverycenter.org), where a variety of regional data are accessible. In particular, the model has been compared with moored observations collected at locations shown in Figure 2.2. Figure 2.3 illustrates the best and worst matches for temperature and salinity of the model with the historical observations. Comparison of the model versus surface temperatures derived from LandSat also confirms that the patterns of heating and cooling are similar to the satellite data, although seasonality in OSOM is somewhat larger than in the satellite record (by roughly 1°C in climatological comparisons).

Figure 2.3 indicates that the model has skill at the high frequency variability (tides and diurnal cycle), although variability at the bottom level is underestimated. The lower frequency temperature and salinity have biases of up to 2°C at the surface and 1°C at the bottom, and 3 and 2 psu at the surface and bottom of MtHB. At GB, the errors at surface and bottom are up to 5°C and 6 psu and 2°C and 4 psu respectively. Table S1 in supplemental information shows root mean square error

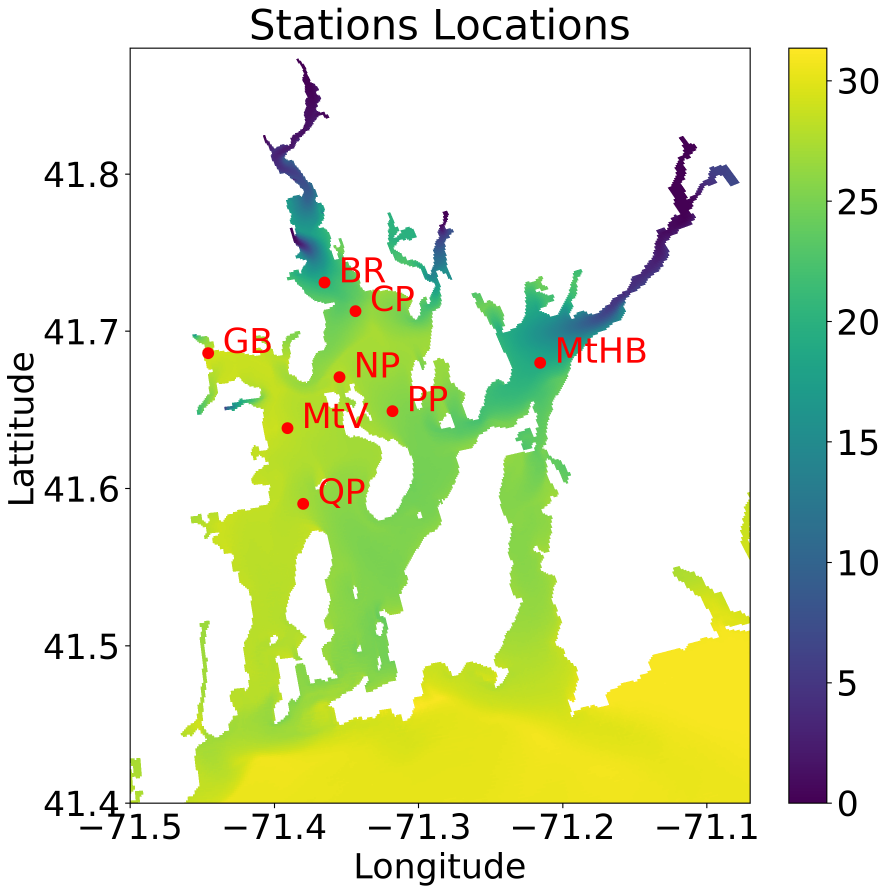

Figure 2.2: Stations where surface as well as bottom temperature and salinity observations are continuously collected during the months of July-August of 2006: Greenwich Bay (GB), Bullock's Reach (BR), Conimicut Point (CP), North Passage (NP), Mount Hope Bay (MtHB), Poppasquash Point (PP), Mount View (MtV), and Quonset Point (QP). Model data is compared with observations from these stations. The background colormap shows an example salinity field.

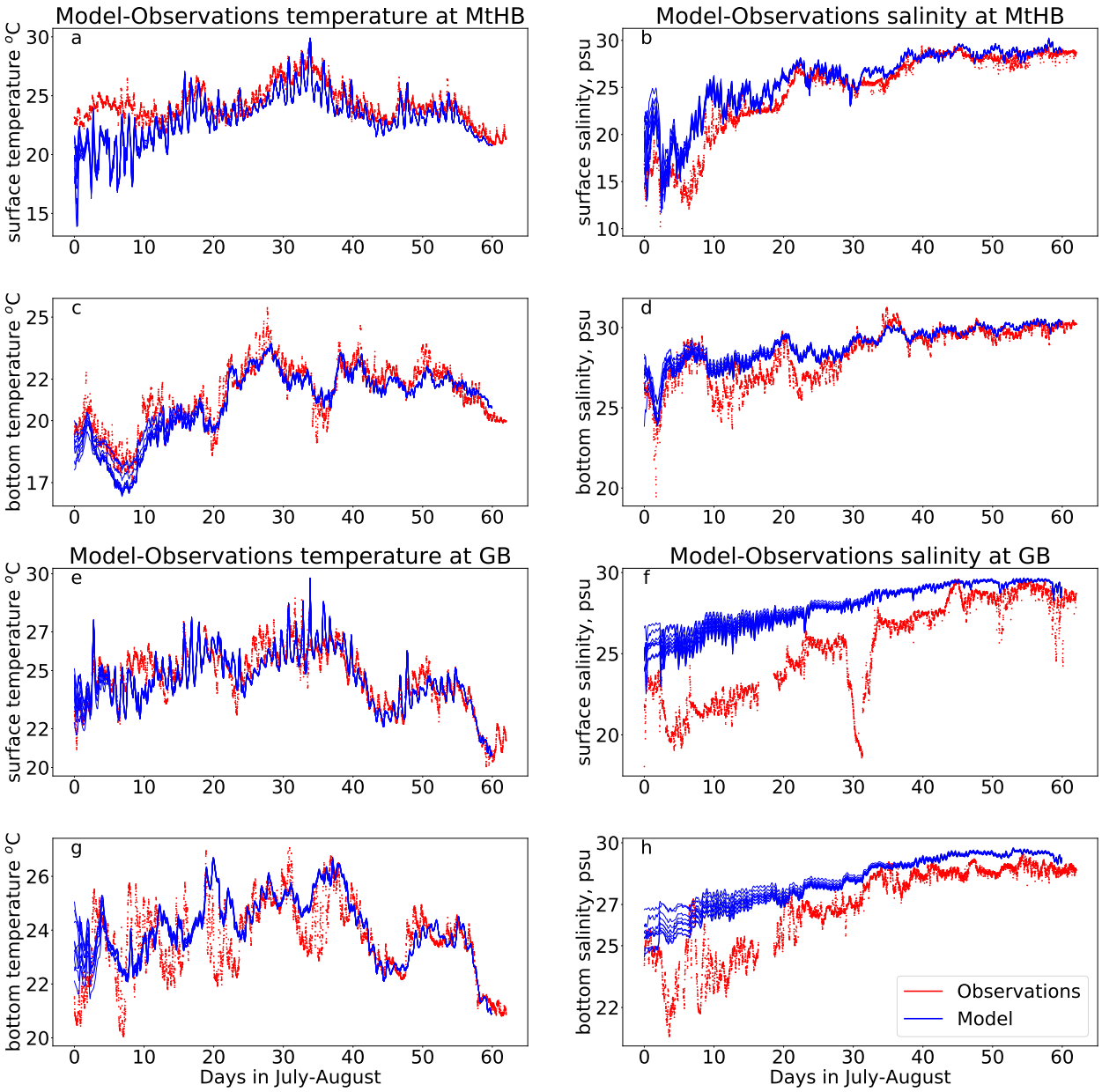

Figure 2.3: (a-d) Comparison of the Mount Hope Bay moored buoy observations of salinity and temperature at the surface (a, b) and maximum depth (c, d). This case is the closest match of the OSOM to the observations during the two months shown: July and August of 2006. (e, f, g, h) Comparison of the Greenwich Bay moored buoy observations of salinity and temperature at the surface (e, f) and maximum depth (g, h). This case is the poorest match of the OSOM to the observations during the two months shown: July and August of 2006. Red color represents the observed values and blue color show different ensemble members. Figures S1 to S6 in the supporting information compare the rest of the marked observation locations.

for all the stations.

The emphasis of this paper is on measuring the basic predictability of the OSOM as modeled in this version. Predictability has been inferred from model-model comparison and not model-observation comparison because our focus is on potential predictability. It is not necessary for this assessment for the OSOM to be completely realistic, but these basic comparisons show that it has skill in reproducing realistic variability in temperature and salinity. Future work will address improvements in the model setup to reduce biases and errors, such as improving the assumed temperature of river inflows, parameterizations of mixing, evaluation of tides, different products for surface and offshore boundary conditions, etc.

2.3 Predictability using information theory

DelSole and Tippett (2007) state that the two guiding principles for measuring predictability of a variable by contrasting the forecast and a climatology distribution should be 1) separate, non-identical measures for a given prediction, and 2) the measure of predictability should be invariant to linear transformation (Schneider and Griffies, 1999; Majda et al., 2002). Measures of predictability using information theory are naturally invariant to linear transformations and will be explained in general in the following paragraphs.

Consider a signal, such as a variable or regional average of a variable modeled by the OSOM, X, having a probability distribution $p_i(x)$ when considered over a particular time or space interval. The probability distribution $p(x_i)$ is of the i^{th} event (i^{th} bin) after dividing the data into N bins. A

fundamental quantity in information theory is the Shannon entropy (Shannon, 1948) defined by

$$H(X) = \sum_{i=1}^{N} p(x_i)\, log_2 \left(\frac{1}{p(x_i)} \right). \tag{2.1}$$

The entropy (with base 2 logarithm) is quantified in units of *bits*, because the Shannon entropy effectively measures the average amount of digital storage required to capture the information present in the variability of X.

To understand Equation 2.1 begin with the innermost term. **?** first proposed using the logarithmic function $log_2(1/p(x_i))$ to quantify information or uncertainity in an event having probability $p(x_i)$. The formulation $log_2(1/p(x_i))$ implies that low probability events have higher uncertainty. Shannon (1948) completed this measure by additionally weighting the logarithm with probability giving rise to the *entropy* definition Equation 2.1, which resembles the thermodynamic entropy function in statistical mechanics resulting from a system that visits a set of equally probable states (e.g. Sethna et al., 2006). Shannon's entropy is formulated so that high probability events reduce uncertainty with a strong weighting because they occur often (Cover and Thomas, 2012). Shannon entropy quantifies uncertainty and the number of states needed to categorize a single probability distribution.

To compare two distributions $p(x)$ and $p(y)$ relative entropy and mutual information measures are useful comparative metrics. Kleeman (2002) recommends the relative entropy (a.k.a., Kullback-Leibler distance Cover and Thomas, 2012) for climate modelling, which is

$$R = \sum_{i=1}^{N} p(x_i) \log_2 \frac{p(x_i)}{p(y_i)}.$$

Here, let X be the forecast and Y be the climatology. Recall that predictability measures

the information contained in a particular forecast that is not present in the climatology, i.e., the information which stems from the forecast initial conditions. It is easy to see that if the forecast probability $p(x_i)$ equals the climatology forecast $p(y_i)$, R goes to zero indicating no distance or difference in information between the forecast and climatology. As a forecast evolves, during the time interval before R reaches zero, $p(x)$ and $p(y)$ are distinguishable (under similar levels of unpredictable noise) and after R reaches zero they are not, thus this time interval is the predictability window.

Within the predictability window, interchanging $p(x_i)$ and $p(y_i)$ changes the value of R, not just by sign from the logarithm, but also by magnitude due to the prefactor $p(x)$. Thus, the relative entropy R depends on both $p(x)$ and $p(y)$ asymmetrically and will change if they are interchanged (i.e., the metric depends on which variable is considered the climatology and which is considered the forecast). Our potential predictability will compare different ensemble members where one is taken as forecast member, and from the same ensemble a different member is taken as a climatology reference (Kumar et al., 2014). As the different ensemble members should be interchangeable in this approach, the magnitude of our metric (in contrast to R) should not change by interchanging the forecast and climatology, hence a different metric is preferred: mutual information.

Mutual information, $I(X;Y)$, is symmetric in X and Y, and hence is a natural metric of distance between these variables without direction. Let two random variables X and Y have joint probability $p(x_i, y_j)$ and marginal probability $p(x_i)$ and $p(y_j)$. X and Y are divided into N bins each (they can also be divided into different bins but we have used the same number of bins for simplicity).

The mutual information $I(X;Y)$ between them is (Cover and Thomas, 2012)

$$I(X;Y) = \sum_{i=1}^{N} \sum_{j=1}^{N} p(x_i, y_j) \log_2 \frac{p(x_i, y_j)}{p(x_i)p(y_j)}, \tag{2.2}$$

Mutual information resembles relative entropy. In fact, it measures the relative entropy between the joint distribution $p(x_i, y_j)$ and the product of the marginal distributions $(p(x_i)p(y_j))$. If X and Y are independent variables, then $p(x_i, y_j) = p(x_i)p(y_j)$ and thus $I(X;Y) = 0$. However, if they are *not independent*, so that one contains information about the other, then there is mutual information shared and $I(X,Y) > 0$. If they are totally dependent, i.e., knowing the value of X reveals the value of Y and *vice versa*, then $p(x_i, y_j) = p(x_i) = p(y_j)$ for each value of i, j and the mutual information equals the Shannon entropy: $I(X,Y) = H(X) = H(Y)$. Thus, mutual information is the metric of the information shared by X and Y versus if they were independent variables. Mutual information between X and Y is symmetric and measures a distance between the two probability distributions. It quantifies the amount of information one variable contains about the other (again in bits). It can also measure the reduction in uncertainty of one distribution given knowledge of a second distribution, or the degree to which they are not independent (Cover and Thomas, 2012): $I(X;Y)$ measures the degree of statistical constraint of X on Y and *vice versa* (Fano, 1961). Mutual information is easily extended to more than one variable leading to a multivariate predictibilty analysis (DelSole and Shukla, 2010).

Unlike relative entropy R, mutual information $I(X;Y)$ does not go to zero when $p(x)$ approaches $p(y)$, instead it approaches the Shannon entropy $H(X)$ from Eq. 2.1. We use the property that $I(X;Y)$ approaches $H(X)$ to delimit the predictability window, taken as when the probability distribution of the forecast and the climatology become effectively indistinguishable, taken to be

the first time when $I(X;Y)$ reaches within 90% of $H(X)$. This threshold is somewhat arbitrary, as convergence is not typically monotonic or complete, so any threshold will tend to have "near misses" and later signs of potential predictability as will be illustrated in a variety of figures in the text and supplementary material. However, to compare to the flushing timescales in later sections, a threshold is a simple test, and a range of predictability timescales is then formulated by comparing to individual climatology ensemble members as well as the climatology ensemble mean to appropriately gauge the level of certainty.

DelSole and Shukla (2010) state that mutual information itself is a measure of forecast skill and provide skill scores founded on mutual information and relative entropy. The metrics in Equations 2.1-2.2 are based on the probabilities of events, not the units or dimensions of the events, so their use on various parameters and between forecasts and climatology can be compared regardless of the type of variable: physical variables, biological variables, chemical variables, or sociological variables of arbitrary units can be compared. For this reason, these information theory metrics are ideal for evaluating forecast skill in a model like OSOM where a variety of applications are intended. The metrics are also invariant under linear transformation of the signal and hence are robust to trivial changes such as changes of the units of measurement (DelSole and Tippett (2007)), unlike alternatives such as the root mean square technique for skill assessment (for example, Jin et al., 2018) which require normalization. The root mean square metric is sensitive to outlier and might over or under estimate predictability. This is because outliers get the same weight as non outliers. Using information theory circumvents this issue because probability distributions are used which naturally gives less weight to outliers as they are few in numbers. Mutual information also measures total correlation by measuring dependence between the two variables (Watanabe, 1960).

To find the predictability time scales of ROMS-OSOM we will compare ensembles members which differ in initial conditions. Hence our focus is on finding the potential predictability (model-model comparison) instead of actual predictability or model forecast skill (model - observation comparison, for example, Kumar et al., 2014). The climatology comes from the model simulations and is a result of past or historical forcings (hindcasts) with unperturbed initial conditions. It will be compared to forecasts with an anomaly of perturbed initial conditions that will eventually decay or be flushed out. The time it takes for the forecast to approach the climatology is the predictability time scale. In other words, the convergence between forecast member and climatology member signals the end of the predictability time period. After this period running the forecast is of no utility, and it will statistically resemble any climatological estimate without predictable consequences remaining from its initial anomaly. This decay occurs because even though an anomaly is introduced, the forcings and boundary conditions are identical between the climatology and the forecast. In a realistic forecast, the model would be initialized with observations and run with historical external forcings as future external forcings are unknown a priori. The initialization due to observations would create anomalies which are similar to perturbations we add to initial conditions in hindcasts to find potential predictability. Also, in a realistic forecast, the forecast signal will begin to diverge away from future observations and converge towards the model climatology signal–another sign marking the predictability time scale.

2.4 Ensemble setup

To begin with initial conditions, temperature and salinity were interpolated from hindcasts of the FVCOM model (Beardsley and Chen, 2014) and velocities were taken to be zero. From

these conditions, the model was spun up for two months before analysis begins. Two months was estimated to be sufficient as the average flushing time in NB is about one month (Pilson, 1985), and post-analysis estimates of the predictability timescale confirm this conjecture. The initial conditions used for ensemble simulations were derived from one single spun-up simulation for each season taken from the boundary conditions for the year 2006. Figure 2.4 shows a sketch of a three membered ensemble of a generic variable to outline this ensemble setup procedure. The blue line shows the spin up. From consecutive days before the spin up ends, initial conditions are drawn. They are shown as three black dots on the blue line. These three states are used to create initial conditions labelled as $c1$,$c2$, and $c3$ and model is run forward displayed by black thick lines. The uncertainty in the initial conditions directly arises from sampling the daily conditions just prior to start of ensemble simulations. We define these three members as constituting our 'climatology ensemble'. Their mean is denoted by letter m and the mean of climatology members is shown by dashed black line. The forecast members shown in red, are denoted as $f1$,$f2$, and $f3$. They are created by perturbing $c1$,$c2$, and $c3$ by their anomaly from the mean. For example, $f1$ is created by multiplying $(c1-m)$ by 3 and adding it to m, $f1 = 3(c1-m)+m$. Similarly $f2$ and $f3$ are created. $f1$, $f2$, and $f3$ are members constituting the 'forecast ensemble' and are shown in red color. All the c and f members undergo the same forcing. The values inside the running window are binned to find their frequency of occurence. These frequencies are converted to discrete probability ditribution using Python Numpy's histogram function. Shannon entropy is applied to values of m inside the running window τ as shown in green color. Mutual information is calculated between values of forecast member and ensemble mean for the running window. For example, Shannon entropy, $H(m)$, of values of m inside τ will be compared with mutual information, $I(m;f1)$, between values of m and $f1$ inside τ. This will quantify how much information is shared between

$f1$ and m with respect to m. As running window moves forward,$H(m)$ and $I(m; f1)$ will be found as a function of time.

To get the ensemble, simulations were performed in each of two seasons: January-February (JF) and July-August (JA). The months JA were chosen because NB faces hypoxia during those months (Codiga et al. (2009)), and JF was chosen as a contrasting alternative. For each season (JF, JA) there is a set of climatology ensemble members that were simulated consisting of 7 and 10 members respectively. The JF and JA climatology ensemble has two sets of corresponding forecast ensembles: one initialized by perturbing only temperature, and the other set initialized by perturbing only salinity.

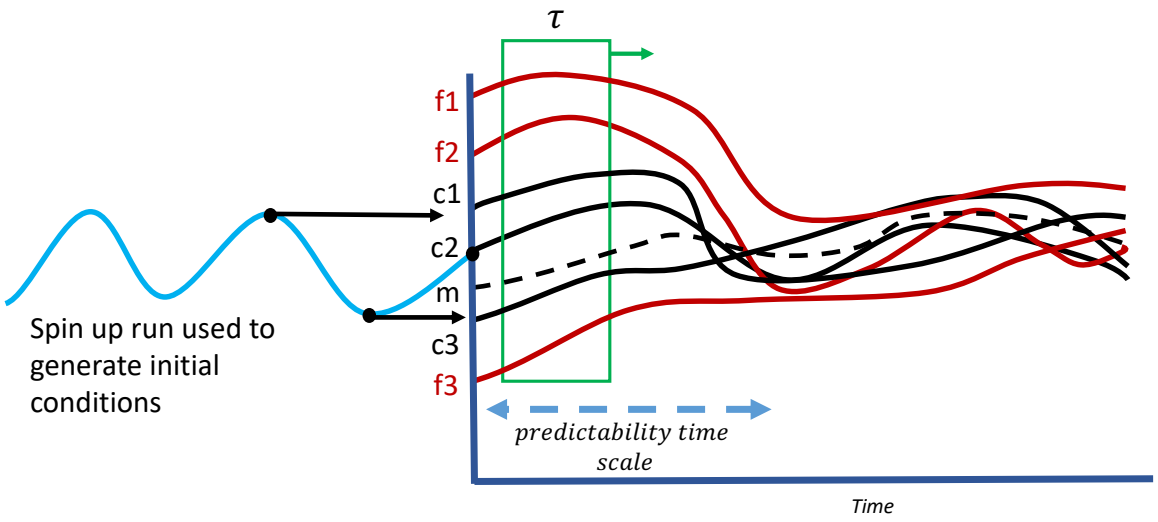

Figure 2.4: Sketch showing generation of ensemble members. Blue line represents a spin up simulation. The members denoted by $c1$, $c2$, and $c3$, termed 'climatology ensemble' and shown by black lines, have initial conditions generated from consecutive days of the spin up run. Member denoted by m is the climatology ensemble average. The forecast members $f1$, $f2$, and $f3$ are shown in red lines and their initial conditions are generating from corresponding climatology members by perturbing them away from m. The running window is shown in green color. Shannon entropy is applied to values of m inside the running window. Mutual information is found for values of a forecast member and m inside the running window.

Each climatology ensemble member is forced in the same way, but each has realistic initial conditions chosen from consecutive days selected from the spin-up run before the simulation start

day (Smith et al., 2007). This method of building a climatology ensemble is perhaps unfamiliar to some readers, and differs from the typical average across multiple years of simulations (where the climatology is across varying forcing, rather than varying initial conditions). To create a larger contrast, the same initial conditions were perturbed by tripling the anomaly of each climatology ensemble member from the climatology ensemble mean. This second ensemble of enhanced initial conditions are called the "forecast ensemble", and the same number of members are in the forecast and climatology ensembles (7 in JF and 10 in JA). The forecast ensemble members by design have bigger spread in their initial conditions than the climatology ensemble. As each ensemble contains both forced and internal variability, it was not sufficient to have only one forecast represent the "climatology", but rather a mean over an ensemble of realistic initial conditions serves as a better reference climatology. Furthermore, it is potentially undesirable to compare a single climatology run versus an ensemble mean of forecasts–care is needed to compare ensemble means versus ensemble means (the approach here) and individual simulations versus individual simulations. However, comparing the individual models within the ensembles is used to formulate a range of possible predictability timescales, and comparing individual members with other individual members yields similar results to the ensemble versus ensemble comparison method used primarily here.

Model data is saved in 2 hour window time averages. The granularity is needed to capture the strong tidal variability in this region. Thus each day has 12 data points for all the variables and for all the ensemble members. Predictability analysis is performed for 3 types of data: 1) Timeseries of volume-weighted averages of variables (temperature, salinity) over the 7 zones shown in Figure 2.5, 2) Predictability of kinetic energy using spatial data over 7 zones, and 3) Predictability of timeseries

for a grid point closest to a moored observation. Thus, the effects of predictability on different variables or different levels of averaging is illustrated.

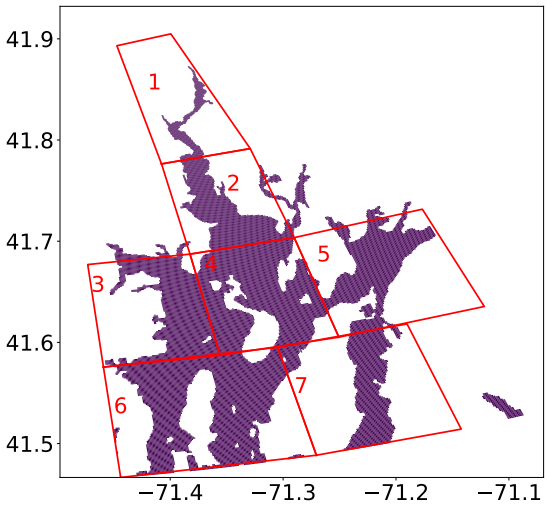

Figure 2.5: Narragansett Bay has been divided into 7 zones. Volume weighted temperature and salinity has been used from each zone to find predictability timescales.

The number of ensemble members is justified by deciphering whether external forcing (wind, tidal, river runoff, and evaporation/precipitation) or internal chaos (nonlinearities, eddies) is setting the trend for evolution of state parameters in the ensemble mean. The methodology of Llovel et al. (2018) and Leroux et al. (2018) is used as a guide. The ratio of "noise" to signal with respect to time was found, where noise is taken as the standard deviation of the model spread and signal is the mean over the ensemble. Let σ be the standard deviation of ϕ_i^n, which is also same as the model spread. The ratio $\sigma_i/\langle\phi\rangle_i$ remains less than 0.5 within the predictability window and below 0.1 after crossing predictability time scale. Llovel et al. (2018) state that a noise to signal ratio of less than 0.5 is sufficient so that external forcing is dominant in setting the ensemble mean variability over internal chaos, indicating also that model trend is captured sufficiently with this number of ensemble members. An upcoming companion paper by the authors (Sane et al., 2021) expands on

the approach of Llovel et al. (2018) using information theory techniques to quantify forced versus internal variability even for non-Gaussian and non-independent datasets.

Let a variable in the climatology ensemble be given by $c^n_{t,i}$ where t denotes time, i denotes spatial grid-point, and n is the ensemble member. Similarly, a variable in the forecast ensemble is $f^n_{t,i}$. The information entropy metrics have been calculated between forecast and climatology using two approaches: 1) Between running time windows (probability distributions of variability in t) of spatial volume weighted averaged data (i.e., averaged over i) in a zone or at an observation location, and 2) examining the covariability of spatial grid points (probability distributions based on i) within a zone at a fixed time. The advantage of the former is that it more naturally describes the evolution of slow variations over large regions of the Bay, while the latter can be used for very rapid convergence of variables with shorter predictability timescales.

The first approach, which uses a running window, is primarily used for evaluating predictability of temperature and salinity. First, data is averaged (volume weighted) over each zone. Hence, $\Sigma_i \left[c^n_{t,i} \mathrm{d}V_i\right] / \left(\Sigma_j \mathrm{d}V_j\right) = \overline{c}^n_t$ and $\Sigma_i \left[f^n_{t,i} \mathrm{d}V_i\right] / \left(\Sigma_j \mathrm{d}V_j\right) = \overline{f}^n_t$ with the over-bar representing volume weighted average over a zone ($\mathrm{d}V_i$ is the volume associated with each gridpoint). Next, the ensemble mean of all climatology members was found, given by $\langle \overline{c} \rangle_t = (1/N) \sum_{n=1}^{N} \overline{c}^n_t$ where the angle brackets represent ensemble average. m from Figure 2.4 is equal to $\langle \overline{c} \rangle_{t=0}$. A running window of size τ is selected and a histogram of values inside the running window is used to estimate the probability distributions of the climatology and forecasts, from which $I(f;c)^n_t$ is calculated over the time interval with climatology spanned by end members $(\langle \overline{c} \rangle_t, \langle \overline{c} \rangle_{t+\tau})$ and forecast variability $\left(\overline{f}^n_t, \overline{f}^n_{t+\tau}\right)$ according to Equation 2.2. Shannon entropy $H(c)^n_t$ is also calculated from these histograms for $(\langle \overline{c} \rangle_t, \langle \overline{c} \rangle_{t+\tau})$ according to Equation 2.1. The predictability time is taken to be when the mutual

information averaged over the forecast ensemble $I(f;c)_t = (1/N)\sum_{n=1}^{N} I(f;c)_t^n$ reaches 90% of the climatology ensemble mean Shannon entropy $\langle H(c)\rangle_t$. The resulting timescales are tabulated in table 2.1. The uncertainty range (square brackets in table 2.1) for the timescale is estimated by repeating the above procedure N times replacing $\langle \overline{c}\rangle_t$ with each of the climatology ensemble members $\overline{c}_t^n$. Results for a typical zone, Zone 6, are shown in Figures 2.6 and 2.7. Predictability time scale obtained by comparing forecast ensemble members to the single unperturbed member from the climatology ensemble were similar to when compared with the mean of climatology ensemble (see Figures S26-S32 in supplemental information). Comparing climatology ensemble members with the single unperturbed climatology member also gave similar results (see Figures S33-S39 in supplemental information).

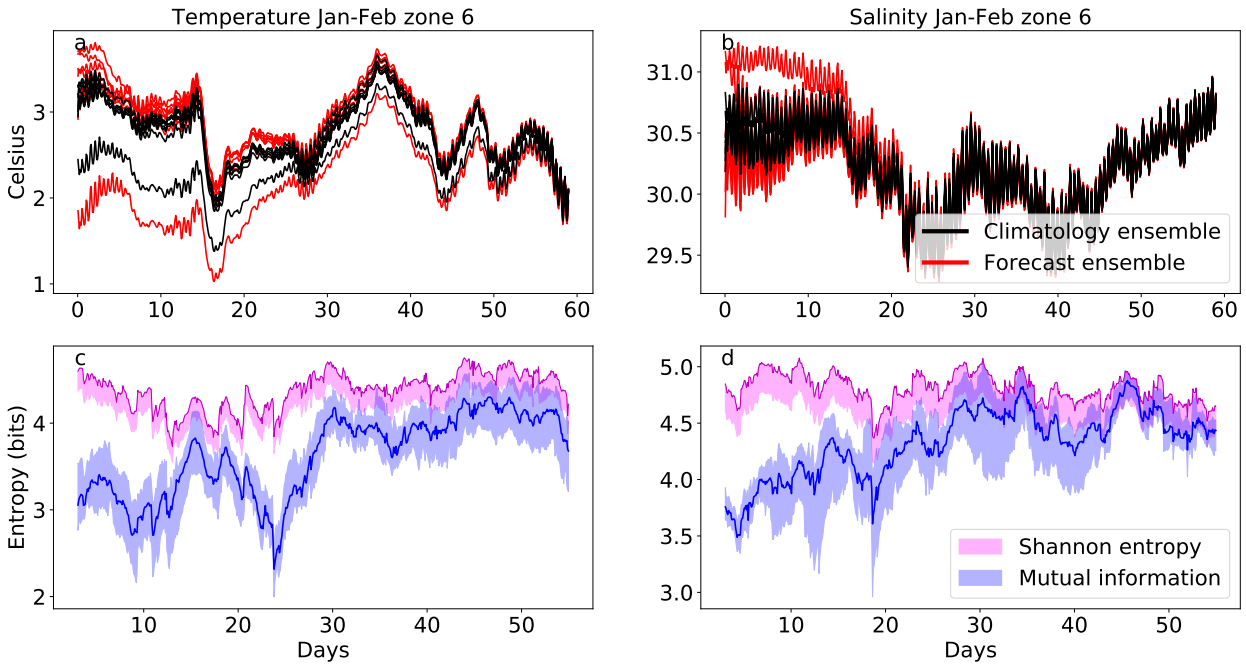

Figure 2.6: Predictability results for Zone 6 volume-averaged temperature (c) and salinity (d) in January to February. Top: Temperature (a) and salinity (b) timeseries from ensemble members is plotted for 7 climatology ensemble members (in black) and 7 forecast ensemble members (in red). Bottom: Information theory metrics (temperature (c) and salinity (d)) shows the convergence of mutual information (blue) with Shannon entropy (pink). The blue range indicates the forecast ensemble and the blue line is the forecast ensemble mean. The Shannon entropy of the climatological mean is shown at the top of the pink range and 90% of this value is shown as the bottom of the pink range. The mutual information converges to 90% of the Shannon entropy in 7-40 days (Table 2.1). Figures S14 to S19 in the supporting information show similar plots for other zones.

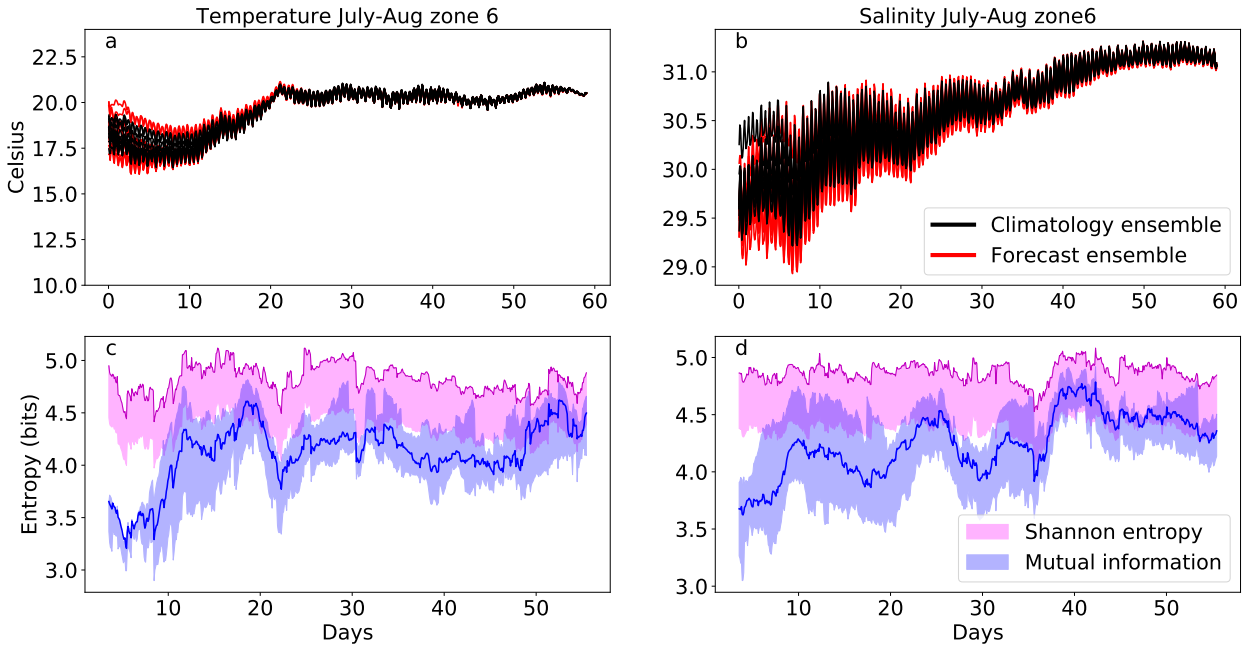

Figure 2.7: Predictability results for Zone 6 volume-averaged temperature (c) and salinity (d) in July to August. Top: Temperature (a) and salinity (b) timeseries from ensemble members is plotted for 10 climatology ensemble members (in black) and 10 forecast ensemble members (in red). Bottom: Information theory metrics (temperature (c) and salinity (d)) shows the convergence of mutual information (blue) with Shannon entropy (pink). The blue range indicates the forecast ensemble and the blue line is the ensemble mean. The shannon entropy of the climatological mean is shown at the top of the pink range and 90% of this value is shown as the bottom of the pink range. Figures S20 to S25 in the supporting information show similar plots for other zones.

Figure 2.8 shows a similar method of estimating predictability at a single grid point near the Mount Hope Bay (MtHB) buoy, which follows the same algorithm but without spatial averaging. The running window method is useful when the time interval under consideration is long enough to provide a reasonable histogram approximation of the temporal probability distribution. The histogram intervals and bin sizes were chosen for each case such that the predictability time period is not sensitive to variations around those values (overly small or large choices show significant dependence on choices of binning and duration). The predictability timescale remains more sensitive to τ than the number of bins. While entropy and mutual information are both sensitive to data binning and duration choices, the timescale for mutual information to converge to Shannon entropy is less sensitive for the selected bin sizes and duration.

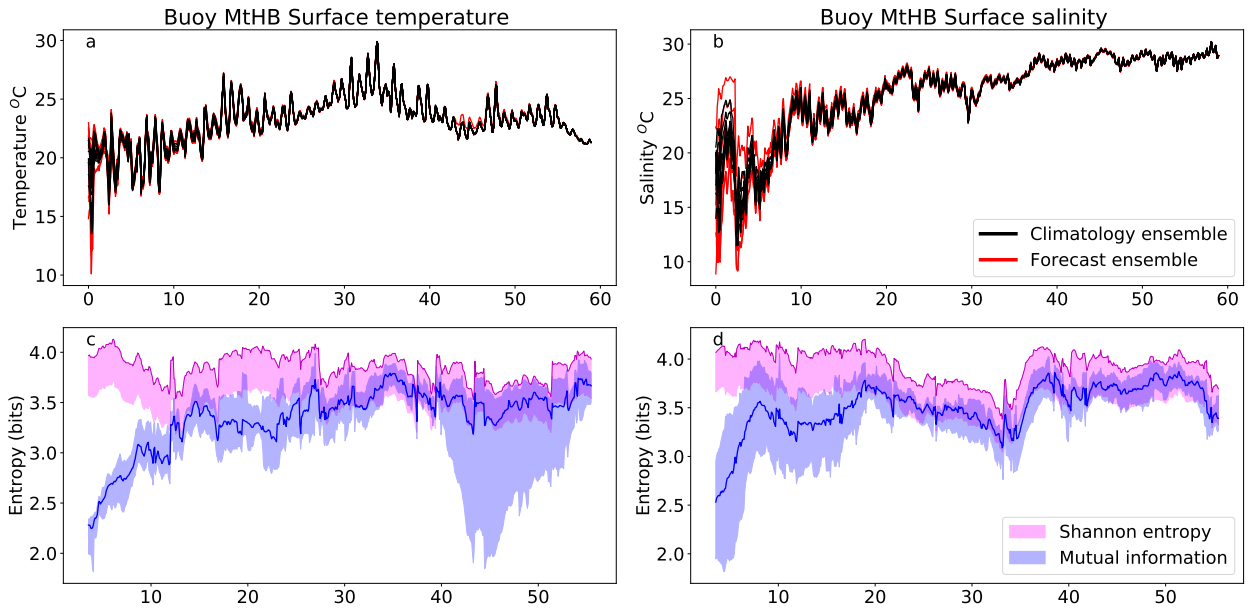

Figure 2.8: Surface temperature (a) and salinity (b) predictability metrics during July-August at one grid point closest to Mount Hope Bay (MtHB) buoy as shown in Figure 2.2. Information theory metrics for temperature and salinity are shown in c and d respectively. Surface temperature at this location is predictable for 27.4 [13.7 - 27.4] days and surface salinity is predictable for 18.5 [8.3 - 19.5] days. Figure S13 in the supporting information shows bottom temperature and salinity predictability.

For the above method to work, the running window should have reasonably enough number of points to make a probability distribution. Also the running window should be of smaller size than the predictability time scale to effectively find the predictability time scale. This works for temperature and salinity, but for kinetic energy a different approach is needed because predictability time scale is less than a couple of days so enough data points are not available on volume weighted time series signals. So a different approach is employed which uses values of all the grid points at a particular instant of time on the spatial grid to create probability distributions by finding frequency of occurences. The second spatial variability method evaluates entropy using all spatial grid points within a zone. Let Z be the set of all grid points in a zone. $I(f;c)_t^n$ is evaluated from Equation 2.2 between the spatial histograms estimating the probability distributions of $\langle c \rangle_{t,i \in Z}$ and $f_{t,i \in Z}^n$. $H(c)_t^n$ is evaluated using Equation 2.1 for $\langle \overline{c} \rangle_{t,i \in Z}$. This approach eliminates the need for time windows by

comparing the spatial variation between the forecast and climatology ensemble mean. Figure 2.9 shows the short predictability window of kintic energy.

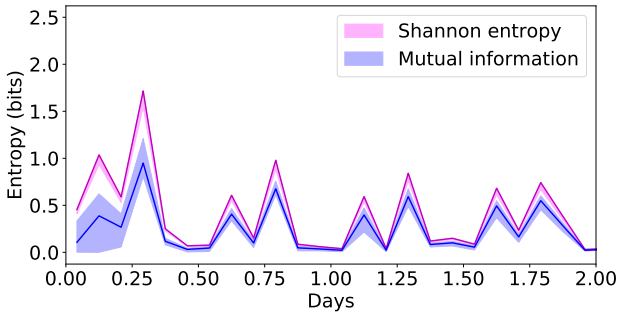

Figure 2.9: Kinetic energy predictability is less than 2 days for Zone 6 for July-August. In this case, the spatial variability metric was used as the predictability timescale was shorter than the running time windows. Using all the spatial grid points instead of the volume weighted time series provides enough sample points to create a probability distribution, and is also sensitive to convergence in higher-order statistics beyond the spatial mean. Alternatively, very frequent output windows in time could have been used with the time window method, but this method was chosen to illustrate the possibilities when initial condition effects are quickly lost and there is rapid convergence to climatology. Kinetic energy results for other zones is similar and are given in supporting information Figures S7 to S12.

Both the running window and spatial variability approaches use data without fixed references and are non-parametric. The data is not assumed to be Gaussian or any other distribution and hence our approach is robust towards all kinds of probability distributions, so long as the sampling is such that the histograms are an accurate representation of the probability distributions. Likewise, the method measures variability by the same units of measure in the forecasts and climatology, so the units or standards of measurement are consistent regardless of whether physical, biological, environmental, or other metrics are chosen.

2.5 Results

2.5.1 Predictability results

Figures 2.6 and 2.7 show typical temperature and salinity results, drawn for both seasons from Zone 6. Other zones are similarly illustrated in the supplementary material. In each figure, the first row shows a timeseries comparison between the climatology ensemble (black) and forecast ensemble (red). The second row has information theory statistics, which permit a more precise time of convergence than just comparison of the timeseries in the upper row. Magenta shows $H(X)$ and the range of $H(x)^n$, the entropy of $c_{t,i}$, blue members represent $I(X;Y)^n$ and single blue line between blue shaded region is the average $I(X;Y)$ over all the $I(X;Y)^n$. Table 2.1 has the predictability timescales and uncertainty range. Results for each zone from 1 to 7 and combinations of zones which progressively increase in volume from North to South are tabulated in Table 1. The combined zones enable us to compare the predictability time scale with flushing/turnover time scales evaluated over similar combined regions measured by distance from the northern end of the estuary to the southern end (Figure 2.10).

Table 2.1 compares the predictability timescales by region and season. The summer timescales tend to be longer, reflecting the typically drier conditions during summer of the year simulated. The timescales for salinity tend to increase as more and more of the Bay regions are included, indicating that anomalies persist somewhere within the Bay after initialization. For regions within the Bay, local circulations and patterns of mixing differ among the different regions, but few clear patterns emerge. Overall, the span of timescales is from 6.9 days to 40.5, indicating that predictions of a week or longer may potentially have skill, and that 1-2 months of spinup is necessary for initial

Table 2.1: Predictability in days for January-February with respect to zones for temperature and salinity based on when mean mutual information between ensemble members and climatology reaches 90% of climatology's Shannon entropy for the first time. The range is estimated by the range over each of the member of the climatology ensemble. 1 to 5 implies all the zones consolidated from 1 to 5 and similarly for 1 to 7.

zones	January-February		July-August	
	Temp.Pred.(days)	SalinityPred.(days)	Temp.Pred.(days)	SalinityPred.(days)
1	36.5[36.2-37.2]	7.3[6.9-7.7]	10.2[9.1-10.6]	9.4[9.1-9.9]
2	14.2[12.1-14.3]	10.5[9.4-11.0]	10.3[9.3-33.0]	27.7[26.6-29.0]
3	11.5[11.5-12.0]	18.3[18.3-19.0]	16.4[16.0-27.4]	23.8[22.1-26.3]
4	13.0[13.0-14.9]	16.9[16.7-17.0]	22.5[21.1-31.5]	31.5[31.4-32.5]
5	11.9[11.7-13.0]	16.9[16.8-17.1]	9.6[9.5-23.0]	18.5[16.6-31.2]
6	30.2[30.0-33.8]	21.9[20.1-23.0]	17.8[17.3-27.0]	23.0[22.9-24.5]
7	14.9[14.1-28.7]	25.5[19.0-26.7]	22.5[20.4-31.0]	10.0[9.0-10.3]
1 to 2	15.0[14.2-33.5]	9.5[9.3-9.5]	23.4[22.3-34.2]	24.8[22.1-28.1]
1 to 5	11.8[11.7-29.8]	17.1[17.1-17.6]	10.0[10.0-26.2]	29.4[29.4-30.6]
1 to 7	14.0[13.2-29.7]	17.0[17.0-18.0]	32.6[18.4-40.5]	31.4[31.4-32.6]

condition effects to be lost and for forcing to become dominant.

Figure 2.8 shows an example of temperature and salinity predictability for a single grid point, for a location nearest to the Mount Hope Bay buoy (MtHB in Figure 2.2). Perhaps counter to intuition, the central predictability timescale estimates (temperature: 27.4 [13.7 - 27.4] days; salinity: 18.5 [8.3 - 19.5] days) is quite long for this one gridpoint in comparison to the predictability of the whole Zone 5 that contains it (Table 2.1 and Supplementary figures; zone-averaged temperature: 9.6 [9.5 - 23.0] days; zone-averaged salinity: 18.5 [16.6 - 31.2] days), but note that the estimated ranges are consistently overlapping. There are many processes which would increase the amount of internal variability at a single location, such as meandering currents, waves, and other effects of flow-topography interaction. Thus, the predictability of an individual measurement location need not agree with the predictability of the region containing it, because of this internal variability would be missing from the zone averages. However, in this case and indeed for all of the monitoring buoy locations shown in Figure 2.2, the buoys are deployed deliberately in locations thought to be

representative of their section of the Bay rather than within a particular feature such as a regular plume or jet. Thus, the agreement in predictability timescales is perhaps not coincidental, but reflects judicious choices for observational advantage. Presenting results at this single location highlights the possibility of evaluating predictability metrics at one location, not just in regional averages, and the potential reasons why these two approaches may differ.

Likewise, predictability is not limited to temperature and salinity. The predictability of kinetic energy is shown in Figure 2.9 for Zone 6 and is less than 2 days. The mutual information converges towards Shannon entropy within a very short period, and the alternative method of calculating the probability distribution using spatial variability is needed. As will be shown in the next section, there is consistency between the timescales of freshwater and salinity flushing and predictability timescales, which argues that the estuarine circulation tends to dominate these tracers. However, anomalies in the kinetic energy within a region are much more quickly generated (by winds and instabilities) and dissipated (by viscous and drag parameterizations) in the OSOM, and so the predictability timescale is one to two orders of magnitude shorter for kinetic energy than for temperature and salinity. Thus, the kinetic energy example illustrates that it is important to evaluate predictability on each metric of forecast interest. The next section explores the physical implications of the predictability timescales in comparison to flushing timescales.

2.6 Turnover timescales

The turnover or flushing time scale is the time scale required for replenishment of a particular water mass in the estuary, based on its rate of resupply or removal. For a water mass having a volume V and volume flux rate Q, the flushing time scale is simply $\tau = V/Q$ (e.g., Monsen et al., 2002; Rayson et al., 2016). In the present study the freshwater turnover/flushing time scale and the salinity turnover time scale are calculated from the model output and compared with the predictability time scales. The approach here follows Lemagie and Lerczak (2015) in comparing estuarine timescales by standard definitions, except here the estuarine timescales are also compared with the predictability timescale.

The freshwater volume is estimated using the relation

$$V_f = \left(1 - \frac{s}{s_o}\right) V_b, \tag{2.3}$$

where V_f is the freshwater volume, s is the volume weighted average salinity of the Bay, s_o is the salinity of the open ocean or the salinity of the incoming volume flux in the region under consideration, and V_b is the volume of the Bay. The freshwater flushing time scale is

$$\tau_f = \frac{V_f}{Q_r}, \tag{2.4}$$

where Q_r is the river supply and runoff.

The salinity turnover timescale follows the isohaline procedure of MacCready (2011). The fluxes of saline water masses are calculated for each salinity class. Let $Q(s)$ be tidally averaged

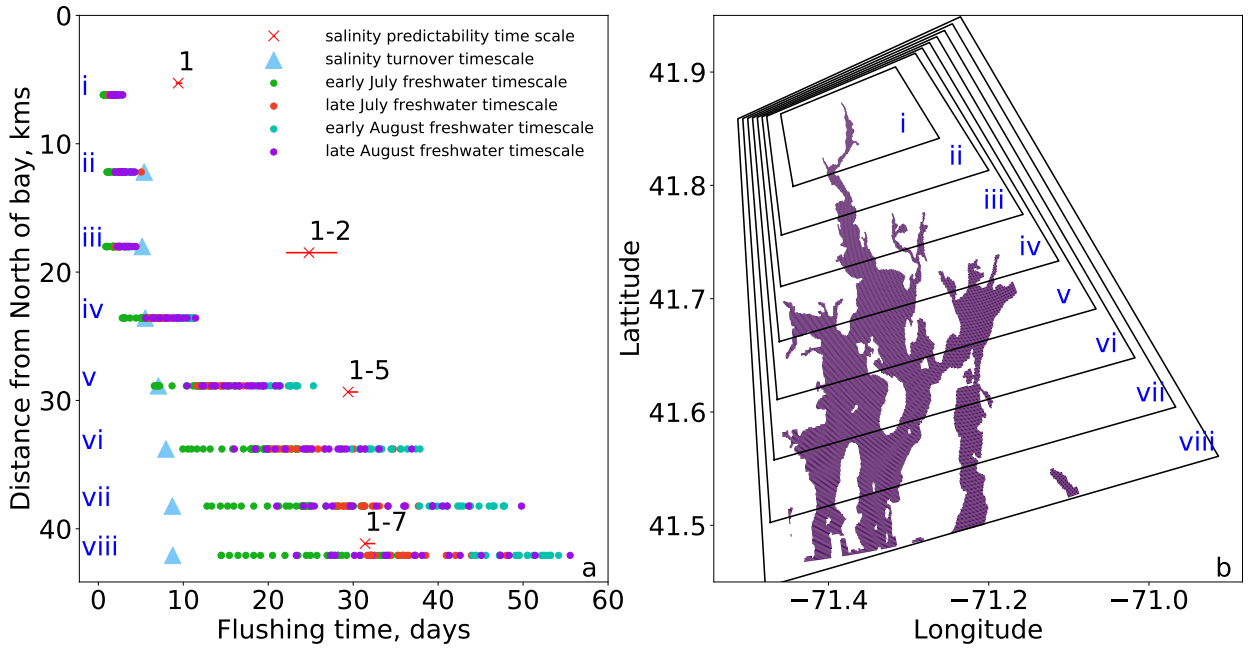

Figure 2.10: Figure a: Freshwater flushing timescales, salinity turnover timescales, and salinity predictability timescales for July-August as a function of distance from the northernmost extent of Narragansett Bay. Blue boxes show the salinity flushing timescale (Equation 2.8). Circular scattered points show the freshwater flushing time estimated from freshwater volume and divided by river input (Equation 2.4). Different colors show averages over different periods within July - August. For comparison, the salinity predictability time scale is shown by red crosses, for Zone 1 and then the combined regions (1 to 2, 1 to 5, 1 to 7). These salinity predictability time scales are the same as shown in the last three rows of Table 2.1. Figure b shows the control volumes chosen to calculate freshwater and salinity flushing timescales. The control volumes have been marked from i to viii and the corresponding freshwater and salinity timescales have been shown in the left Figure.

salinity flux corresponding to salinity s and be given by:

$$Q(s) = \left\langle \int_{A_s} u \, \mathrm{d}A \right\rangle . \tag{2.5}$$

where double angled brackets denote temporal filtering over a tidal period with a Butterworth filter. A_s is the cross sectional area having salinity greater than s. $Q(s)$ is the salinity flux for the salinity belonging in the range (s, s_{max}). $Q(s)$ is evaluated laterally at a vertical cross section along the estuary, beginning at the north and proceeding south. The flux moving in, Q_{in} and moving out,

Q_{out}, of the estuary is calculated using an integral over the salinity classes:

$$Q_{in,out} = \int \left.\frac{\partial Q}{\partial s}\right|_{in,out} ds \,, \tag{2.6}$$

where "in" and "out" are evaluated on the basis of the sign of the integrand. MacCready (2011) defines the fluxes as total exchange flow (TEF). The TEF relates to corresponding salt fluxes of

$$F_{in,out} = \int s \left.\frac{\partial Q}{\partial s}\right|_{in,out} ds \,. \tag{2.7}$$

The MacCready (2011) approach results in the salinity turnover timescale of

$$\tau_s = \frac{\int s dV}{F_{in}} \,. \tag{2.8}$$

Using above definitions, τ_f and τ_s have been found by considering a control volume with one end fixed at the mouth of Providence river at the northernmost end of NB and the other end gradually increasing towards the South. Figure 2.10b shows the control volumes marked from i to viii used to calculate the flushing time scales. The intention is to estimate these timescales in order to check whether they agree with predictability timescales. The time scale results are displayed in Figure 2.10 by using circle and triangle markers along with predictability timescales for the corresponding regions. The y-axis is the distance from the north of the Bay to the south end of each control volume. So for each point in the Figure 2.10a shown by circle or triangle marker, the flushing time calculated is for the entire corresponding region as shown in Figure 2.10b. This includes the rivers as source of freshwater flux and the South end of each control volume acts as "open ocean"

for that control volume. The x-axis provides the ranges of timescales. The predictability time scales shown by red crosses are for consolidated regions. For example, 1-5 means all the regions 1,2,3,4,5 as shown in Figure 2.5. The predictability timescales are consistent in magnitude with the various flushing timescales and increase as the quantity of the Bay in the control volume increases (although somewhat less rapidly with distance). Four time periods are shown by colors–early and late for July and August–illustrating that the flushing timescales vary significantly (with the amount of precipitation, mainly).

2.7 Discussion

The predictability timescales measure the persistence of statistical anomalies deviating from climatology that stem from the initial conditions. These anomalies might be detected to decay, through information theory metrics, by a variety of processes: tidal or wind-driven mixing, being carried out of the Bay by advection, or becoming so well stirred by turbulent motions that they no longer persist as statistical anomalies. The consistency between the salinity and temperature predictability timescales and the salinity flushing timescales illustrates that it is likely that these anomalies are removed from the Bay primarily by the estuarine circulation whose timescale is estimated with the variety of flushing timescales shown. Even pointwise measurements tend to agree with their zone-average prediction timescale (Figure 2.8), which indicates that the anomalies in OSOM temperature and salinity tend to be fairly mixed over broad areas, so that regions and buoys capture much the same information. It is not clear if this is true in the real Narragansett Bay to the same degree, but the consistency in the degree of variability between the modeled buoy locations and the buoy observations (Figure 2.3) suggests that this may be.

We believe that 3 out of 4 predictability times are longer than either turnover time because the flushing times assume inputs and outputs interact with a volume of *well-mixed estuary*, whereas the predictability time scale measures the persistence of statistical anomalies in the domain considered. The latter may be subject to statistics emanating from lingering water masses from recirculations or slowly-mixed regions within the estuary.

The predictability timescale of kinetic energy is one to two orders of magnitude shorter than that of temperature or salinity (Figure 2.9). This suggests that kinetic energy in NB is not governed solely by the estuarine overturning. Indeed, NB and the OSOM are highly tidally-driven – with the majority of the kinetic energy involved in the ebb and flow. Apparently, the propagation of the tidal energy into the Bay through waves, winds, currents, dissipation and drag, and generally perturbations to the surface elevation and kinetic energy, are a rather different set of processes operating on very different timescales from the estuarine overturning that transports the salinity and temperature anomalies and their predictability.

2.8 Conclusions:

This study has introduced the Ocean State Ocean Model (OSOM) and measures of its intrinsic timescales. The predictability timescales range from 6.9 to 40.5 days for temperature and salinity. The predictability timescales differ for different periods of the year and the region under observation–with generally longer periods for the larger basins and under drier conditions. These relationships are consistent with the expectations of estuarine circulation dominating the flushing of anomalies in salinity and temperature, and these predictability timescales are quantitatively similar to the range of estimates of flushing timescales.

Information theory proves useful for quantifying predictability. It can also be applied to other variables such as physical, biogeochemical, and environmental metrics that are being considered for forecasting with the OSOM. Not all variables have the same timescales, as some rely on processes that operate at different speeds.

While it is important to know the predictability timescales for understanding the constraints on spinning up a model and the *potential* length of a forecast, it is important to keep in mind that the *skill* of a forecast is not simply related to the predictability. Here the model skill is adequate for the assessment of predictability (Section 2.2.1), but the model shows skill deficiencies in some locations, as highlighted here by comparison to observations at the Greenwich Bay buoy (Figure 2.3). Such biases and errors in a model may not affect the predictability timescale, but they clearly reduce the value of a forecast. Future work in tuning the model parameterizations and improved forcing will increase model skill but are not expected to change the predictability. A higher-resolution version of the model is expected to have better skill and lower biases, but the stronger chaotic transport and resolved eddying features in such a model are likely to decrease the predictability timescale (by increasing internal variability). This is one key reason why predictability metrics are not an aspect of Narragansett Bay itself, but only of this particular model: the OSOM.

In the case of temperature and salinity predictability in the OSOM, forced estuarine circulations tend to set the dominant timescales. Knowing this is useful in estimating forecast windows, spin up times, and sensitivity to forcing variability. Other systems, and perhaps the kinetic energy in this system, are dominated by internal variability rather than forced variability. A companion paper (Sane et al., 2021) expands on this topic for coastal modeling, where a variety of different boundary forcing mechanisms can contribute.

Acknowledgments

The Rhode Island Coastal Ecology Assessment Innovation & Modeling grant (NSF 1655221) supported this work. BFK was also supported by ONR N00014-17-1-2963 and NSF 1350795. This material is based upon work conducted at a Rhode Island NSF EPSCoR research facility Center for Computation and Visualization (Brown University), supported in part by the National Science Foundation EPSCoR Cooperative Agreement #OIA-1655221. J. Benoit provided the LandSat analysis dataset and M. Brush contributed the drainage area dataset. All the data and the codes used to plot results can be downloaded via Brown University's digital archive DOI: https://doi.org/10.26300/crbx-9784.

Chapter 3

Variability

Preface to Chapter 3

Chapter 3 is a verbatim copy of a manuscript being prepared Sane et al. (2021, (preprint)). The title of the article is: “Internal vs Forced Variability metrics for Geophysical Flows using Information theory". The authors of the manuscript are: Aakash Sane, Baylor Fox-Kemper, and Dave Ullman. AS and BFK are affiliated with Brown University and DU is affiliated with University of Rhode Island. The preprint of the manuscript can be found at the permanent DOI: https://doi.org/10.1002/essoar.10505545.1.

DU was involved in setting up the initial model: creating forcing and grid files and evaluating the performance of model with respect to observations. AS and BFK contributed in setting up ensemble runs, and deriving information theoretic metric. Everyone contributed to writing the manuscript.

Abstract

We demonstrate the use of information theory metrics, Shannon entropy and mutual information, for measuring grid-pointwise internal and forced variability in ensemble atmosphere, ocean, or climate models. This metric differs from the standard ensemble-variance approaches and delineates intrinsic and extrinsic variability. Information entropy quantifies variability by the size of the visited probability distribution, as opposed to variance that measures only its second moment. Shannon entropy and mutual information manage correlated fields, apply to any data, and are insensitive to outliers as well as a change of units or scale. In the first part of this aricle, we use an example featuring a highly skewed probability distribution (Arctic sea surface temperature) to show that the new metric is robust even with a sharp nonlinear cutoff (the freezing point). We apply these two metrics to quantify internal vs forced variability in (1) idealized Gaussian and uniformly distributed data, (2) an initial condition ensemble of a realistic coastal ocean model, (3) the GFDL-ESM2M large ensemble. Each case illustrates the advantages of the proposed metric over variance-based metrics. The metric can be applied to any ensemble of models where intrinsic and extrinsic factors compete to control variability and can be applied regardless of if the ensemble spread is Gaussian. In the second part of this article, mutual information and Shannon entropy is used to quantify the impact of different boundary forcing in a coastal ocean model. Information theory is useful as it enables ranking the potential impacts of improving boundary and forcing conditions across multiple predicted variables.

3.1 Introduction

In an ocean or climate model, it is pertinent to understand the cause of variability as it leads to implications for predictability, prioritization of data collections for assimilation, and provides an understanding of the dynamics at play in different regions. In a coastal model, variability can arise from extrinsic factors such as wind forcing, solar and thermal forcing, tides, rivers, evaporation and precipitation, or it can be due to internal chaos inherent to the governing fluid equations (Sane, Fox-Kemper, Ullman, Kincaid, and Rothstein, Sane et al.). In a climate model, modes of variability such as El Niño, the North Atlantic Oscillation, or the Southern Annular Mode, can conceal or delay the emergence of attributable anthropogenic climate change signals (Milinski et al., 2019). In high-resolution ocean models, internal chaos or intrinsic variability can also be due to eddies (Leroux et al., 2018; Llovel et al., 2018). Accurately quantifying the relative contribution of external and internal factors can help in elucidating the causes responsible for the observed variability in models, help to identify key observable metrics, and help quantify concepts such as the time of emergence of climate signals (Hawkins and Sutton, 2012).

Numerous methods exist in the literature to quantify intrinsic and extrinsic variability using models or observations (e.g., Frankcombe et al., 2015; Schurer et al., 2013; Liang et al., 2020). Model ensembles–i.e., a set of simulations sharing the same forcing–naturally vary because each ensemble member follows the same governing equation (with same external forcings) with identical or similar parameterizations but differ due to intrinsic chaos. Two types of model ensembles are common: initial condition ensembles (where the same model is used repeatedly with perturbed initial conditions and intrinsic variability occurs from model's chaotic sensitivity to the initial conditions), and multi-model ensembles (where a variety of models differing in numerics and

parameterizations are used to simulate change under the same forcing–in this case "intrinsic" variability also includes aspects of model formulations). Most of the discussion here will focus on initial condition ensembles, but the metrics proposed can be adapted to both cases.

To help visualize variability, a generic output from an ocean or atmospheric model is shown in Figure 3.1. Each color represents a different ensemble member and the black solid line is the mean of those members. The black solid line is the signal mostly due to extrinsic factors (aside from finite ensemble size limits) and the model spread (schematized by the double-headed magenta arrow in Figure 3.1) can be considered due to intrinsic variability or internal chaos.

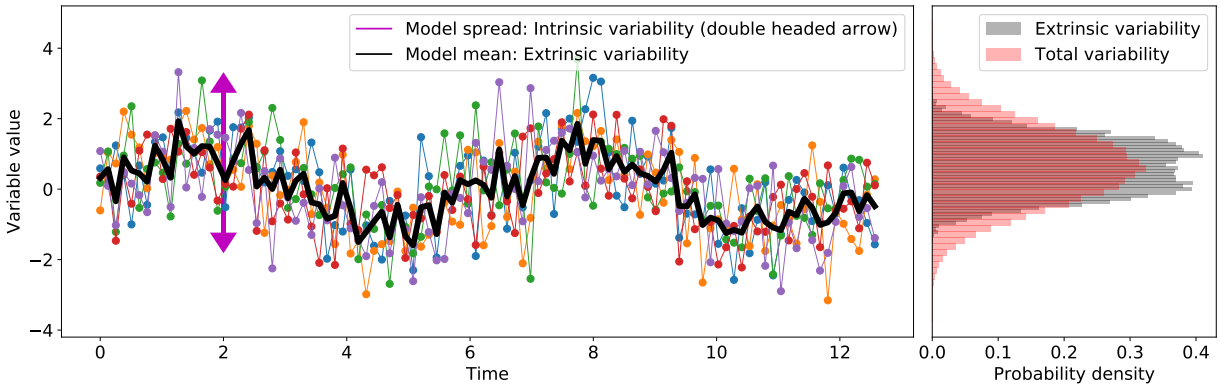

Figure 3.1: A sketch of a typical ocean or climate model output for an arbitrary variable. Each ensemble is shown in different color and the mean of the ensemble is shown as black line. The ensemble mean can be considered to be the trend set by external forcings. The model spread shown by double headed magenta arrow indicates the model chaos.

One method of quantifying intrinsic and extrinsic variability is to look at variances (second central statistical moment) of model spread and model mean (Leroux et al., 2018; Llovel et al., 2018; Waldman et al., 2018; Yettella et al., 2018). Variance is sufficient to constrain all metrics of variability about the mean when distributions are Gaussian and uncorrelated, but a single statistical moment usually measures only part of a more complex variability. Many climatological variables show non-Gaussian distributions (e.g., Franzke et al., 2020). In fact, generalized variance might

be misleading (Kowal, 1971). Quantification of variability should be robust to or have known dependence on changes in the units of the quantity or the scale (e.g., changing temperature from Celsius to Fahrenheit or Kelvin). Comparative metrics, such as intrinsic vs. extrinsic variability should not depend on these arbitrary choices of units at all.

Variability, in essence, is a function of the number of occurrences or frequency of occurrence (or probability p_i as a fraction over all visited system states) after appropriately binning the data (and thereby making the estimated and visited number of states finite rather than continuous). Information entropy metrics measure variability by taking into account the probability distribution of the binned data, drawing on the statistical mechanics concept of entropy in quantifying the number of microstates that a variable can occupy. The fundamental measure in information theory is the Shannon (1948) or information entropy which characterizes the amount of variability in a variable (Carcassi et al., 2019). The mutual information, another metric introduced by Shannon (1948), measures how much information one variable contains about another variable.

Information theory is applied in signal processing, computer science, statistical mechanics, quantum mechanics, etc. It is used to quantify amount of information, disorder, freedom, or lack of freedom (Brissaud, 2005). The application of these abstract notions to geophysical flows can have immense practical benefit when information entropy is interpreted as a measure of variability, as entropy does not rely on any particular parametric probability distribution. Metrics from information theory are not new to climate sciences. They have been introduced in predictability studies, evaluating the skill of statistical models, as well as uncertainty studies (e.g., Leung and North, 1990; Schneider and Griffies, 1999; Kleeman, 2002; DelSole and Tippett, 2007; Majda and Gershgorin, 2010; Stevenson et al., 2013) and recently in studying variability (Gomez, 2020) and

coastal predictability (Sane, Fox-Kemper, Ullman, Kincaid, and Rothstein, Sane et al.).

In this article we bring well-established concepts of information theory to the particular application of measuring intrinsic and extrinsic variability for ensemble model runs within atmospheric and oceanographic modeling. Our metric uses Shannon entropy and mutual information. We indirectly employ conditional entropy, which depends on Shannon entropy and mutual information. To keep the metric intuitive, we have used Shannon entropy and mutual information and not casted it using conditional entropy.

There are two parts to this article. In Part 1, we apply our metric on three sets of data: 1. Idealized Gaussian and uniformly distributed arrays with specified correlation 2. Ensemble output of a regional coastal model (OSOM) (Sane, Fox-Kemper, Ullman, Kincaid, and Rothstein, Sane et al.) where most variables are non-Gaussian. 3. The GFDL-ESM2M Large Ensemble (Rodgers et al., 2015; Deser et al., 2020), hereby referred to as GFDL-LE. This dataset contains historical and RCP 8.5 simulation data. All the monthly mean data from 1950 to 2100 have been used in the anaylsis.

In Part 2, we use OSOM to demonstrate the use of Shannon entropy and mutual information in evaluating the effects of altered boundary forcings. In coastal and estuarine systems, it is pertinent to know which forcings are dominant. For example, is wind forcing dominant over river forcing, does using temporal averaged river runoff cause any appreciable changes in the estuarine circulation or does change in the wind product alter circulation? These questions can be tackled by switching on and off or modifying each forcing and comparing the predicted variables using information theory.

Recent theoretical advances in understanding dynamical systems through the lens of information theory relate causality analysis and information transfer (e.g., Liang, 2014). Although important, the transfer of such theoretical concepts into pragmatic research applications are few. Even basic concepts of information theory (Shannon entropy and mutual information) have been adopted in a limited capacity by the oceanic and atmospheric community to address problems arising in predictability and variability. We attempt to bridge the gap using approximate but practical framework which can be easily replicated and improved upon in the future, including causality analysis and the evolution of entropy within modeling systems like those studied here.

3.1.1 Information theory

We will introduce information theory concisely assuming the reader has no background knowledge–this section contains standard definitions. Consider a probability distribution p_i obtained after binning data into N bins. The user chooses the appropriate number of bins or bin widths for the range of data. Shannon (1948) identified the average information content in N possible outcomes, equally or not equally likely, as given by:

$$H = \sum_{i=1}^{N} p_i \log_2(1/p_i), \tag{3.1}$$

where H is the Shannon entropy with unit of bits when log is base 2 and p_i is the probability of the i^{th} outcome. $\log_2(1/p_i)$ measures the information of the i^{th} outcome as proposed by Hartley (1928) and is also a measure of uncertainty (Cover, 1999). The quantum $\log_2(1/p_i)$ measures the information gained by knowing that the i^{th} outcome has happened. Another interpretation for $\log_2(1/p_i)$ is that it measures reduction in uncertainty by knowing the i^{th} event has occurred, or

that the variable falls in the i^{th} bin. The term information does not mean knowledge but it means the amount of uncertainty shown by a variable or the freedom that a variable has in falling into the i^{th} out of the N bins. Shannon (1948) found Equation 3.1 to provide the average information (or uncertainty) for all events in a record. For the entire set of elements, a highly probable event has less uncertainty associated with it and low probability event has high uncertainty associated with it. The prefactor p_i is thus used to weight the information over all possibilities. One way to interpret the need for the prefactor p_i is that in repeated experiments the events with higher probability will occur more often, hence they should contribute more to a quantification of variability than infrequent events.

Stone (2015) gives an intuitive way of understanding Shannon entropy using a binary tree. A binary tree is a tree chart which starts with 1 node and splits to two nodes at each node. At each node you can take a left or right turn to proceed and if there are say 3 levels in the tree, then 8 (i.e. 2^3) outcomes or possible destinations exist. If a binary tree has N equally probable outcomes then the set of instructions required to reach the correct destination is given by $h = (N)(1/N)\log_2(N) = \log_2(N)$. The *uncertainty* about reaching the correct destination will be removed by providing $\log_2(N)$ *bits* of information. In other words, if entropy is h then 2^h states are possible.

A second metric from Shannon (1948) which is also extensively used is now known as *mutual information*. The mutual information between two signals x and y denoted by $I(X;Y)$ is (Cover, 1999)

$$I = \sum_{j=1}^{N}\sum_{i=1}^{N} p_{ij}\log_2\left(\frac{p_{ij}}{p_i p_j}\right), \tag{3.2}$$

where p_{ij} is joint probability of i^{th} outcome of x and j^{th} outcome of y. p_i and p_j is the marginal

probability of i^{th} and j^{th} outcome of x and y respectively. The addend within the summations can be expanded to $p_{ij}\left(\log_2\left(p_{ij}\right) - \log_2\left(p_i\right) - \log_2\left(p_j\right)\right)$. I can be interpreted as the extra information in entropy of marginal distributions of x and y over the joint distribution. Mutual information is symmetric between x and y and is the measure of how much information they share. For example, if the distributions are statistically independent, then $p_{ij} = p_i p_j$ and thus $I = 0$. If the two records x and y are identical, then $p_{ij} = p_i = p_j$ and $I = H$. I is the average reduction in uncertainty in x by knowing y or vice versa. It denotes how much information is transmitted between the two variables.

In the context of ocean modeling (or in general climate modeling) entropy is used to measure variability in a model output or available data. This is in tandem with interpretation of Shannon entropy in physical sciences as given in Carcassi et al. (2019). When calculating the Shannon entropy we are concerned about the possible states (e.g. the various bins in a histogram) the variable can (and does) go into while the variable value and its dimensions are of lesser importance. Entropy metrics measure variability in *bits* (when logarithm is of base 2) and hence changing the scale, e.g. switching from Celsius to Fahrenheit for temperature, does not change the value of variability (under equivalent binning). Mutual information and entropy are both dimensionally agnostic. They are also not sensitive to outliers (due to the weighting prefactor) and can capture nonlinear interactions (Watanabe, 1960; Correa and Lindstrom, 2013) and discontinuous or intermittent visited states. We will present the effect of correlation and outliers in the sections related to idealized random vectors.

The following methods and results sections are divided into the two parts of the overall paper objectives. Part A of both sections are related to evaluating intrinsic and extrinsic variability in

ensemble models. Part B describes the usage of Shannon entropy and mutual information on coastal regional modeling data to understand and compare effects of using different boundary conditions.

3.2 Methods

3.2.1 Part A: Intrinsic and Extrinsic variability for ensemble data

We perform analysis on each grid point at the ocean surface or ocean bottom. Let a variable from the ensemble be given by $f(n,t,x,y)$ where f is the variable, n denotes the index of the ensemble member and goes from 1 to N, t is the time index and goes from t_1 to t_M, x, y represents the spatial grid point at the surface or bottom. At a particular grid point $f(n,t,x,y)$ is $f(n,t)$. The total number of ensemble members is N and each member has M time steps. To get the signal due to extrinsic forcings, the "differencing" approach (Frankcombe et al., 2015) has been followed to estimate forced response. This approach involves averaging over the ensemble members to derive ensemble mean (also termed as ensemble mean here). The ensemble mean is given by:

$$g(t) = \frac{1}{N}\sum_{n=1}^{n=N} f(n,t) \tag{3.3}$$

$g(t)$ is a single time varying signal for each grid point obtained by averaging the ensemble members. There are potential problems with this assumption such as the model might be sensitive to the forced signal based on the model's equilibrium sensitivity as elaborated in Frankcombe et al. (2015). For a first order approximation, we will asume this as the best estimate of the forced response. Our metric's sensitivity to forced responses evaluated from different techniques will be left for future work. Once $g(t)$ is obtained, the intrinsic variability can be estimated by subtracting the ensemble

mean $g(t)$ from each ensemble member. Ensemble signal, forced response and intrinsic variability are related by:

$$f(n,t) = g(t) + \eta(n,t), \tag{3.4}$$

where $\eta(n,t)$ is the noise (which differs from ensemble member to ensemble member–i.e., it is intrinsic variability). Note that the above is at a grid point. η and f are functions of grid points. In Figure 3.1 a, $f(n,t)$ are shown by multi-colored ensemble members. $g(t)$ is shown by thick black line. As seen in Figure 3.1 b, $g(t)$ has a probability distribution shown in grey color and subsequently has first, second, and possibily higher statistical moments. The grey colored density histogram shows variability due to extrinsic factors and the pink colored density histogram shows total variability given by extrinsic and intrinsic factors.

Detrending and evaluating entropies

Analysis has been done with and without detrending the data to understand its impact. For detrending, a quadratic fit using least squares was found for the ensemble mean at each grid point and subtracted from all ensemble members and ensemble mean at the same grid point to get detrended data (e.g. Frankcombe et al., 2015). Detrending will remove some non-stationarity from the data but will also remove some part of the extrinsic variability. Our aim is not to determine the forced response, but to estimate the degree of *variability* contributed by the forced response (extrinsic response) and intrinsic variability originating from intrinsic chaos. The ensemble mean $g(t)$ was found at each grid point after detrending. For the non-detrended case, the raw ensemble simulation data has been used to evaluate $g(t)$ and $\eta(n,t)$.

Usually we are limited in the number of ensemble members due to computational costs so

we perform a *jugaad* in order to use *all* the ensemble members at once to evaluate information entropies. All the ensemble members given by $f(n,t)$ are rearranged into a single row vector f as:

$$f = [f(1,t_1), f(1,t_2), ...f(1,t_M), f(2,t_1), f(2,t_2), ...f(N-1,t_M), f(N,t_1), ...f(N,t_M)]\,, \tag{3.5}$$

and g is row vector obtained by arranging N copies of $g(t)$ in the following fashion:

$$g = [\underbrace{g(t_1), g(t_2), ...g(t_M)}_{1}, \underbrace{g(t_1), g(t_2), ...g(t_M)}_{2}, ... \underbrace{g(t_1), g(t_2), ...g(t_M)}_{N}] \tag{3.6}$$

This enables wide sampling and obtains an accurate probability distribution for f (assuming approximate stationarity, or enforcing stationarity by detrending), and enables g to be of the same size as f and having the same porbability distribution as that of $g(t)$. The information statistics we get at each grid point are time invarient since the complete time series is considered. It is the user's choice to choose either the complete time series or a section of it for analysis. We have chosen the whole time series, as this is a sufficient demonstration of the value of information theory metrics. A time-evolving analysis raises additional issues about causality and shifting probabilities distributions of climate states that are not the focus here (Liang, 2013; DelSole and Tippett, 2018). By using the whole timeseries, we are treating all variability as drawn from the same distribution, and seek only to associate internal (associated with each ensemble member) and external (associated with the ensemble mean) sources of variability following Leroux et al. (2018). The timeseries f and g are both expressed as row vectors of the same size, $N \times M$. This step is crucial as vectors having same number of elements are necessary to evaluate joint probability distribution. This enables us to calculate mutual information between f and g.

Calculating the Shannon entropy of f and mutual information between f and g is not a trivial task. In fact optimal binning for precise measurement of information entropies is a research topic in itself. Multiple techniques exist such as equidistant partitioning, equiprobable partitioning, k nearest neighbour, usage of B-spline curves for binning to name a few (e.g. see Hacine-Gharbi et al., 2012; Kowalski et al., 2012; Knuth, 2019). For a comprehensive review of the methods for getting probability distribution see Papana and Kugiumtzis (2008). We have used equidistant partitioning throughout this article. For the case of GFDL-LE data, there were 1812 time steps available as monthly averages ranging from the year 1950 to 2100. As per Rice's rule, 25 bins are needed for the GFDL-LE data. The bin width, δw, was calculated by dividing the range of data (maximum minus the minimum value) at the grid point with the least spread. The same bin width was used for all the grid points for Shannon entropy and mutual information. Equal bin width was used for the two variables in the joint probability and marginal probability calculation for mutual information. Maintaining the same bin width and range for all the grid points is crucial because information entropy strongly depends on the precision with which data is binned. To check sensitivity of our binning choice, the endpoints of each bin were shifted by $\delta w/2$ and results were compared. For temperature, the raw data gave an error of 0.0473 in γ and detrended data gave error of 0.11. For salinity, the error in γ for raw data was 0.017 and for detrended data was 0.02. Similar analysis for ROMS-OSOM coastal ensemble data gave negligible error for shifting the bin endpoints. Different binning strategies will be left to be explored for future research.

Proposed metric

Using f and g, we propose the following metric γ, which has the same intent as metrics in (Leroux et al., 2018) to quantify the fraction of variability that is intrinsic, i.e., the typical amount

that is unique to an ensemble member or statistical instance, but unlike (Leroux et al., 2018) this metric is built from standard information theory quantities:

$$\gamma = 1 - \frac{I(f;g)}{H(f)}. \tag{3.7}$$

$H(f)$ is the Shannon entropy of f, and $I(f;g)$ is mutual information between f and g. $I(f;g)$ calculates the contribution of extrinsic signal g to the whole ensemble. $H(f)$ is the total variability in the ensemble output which is the result of extrinsic and intrinsic factors. The metric γ gives the *ratio of intrinsic variability to total variability*.

$H(f)$ and $I(f;g)$ are related through conditional entropy by $H(f) = I(f;g) + H(f|g)$ (Cover, 1999). $H(f|g)$ is the conditional entropy[1], i.e., average uncertainty about the value of f after g is known. It is the uncertainty in f that is not attributed to g but is attributed to noise η. Hence $H(f) - I(f;g)$ estimates variability due to intrinsic chaos.

Returning to the binary tree analogy, $I(f;g)$ would be the set of instructions sent by a source to reach one among $2^{H(f)}$ possible destinations in the presence of noise having $H(f|g)$ entropy. To capture the entropy in the noisy binary tree, to each of the $2^{I(f;g)}$ microstate possibilities noise $\left(2^{H(f|g)}\right)$ gets multiplied and the relation becomes $2^{H(f)} = 2^{I(f;g)}2^{H(f|g)}$.

$I(f;g)$ takes into account any correlation or information shared between f and g. This is vital because even though the model spread η is being treated similarly to noise added to the mean signal, it might be that model spread depends on the mean signal. A simple example is if the model spread is relative (e.g., 10% of the mean signal), rather than absolute (e.g., 2 units), then

[1]Conditional entropy $H(X|Y)$ is defined by $H(X|Y) = \sum p(x|y)\log_2 p(x|y)$ (Cover, 1999). It is not necessary to calculate conditional entropy to arrive at γ, but understanding is aided by the expected relation between entropy and mutual information.

there is information about the model spread contained in the ensemble mean signal. This situation is sometimes called multiplicative noise in contrast to additive noise. The nonlinear and chaotic nature of fluid mechanics often leads the mean flow to amplify the chaotic signal (e.g., eddies) and thereby result in altered variability statistics. When $f \to g$, then $I(f;g) \to H(f) = H(g)$ from (3.2). This makes $\gamma = 0$ when there is no intrinsic variability or chaos. When intrinsic chaos fully dominates the ensemble output, i.e. f and g are fully decorrelated, then $I(f;g) = 0$ yielding $\gamma = 1$. We see that γ satisfies the extremes of zero noise as well as total chaos.

Another analogue for a climate system component is a noisy communication channel as given in Leung and North (1990), where the governing equations of ocean (atmosphere) modeling are taken to communicate from forcing to response. The extrinsic forcings are inputs to the channel, the intrinsic chaos is the noise created because of channel's inherent mechanisms while the outputs are the ensemble members. A noiseless channel will give γ as zero and completely noisy channel where output is independent of input will yield γ as 1.

A seemingly enticing and simpler alternative is $\gamma = 1 - \frac{H(g)}{H(f)}$, i.e. just the difference between ensemble entropy and mean entropy as a ratio with the ensemble entropy. However, this formulation is incorrect because $H(g)$ does not quantify the contribution of extrinsic factors to the variability in the ensemble, it only quantifies the variability of the mean. Relatedly, $H(f) - H(g)$ does not correctly manage mutual information between the ensemble members and their mean in estimating the intrinsic variability.

Recently, another alternative was proposed by Gomez (2020): using Shannon entropy directly as a measure of intrinsic variability. They propose using Shannon entropy of model spread $\eta(n,t)$ at each time step normalized by the logarithm of the number of bins utilized. Their metric has

a lower limit of 0 and an upper limit of 1, where 0 denotes zero noise and hence zero intrinsic variability and 1 denotes complete intrinsic variability. Again, this metric is similar to γ in building upon information theory, but γ takes into account the variability of the ensemble mean, correlations between the ensemble mean and the intrinsic variability, and it is time invariant. A time dependent version of γ can be made using running time windows instead of the whole time series, but care in quantifying or controlling for lack of stationarity is needed in this interpretation (DelSole and Tippett, 2018). The Gomez (2020) metric uses the spread of the ensemble members similar to measuring Shannon entropy whereas γ utilizes, in an abstract sense, the set of instructions required to choose a destination for the particular variable among the possibile model states.

Variance based metric

A variance based metric as given in (Leroux et al., 2018) has been utilized to compare to our information based metric. The variance based metric measures intrinsic and extrinsic variability using the second moment, variance. It involves calculation of the following terms σ_g and σ_η given by:

$$\sigma_g^2 = \frac{1}{M}\sum_{t=1}^{t=M}\left(g(t) - \overline{g(t)}\right)^2, \tag{3.8}$$

$$\sigma_\eta^2(t) = \frac{1}{N}\sum_{n=1}^{N}\eta(n,t)^2, \tag{3.9}$$

where the overbar denotes temporal averaging. The total variability has been estimated as $\left(\sigma_g^2 + \overline{\sigma_\eta^2(t)}\right)^{1/2}$. The forced variability σ_g is equivalent to $I(f;g)$, and total variability $\left(\sigma_g^2 + \overline{\sigma_\eta^2(t)}\right)^{1/2}$

is equivalent to $H(f)$. Hence, γ is compared with γ_{std} given by

$$\gamma_{std} = \frac{\left(\overline{\sigma_\eta^2(t)}\right)^{1/2}}{\left(\sigma_g^2 + \overline{\sigma_\eta^2(t)}\right)^{1/2}} \tag{3.10}$$

3.2.2 Part B

Impact of changes in boundary forcings in coastal models

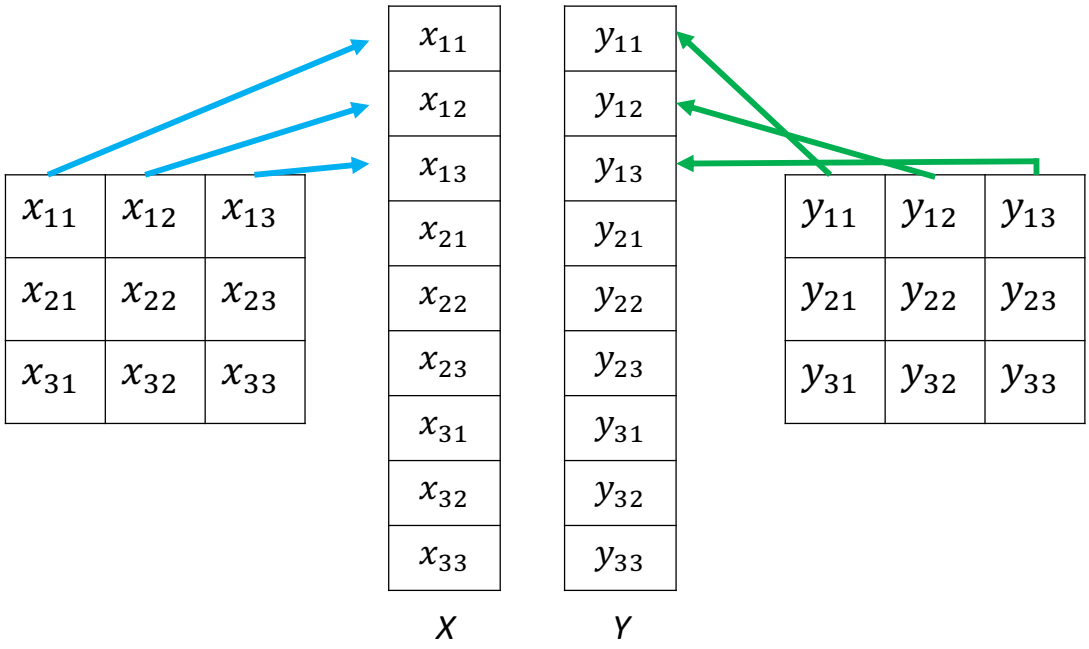

Figure 3.2: Flattening process for comparing two dimensional fields using Shannon entropy and mutual information. As the flattened arrays $x_1, x_2, \ldots$ and $y_1, y_2 \ldots$ might not have linear dependence on each other, using linear dependence measure such as Pearson correlation will yield incorrect results. Mutual information measures nonlinear correlations and hence captures

Here instead of using the new metric γ, we use its components: Shannon entropy and mutual information individually to compare variability between different simulations. Quantifying differences because of modifications in the extrinsic forcings may be required for coastal applications where systems vary predominantly due to external forcings (note that intrinsic variability is less than

half by both metrics in Figure 3.5). For these forcing significance experiments, OSOM was run after modifying the external forcings (Table 3.1). OSOM is forced by tides, river runoff, atmospheric winds and air-sea fluxes, etc. (Full details of the model can be found in Sane, Fox-Kemper, Ullman, Kincaid, and Rothstein, Sane et al.). For this comparison, we quantify the effects of altering forcing on 4 modeled variables: sea surface temperature and salinity, and bottom temperature and salinity. Four altered forcing sets were utilized, beyond set (1) Full set of atmospheric forcings using the North American Mesoscale (NAM) analyses, a data-assimilating, high resolution (12 km) meteorological simulation (https://www.ncei.noaa.gov/data/north-american-mesoscale-model/access/historical/analysis) denoted as FF. FF stands for full forcing. (2) Full set of atmospheric forcings but using the Northeast Coastal Ocean Forecast System (NECOFS) winds (Beardsley and Chen, 2014) instead of NAM, denoted as NECOFS. (3) River flows are replaced with their monthly-averaged flow, other forcing as in FF (4) River flows set to zero, other forcing as in FF. (5) Wind forcing set to zero, other forcing as in FF. These forcings have been tabulated in Table 3.1. The aim is to quantify the effect on total variability by removing or altering one of many processes which might contribute.

Forcing Set	Wind forcing	River forcing
FF	NAM	As Observed
NECOFS	NECOFS	As Observed
MR	NAM	Time-averaged
ZR	NAM	Zero river input
ZW	Zero winds	As Observed

Table 3.1: Different types of forcing combinations employed to test their effect on variability. FF stands for full forcing: winds, tides, rivers, etc. For more details see Sane, Fox-Kemper, Ullman, Kincaid, and Rothstein (Sane et al.). MR: mean rives; ZR: zero rivers; ZW: zero wind.

To evaluate Shannon entropy, the spatial output at a particular instant of time was rearranged into a row vector by a process called 'flattening' as shown in Figure 3.2. Land mask points

were removed. A variable x which is a two-dimensional variable was converted to one-dimension (flattened) by concatenation. Shannon entropy was found out for the flattened variable at each time step. Hence we get a time varying entropy of the surface or bottom variable and results for various types of forcings have been shown in Figure 3.10.

Mutual information was applied between the row vectors. The flattening process is shown in Figure 3.2. Our focus is towards a pragmatic approach on using information theory for simulation comparisons. For this article, the evolution of Shannon entropy and mutual information with to respect to time is not important. But relative comparison between mutual information values is what we seek. For example, if mutual information of surface salinity between FF and MR is higher than between FF and ZR, this implies the penalty for using time-averaged river runoff is not as severe as using zero river runoff. Replacing FF with MR will give better results than ZR. Small errors in river runoff flow rates won't cause appreciable changes to surface salinity than using zero rivers.

3.3 Results

3.3.1 Part A

Idealized Gaussian Arrays

We test our metric, γ, Equation 3.7 on synthetic data consisting of idealized arrays of Gaussian data: $\mathcal{N}(0, 1)$. For a normal Gaussian distribution Shannon entropy depends[2] only on the standard

[2] $H = \log_2 2\pi e\sigma^2$ is the Shannon entropy of a Gaussian distribution when probability density is continuous with σ as standard deviation. The Shannon entropy of a discrete probability distribution differs, which is inconsequential here but the reader is encouraged to read Jaynes (1962). Consistently here discretely sampled and binned probability distributions are obtained directly from data without any further parameterization.

deviation σ i.e. $H = \log_2\left(2\pi e\sigma^2\right)$. The variability in a Gaussian distribution can be increased or decreased by changing its standard deviation. Our goal is to compare γ and γ_{std}. We set out our numerical experiment as follows: we create 10 arrays, each having 10,000 elements drawn from a Gaussian distribution. Any two arrays from those 10 have a prescribed linear Pearson correlation coefficient from 0 to 1.

Thus, the 10 arrays covary linearly with a specified correlation coefficient. These 10 arrays represent each of 10 ensemble members from climate simulations. The mean of 10 members gives us the synthetic forced variability signal as would be determined from the model output; averaging over the 10 ensemble members reduces the contribution from uncorrelated variability and reaffirms the covarying component into the forced variability. We apply γ and γ_{std} on this synthetic ensemble by varying the prescribed correlation coefficient from 0 to 1. Figure 3.3 shows that as expected both metrics increase as the correlation decreases, i.e., as internal variability dominates forced. Both metrics behave similarly when correlation decreases, i.e. noise increases but γ is more sensitive as correlation tends to 1. This distinction is due to the logarithmic nature of Shannon entropy for Gaussian distributions–in essence, information measured in bits is not proportional to distance measured between distributions in terms of summed variance–in the examples following the consequences of this distinction will become clearer. Critically both functions are monotonic with correlation, however so relative comparisons (more intrinsic fraction in this region vs. that region) are preserved.

A second related experiment was derived from the first is also shown in Figure 3.3: adding outliers outside of the Gaussian distribution. 50 out of 10000 elements of each individual member were artificially corrupted (values were set to a constant value of 5) to test the sensitivity of both the

metrics. Figure 3.3 shows that γ is insensitive to outliers while γ_{std} is not. γ is not sensitive because outliers occur less frequently and hence do not affect the probability distribution much, especially with the prefactor in (3.1) and (3.2). Hence information theory metrics are robust in comparison to using standard deviation (or variance). If the outliers (extreme events) occur at higher frequencies, information metrics will naturally start sensing them even if they are discontinuous from the typical conditions (e.g., multimodal distributions). The above process was repeated for 100 ensemble members each sampled from Gaussian distributions. Increasing the number of ensemble members does not change the result qualitatively for both the experiments. The results for 10 members Gaussian ensemble are shown in Figure 3.3 a and for 100 members are in Figure 3.3 b.

Another set of experiment was done by using Uniform distributed data $U(-1, 1)$. The prescribed correlated vectors were created using the procedure outlined in Demirtas (2014). 10 and 100 ensemble members were created and γ and γ_{std} was found between the members and their mean. Results are shown in Figure 3.3 c, d respectively. The outlier had a value of 1.5. In all the cases, γ was less sensitive to outliers than γ_{std}.

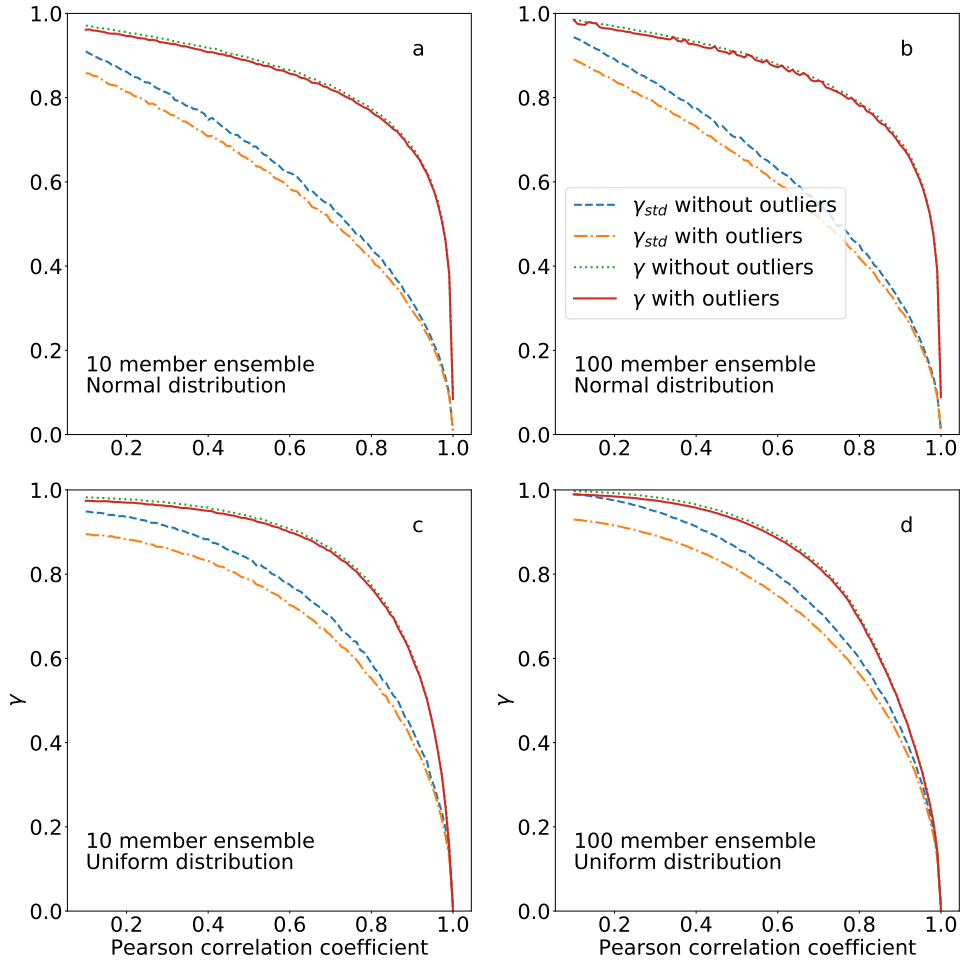

Figure 3.3: Information theory metric of intrinsic vs. extrinsic variability γ as a function of correlation coefficient in idealized Gaussian correlated arrays (a and b) and idealized uniformaly distributed arrays (c and d). The horizontal axis is the correlation coefficient between mean member and ensemble members. The vertical axis shows the information theory metric γ from Equation 3.7 and the traditional metric γ_{std} from Equation 3.10. A second related experiment adding (50 out of 10,000) "corrupted" outliers to each individual member is also shown. The information theory metric γ does not change for these outliers which shows its robustness while γ_{std} is highly sensitive. Results are similar for Gaussian distribution members and uniformly distributed members. γ is more sensitive towards linear correlation of 1. This is due to the logratihmic nature of γ.

Regional coastal model output

In this section we show the results of applying γ and γ_{std} on realistic simulation data from the Ocean State Ocean Model, hereafter OSOM (Sane, Fox-Kemper, Ullman, Kincaid, and Rothstein, Sane et al.). OSOM uses the Regional Ocean Modeling System (ROMS) (Shchepetkin and

McWilliams, 2005) to model Narragansett Bay and surrounding coastal oceanic regions and waterways. OSOM's primary purpose is for understanding and predictive modeling and forecasting of the estuarine state and climate of this Rhode Island body. Sane, Fox-Kemper, Ullman, Kincaid, and Rothstein (Sane et al.) gives more details about the model.

Using OSOM, an ensemble of simulations have been performed using perturbed initial conditions for the months July - August of 2006. This ensemble consists of 10 member ensemble. The data during the initial predictability window (20 days) has been ignored and the rest has been used to look at variability within the "climate projection" of the model beyond when forecasts sensitive to initial conditions are possible (see the related application of information theory to assess predictability in Sane, Fox-Kemper, Ullman, Kincaid, and Rothstein, Sane et al.). We examine whether the modeled temperature and salinity at each grid point follow normal distributions by evaluating the skewness and kurtosis of the ensemble mean at each grid point. Figure 3.4 shows skewness and kurtosis for sea surface salinity and temperature as well as bottom salinity and temperature for the Narragansett Bay region. The horizontal axis shows skewness and excess kurtosis, which are the third and fourth statistical moments respectively, normalized by powers of the standard deviation to dimensionless ratio and in the case of excess kurtosis a constant value of 3 is subtracted. For Gaussian distributions, skewness and excess kurtosis both should be close to zero. The vertical axis denotes the number of occurrences at a grid point. Observe that the majority of grid point values are away from zero. These variables are considerably non-Gaussian in OSOM. Thus, Equation 3.10 is at a disadvantage, because the prevalence of higher statistical moments implies that the variance does not contain a complete description of the variability. The information theory metric Equation 3.7 is suitable for such data as it takes into account higher moments and does not rely on

Gaussian distributions.

Figure 3.5 shows the ratio of intrinsic variability to total variability applied on every grid point for OSOM. γ is displayed on left whereas γ_{std} is shown on right for comparison. The features highlighted by both metrics are qualitatively different. The contribution of intrinsic chaos to total variability is more uniform using the γ metric than using γ_{std}. The intrinsic chaos displayed using γ_{std} might be misleading because the probability distributions are non-Gaussian. Furthermore, where the γ metric highlights internal variability tends to agree in similar dynamical locations–all river mouths show high surface salinity intrinsic variability. While surface temperature intrinsic variability is higher in more open regions of the Bay where eddies form intermittently due to varying topography. Also note that the ranges are quite different between γ and γ_{std}, but this is to be expected from the different rate of increase with correlation seen in Figure 3.3.

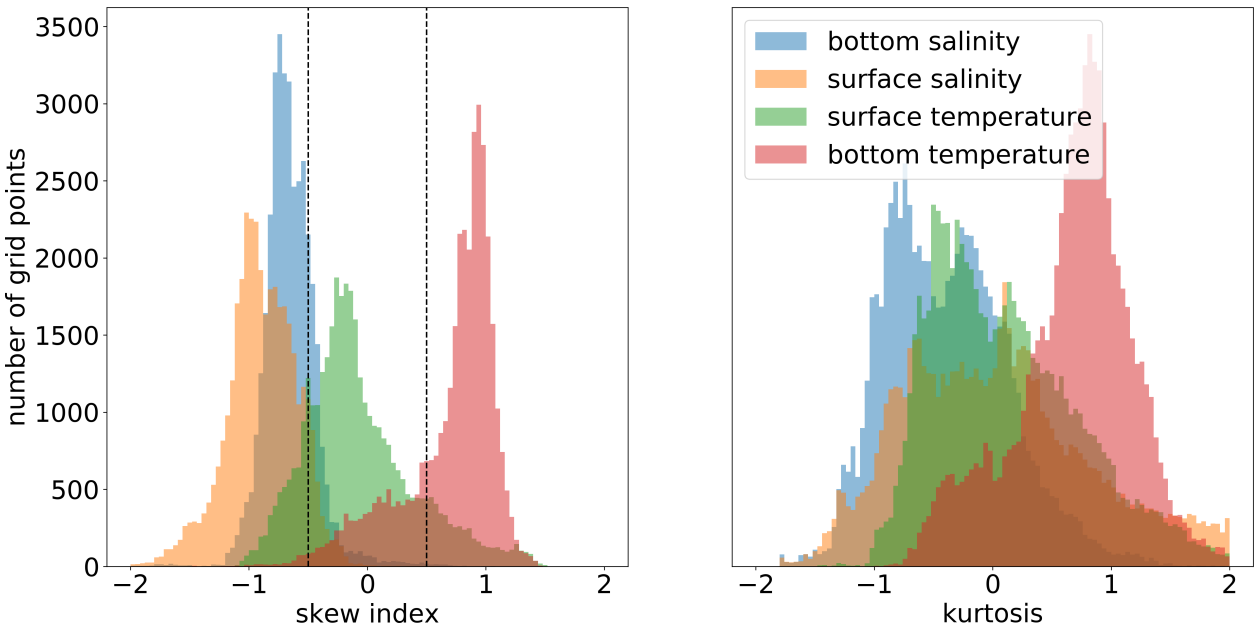

Figure 3.4: Grid point wise kurtosis for OSOM output. Kurtosis is not closer to zero within (-0.5, 0.5) suggesting the data distribution is non Gaussian.

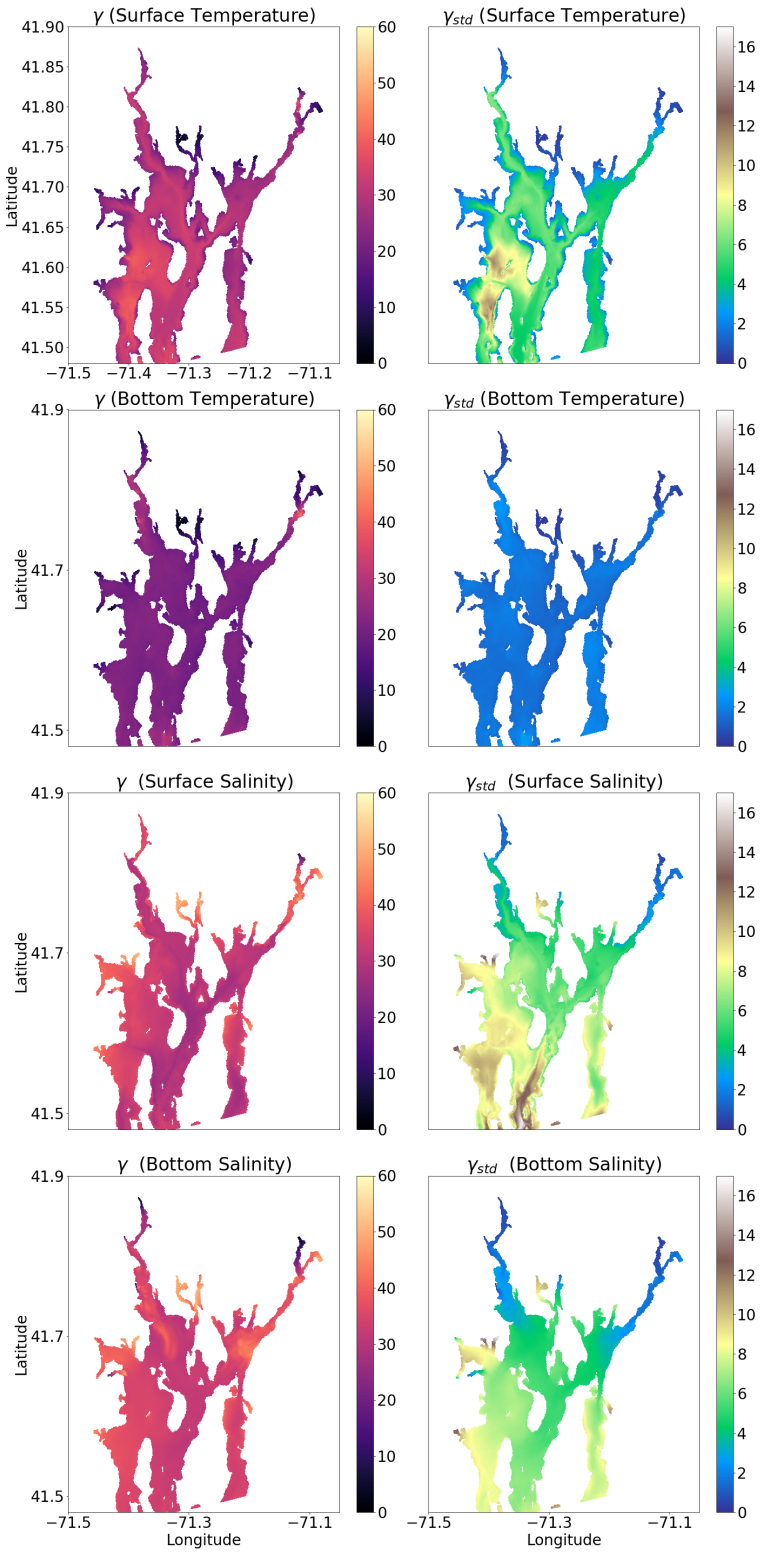

Figure 3.5: Metrics γ vs γ_{std} for OSOM output. Both metrics show different contribution of intrinsic variability to total variability. γ is more uniform throughout the domain than γ_{std}. Colormaps for γ and γ_{std} are different to highlight the different ranges each of them have. γ_{std} for bottom temperature has maximum value of 5%, and pattern is almost uniform except at the river sources where values are on the lower side (less than 1%).

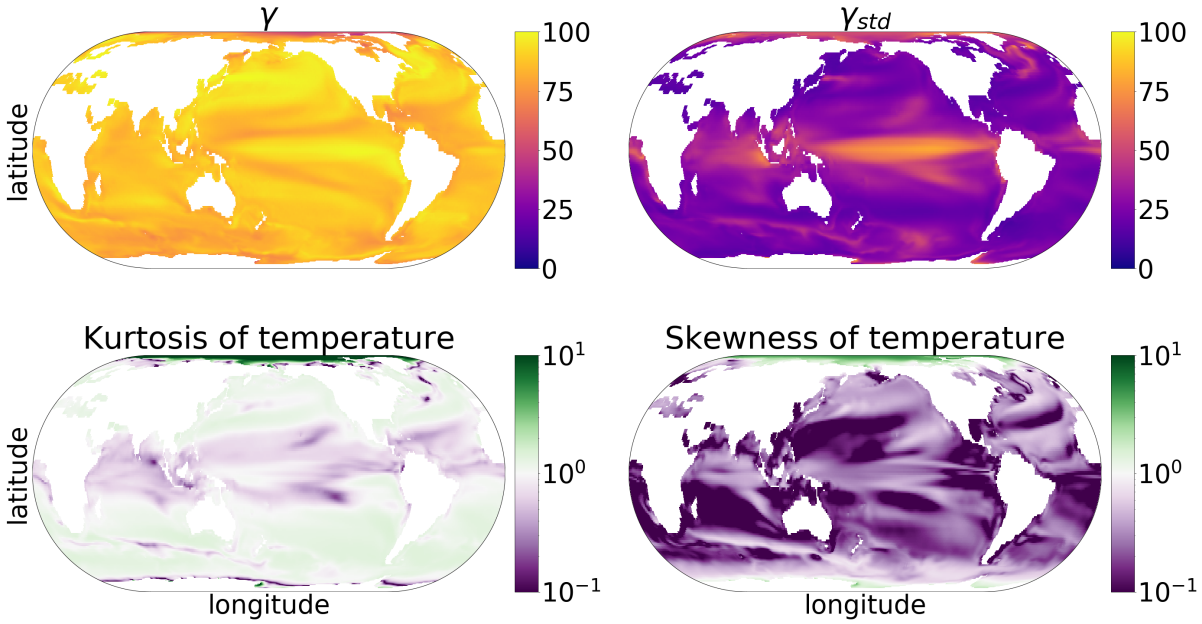

Figure 3.6: Top: Intrinsic to total variability percentage for sea surface temperature. Bottom: Excess kurtosis and skewness of the ensemble mean of temperature at each grid point. Values closer to zero (within 0.5 of zero, purple shades) are considered approximately Gaussian. The deviation of ensemble mean away from non normality implies that the ensemble members are also non normal. The Arctic regions have the most skewness and excess kurtosis implying non-Gaussian distributions.

Large Ensemble

A complementary experiment was performed by using γ to evaluate internal vs. forced variability in the global climate simulation output for climate change scenario RCP8.5 using the (randomly selected among the models compared) GFDL-LE model. All the 40 members from the ensemble were utilized. Variability of sea surface temperature (Figures 3.6) as well as sea surface salinity (Figure 3.7) were estimated using both γ and γ_{std} (upper left and upper right). Similar results were obtained for the detrended data for temperature (Figures 3.8) and salinity (Figures 3.9) The skewness and excess kurtosis of the ensemble mean were also plotted to find the deviation of variables away from Gaussian distributions (lower). Regions shaded in purple have low values of excess kurtosis and skewness and might be considered Gaussian. The detrended data shows higher

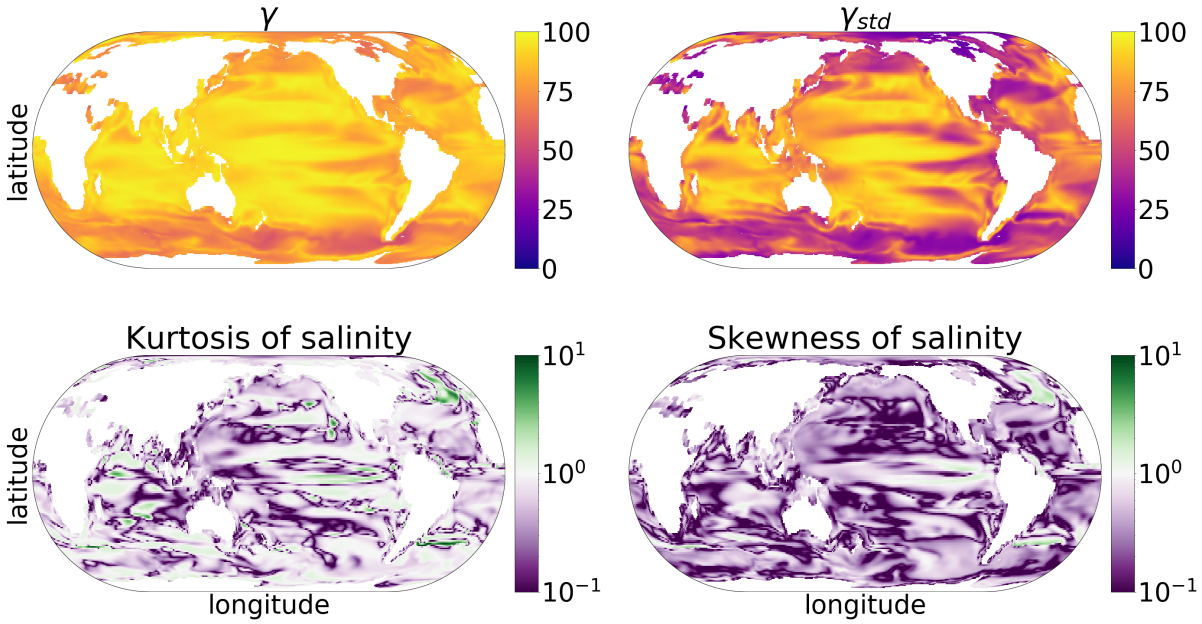

Figure 3.7: Top: Intrinsic to total variability percentage for sea surface salinity. Bottom: Kurtosis and skewness of the ensemble mean of salinity at each grid point. Values closer to zero (within 0.5 of zero, purple shades) are considered approximately Gaussian.

percentage of intrinsic variability than non-detrended data which suggests that detrended might have removed some poprtion of extrinsic variability.

Note in particular the Arctic sea surface temperatures, which have a highly skewed and excessive kurtosis distribution due to the freezing point of seawater. The standard metric deems this region to be among the most intrinsically variable in the world, while the information theory metric has it as a low intrinsic variability region. It is clear that a Gaussian metric should not be applied to this region, and the inference is opposite using the two metrics. In the equatorial Pacific where Gaussian statistics are more reliable, the two metrics agree that internal variability is high.

A less drastic failure occurs from the modest excess kurtosis in extra-tropical temperatures and in a few isolated regions in surface salinity. These regions are also non-Gaussian, but also are not heavily skewed (i.e., they are more long-tailed and intermittent than Gaussian). These regions

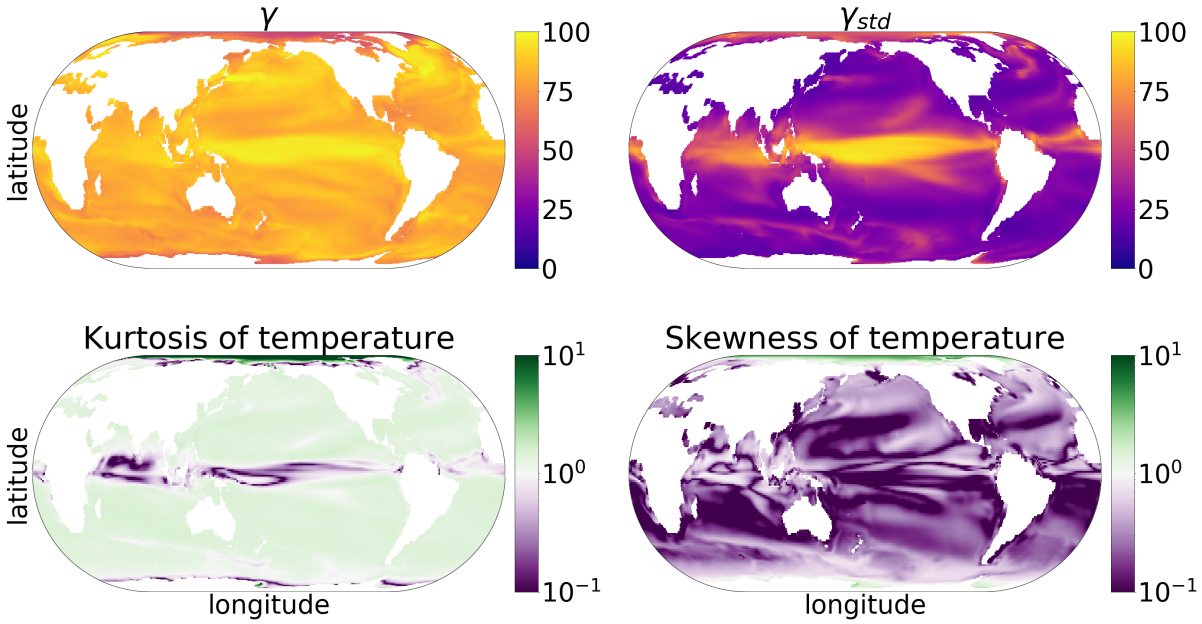

Figure 3.8: Top: Intrinsic to total variability percentage for detrended sea surface temperature. Bottom: Excess kurtosis and skewness of the ensemble mean of temperature at each grid point. Values closer to zero (within 0.5 of zero, purple shades) are considered approximately Gaussian. The deviation of ensemble mean away from non normality implies that the ensemble members are also non normal. The Arctic regions have the most skewness and excess kurtosis implying non-Gaussian distributions.

differ in relative estimation of intrinsic versus total variability. It is also the case that the γ metric is closer to one in most regions than γ_{std}, which is to be expected when the correlation coefficients are low from Figure 3.3.

3.3.2 Part B

Impact due to changes in boundary conditions in coastal model:

We show results in Figures 3.10 and 3.11. Entropy has been plotted with respect to time. In Figure 3.10, Shannon entropy is plotted for spatial quantities. For example, for surface salinity, all the surface values have been considered to find Shannon entropy using the flattening approach. Figure 3.11 displays mutual information. It is user's choice to choose the type of domain, here we

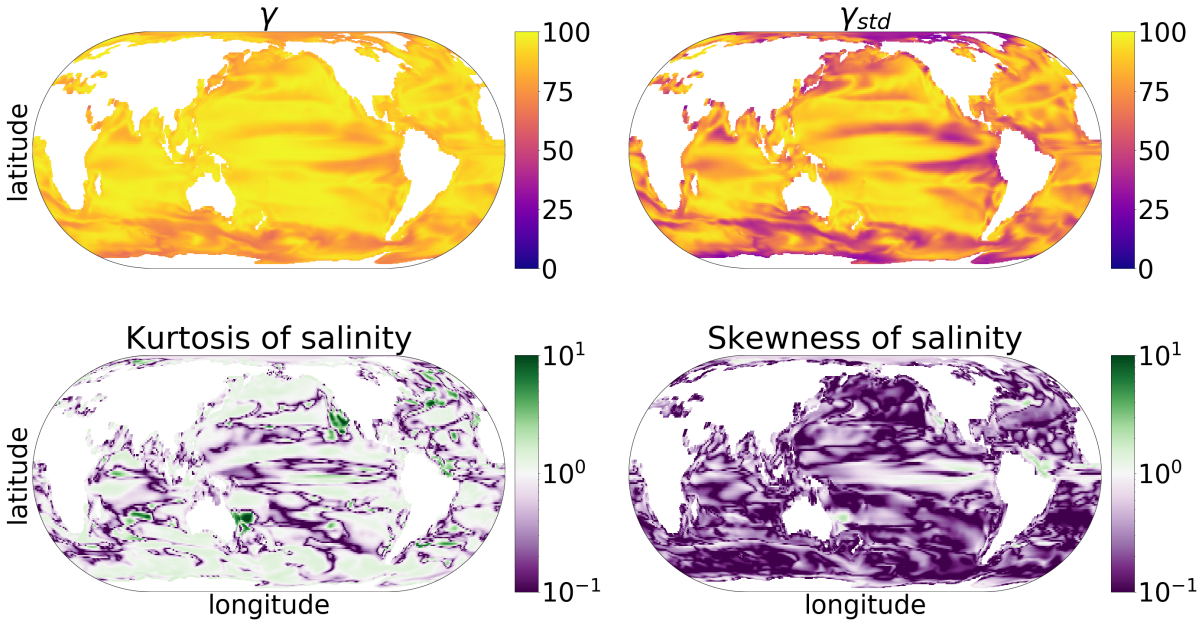

Figure 3.9: Top: Intrinsic to total variability percentage for detrended sea surface salinity. Bottom: Kurtosis and skewness of the ensemble mean of salinity at each grid point. Values closer to zero (within 0.5 of zero, purple shades) are considered approximately Gaussian.

have chosen the same domain of OSOM as shown in Figure 3.5. If Shannon entropy is more or less equal for two forcings, it implies they similarly affect variability. Mutual information should be compared for two pairs of forcings. Greater mutual information implies the two pairs share more *bits* of information, suggesting one of the forcing in that pair can be replaced with the other without significantly affecting variability.

3.4 Discussion

Our numerical experiments performed using γ on idealized Gaussian arrays show that γ is monotonic and decreases as the linear Pearson correlation coefficient increases. Thus aside from the qualitative differences the new metric finds when the data are non-Gaussian, the ranges of intrinsic versus total variability are quite different between γ and γ_{std}. This is to be expected from

the different rates of increase with correlation seen in Figure 3.3. Approximately, the traditional metric falls approximately linearly as the correlation coefficient increases, so that a correlation coefficient of 0.5 gives a γ_{std} just above 0.5. The new metric γ agrees with γ_{std} that correlation of 0 implies $\gamma = 1$, and correlation of 1 implies $\gamma = 0$, but correlation of 0.5 is closer to $\gamma = 0.9$. Only very near correlation coefficients of 1 does γ fall below 0.5. If roughly linear dependence on correlation coefficient is desired, γ can be raised to a power–γ^3 resembles γ_{std} and γ^6 resembles the correlation coefficient. These higher powers do not lose the ability to apply to non-Gaussian data nor become non-monotonic, but they will lose their interpretation as a ratio of bits of information entropy, and instead reflect ratios of bits cubed of information entropy, etc. An alternative is to take γ_{std} raised to a different power: $\gamma_{std}^{1/3}$ is roughly similar to γ.

As can be seen in Figures 3.5, 3.6, and 3.7, information theory metrics show different patterns as compared to variance. Information theory metrics, especially mutual information, account for *all* non-linear shared information between the ensemble members and the mean including linear correlation, and this is one reason for the differences. We have argued that non-Gaussian statistics are another (which is not wholly independent of non-linear shared relationships). There are likely other aspects of differences between these metrics, but the management of these two expected aspects of geophysical fluids–nonlinear relationships and non-Gaussian distributions–justify the introduction of the new metric.

For the regional coastal model OSOM, forcings differ as to how they affect different variables. As might be expected, river runoff is more important for salinity than for temperature. However, replacing rivers with the monthly-mean river flow gives nearly the same result (in terms of variability) as fully time-varying rivers. For the duration considered (July-August), averaging the river runoff

gives similar effect for salinity as compared to giving the observed river runoff in the simulations, see Figure 3.10. Temperature is less sensitive to any of the forcing alterations, because although temperature and salinity are passive tracers they have different sources and sinks. Switching the wind product from NAM to NECOFS does not have any significant effect on the sources or sinks of temperature or salinity, but switching the wind off definitely affects the parameters by eliminating wind-driven mixing altogether. Figure 3.11 shows that zero wind (ZW) simulations are markedly different than the rest in terms of *mutual information* (i.e., they do not covary), although very similar in terms of amount of spatial variability (Shannon entropy, Figure 3.10), because even without winds tides, fluxes, and rivers still vary. The zero river case tends to eliminate both variability and mutual information (ZR). Please note that our simulations are for July-August, and results might be different for different season.

If we were to prioritize improvements based on Shannon entropy and mutual information, note that the two highest mutual information cases are where NAM is substituted with NECOFS and where mean rivers are substituted for varying rivers. The first observation is important from a forecast perspective, because it means that we can not easily tell the difference between different wind products, although something rather than zero winds should be used if the estuary is forecast out to the full 20 day predictability range (weather forecasts only good out about 7 days in this region). Similarly, knowing that substituting the mean of the rivers for the fully varying rivers has little impact implies that rivers can be fixed in time for forecasts beyond where they might be predicted based on expected weather and precipitation. Finally, despite the fact that Narragansett Bay is a dominantly tidally-mixed estuary, among the sources of overall variability (i.e., sources of information entropy) considered, preserving an inflow of fresh water is key, even though that

inflow can be steady. Winds do not appreciably increase information entropy of the Bay, but they are an important source of forced co-variation, and so are important for predictions but do not raise the overall level of variability.

3.5 Conclusion

We have proposed an information theory metric to determine contribution of intrinsic chaos and external variability to total variability in ensemble model simulations. Our metric uses Shannon entropy and mutual information and has several advantages over using only standard deviation (or variance). We have applied our metric on idealized Gaussian arrays as well as realistic coastal ocean and global climate model. We conclude that:

1. The new information theory metric is more reliable when outliers are present, because outliers get assigned less probability and because Gaussian distributions have a difficult time approximating long-tailed (i.e., outlier prone) distributions.

2. The new information theory metric is more reliable when variability is non-Gaussian because it is based on non-parametric measures of the probability distributions.

3. The new information theory metric varies monotonically with ensemble member to ensemble mean correlation, but is quantified in fraction of bits required to capture internal variability versus bits required to capture of total variability.

4. The use of the information theory metric in a coastal ocean model ensemble and a climate model ensemble qualitatively changes the focus to regions that were previously erroneously labeled as having high or low internal variability.

5. In this case, the coastal ensemble had a much smaller intrinsic (chaotic) proportion of its total variability in comparison to the climate ensemble had more intrinsic (weather, climate oscillations, etc.) as a proportion of its total. Importantly, the resolution of the models helps determine the proportion of intrinsic variability, so such comparisons are model-specific: a higher resolution coastal model might well have a larger intrinsic fraction than a coarser climate model.

Acknowledgments

The Rhode Island Coastal Ecology Assessment Innovation & Modeling grant (NSF 1655221) supported this work. BFK was also supported by ONR N00014-17-1-2963 and NSF 1350795. This material is based upon work conducted at a Rhode Island NSF EPSCoR research facility Center for Computation and Visualization (Brown University), supported in part by the National Science Foundation EPSCoR Cooperative Agreement #OIA-1655221.

Data statement

All the data and the codes used to plot results can be downloaded via Brown University's digital archive DOI: urlplaceholder.

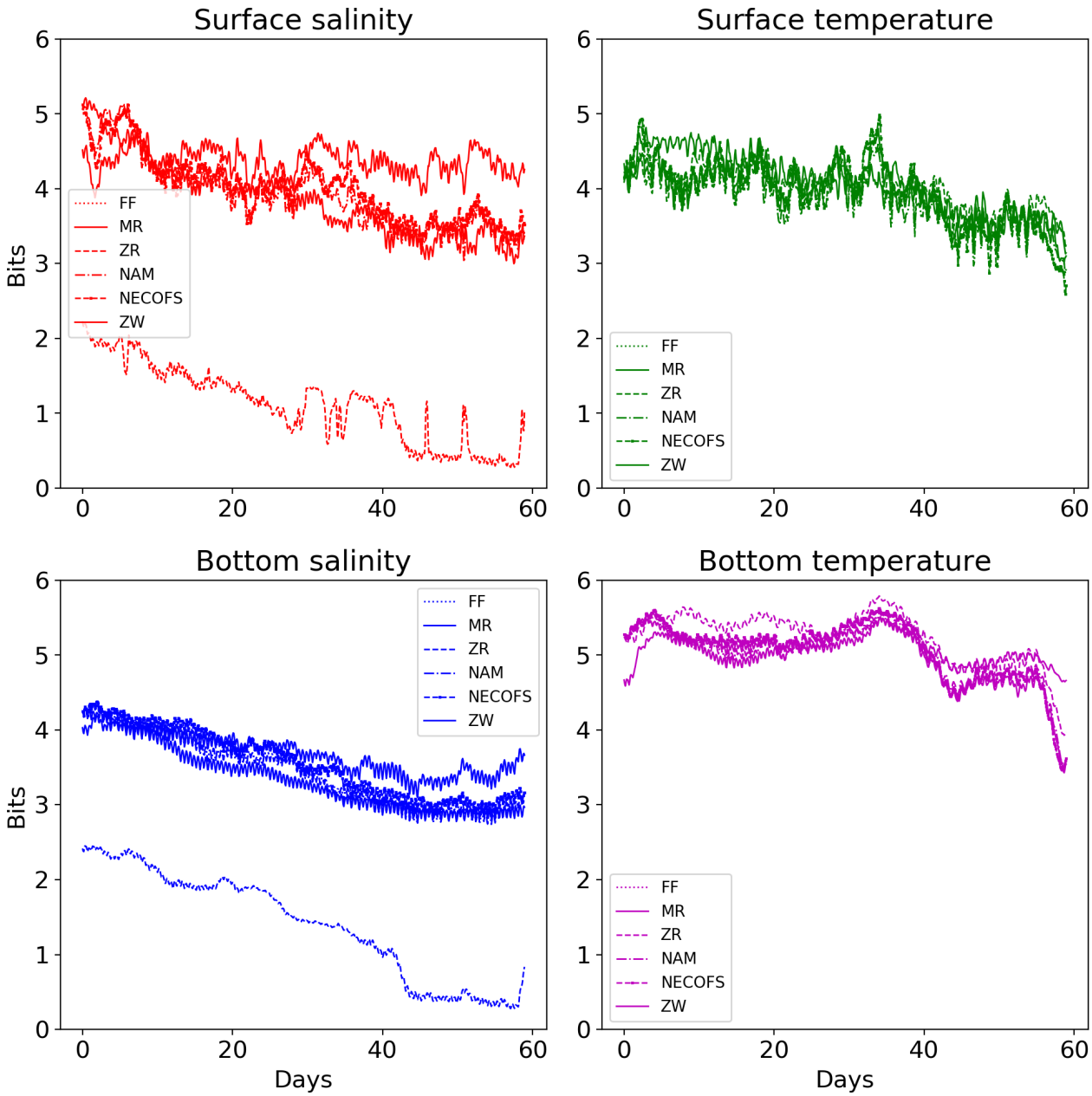

Figure 3.10: Shannon entropy applied to temperature and salinity. Replacing fully time varying rivers with monthly-mean river flow gives almost the same result for salinity. Same is true by replacing wind product with a different one. Rivers set to zero affects salinity but not temperature. Winds are important in terms of variability but different wind products do not noticeably alter variability.

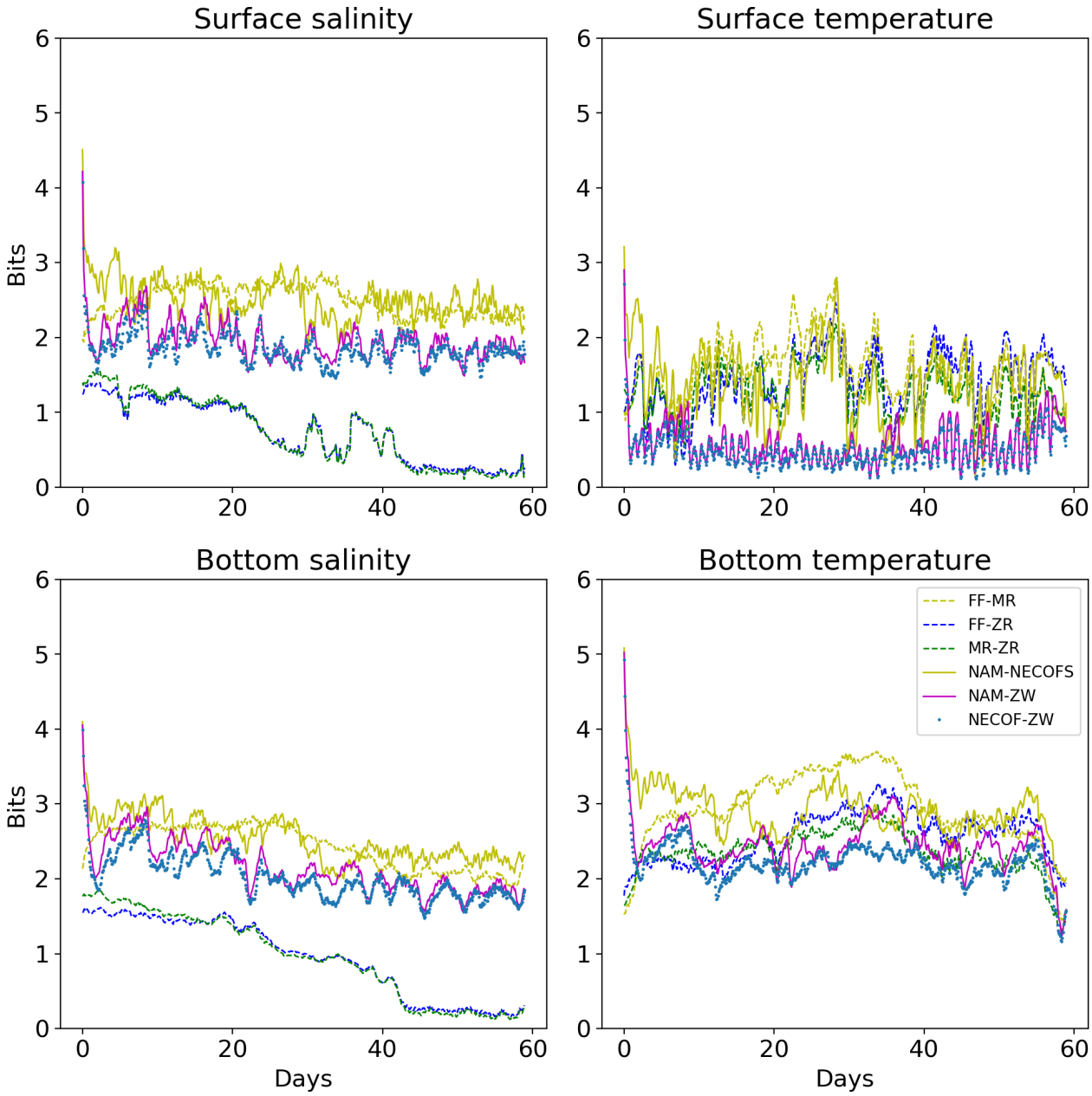

Figure 3.11: Mutual information applied to simulations from different forcings. Higher mutual information implies higher similarity in terms of variability. For example NAM-NECOFS values are higher than NAM-ZW implying that NAM and NECOFS are significantly different than having no wind.

Chapter 4

Parameterization

Preface to Chapter 4

Chapter 4 is a draft of a manuscript in preparation. It describes the results of using different paramterizations in OSOM. I have peformed the simulations for the three cases: GLS, KPP, and SI and documented the results in this chapter. The manuscript will develop subsequently and will be co-authored by Baylor Fox-Kemper, Jihai Dong, and Leah Johnson with a possibility of more co-authors. The SI scheme developed by Bachman et al. (2017) has been implemented in CROCO by Jihai Dong.

4.1 Introduction

In the previous chapters, the predictive capacity of OSOM was described and the model output was compared with the observations from buoys. Vertical mixing was represented using the GLS

turbulence paramterization scheme. The model shows high skill, skill being defined by how close the output is with the observations. Although the model output displays high skill, as observations are sparse, the grid points only near the buoys can be compared. The question of model accuracy away from the buoy sites is difficult to answer, but the model's sensitivity to different vertical mixing schemes can be checked. The level of agreement of the model among the different paramterization schemes should provide an insight into the physical processes as the various paramterizations are physics based and try to accurately represent turbulent eddy diffusion. Hence, it is pertinent to check OSOM's performance for different vertical mixing schemes.

Different mixing parameterizations should result in similar mixing for the same physical forcing conditions, but vertical mixing parameterizations are known to disagree (e.g. Li et al., 2019). I have modelled OSOM using CROCO and compared CROCO-OSOM's output using three different vertical mixing schemes: GLS (Umlauf and Burchard, 2003) , KPP (Large et al., 1994) and modifed KPP (Bachman et al., 2017), hereby reffered to as GLS, KPP, and SI schemes respectively. CROCO (`https://www.croco-ocean.org/`) (Shchepetkin and McWilliams, 1998; Haidvogel et al., 2000; Marchesiello et al., 2001; Ezer et al., 2002; Marchesiello et al., 2009; Lemarié et al., 2012,?; Soufflet et al., 2016; Ménesguen et al., 2018) is derived from ROMS, specifically from ROMS-AGRIF, and apart from all the technological advancements of ROMS it has the option to use non-hydrostatic set of equations. Non-hydrostatic equation uses the momentum equation in z-direction to evolve w velocity, and pressure is not a function of depth alone. The non-hydrostatic feature has not been used in the current version CROCO-OSOM, but will be left for future work which might involve nested grids with higher resolutions. The K-Profile Parameterization (KPP) is a first order closure and models the effects of surface stress, boundary

layer depth, and bouyancy flux. It uses a shape function and surface boundary layer depth to estimate tubulent eddy diffusivity/viscosity. More details can be found in Van Roekel et al. (2018, Appendix B). The GLS scheme stands for Generic Length Scale and uses a two equation turbulence closure model. It was proposed by Umlauf and Burchard (2003) and was introduced in ROMS in Warner et al. (2005b).

In typical oceanic conditions, vertical displacements are stabilized due to stable stratification and rotation puts a constraint on horizontal perturbations (inertial stability). One may think these two constraints are the only two ways in which a fluid parcel can be stable or unstable. However, in the cross-frontal plane, there is an instability which slips through the cracks of the above vertical and horizontal stability barriers. This instability occurs along the isopycnal direction, even when the parcel is stable in vertical and horizontal directions, and can be termed as the isopycnal inertial instability, or isentropic inertial instability to be more general. An astoundingly precise explanation of symmetric instability can be found in Holton (Holton, p. 279).

Symmetric instability occurs when the Ertel potential vorticity, given by

$$q = (f\mathbf{k} + \nabla \times \mathbf{v}) \cdot \nabla \mathbf{b}, \tag{4.1}$$

has the opposite sign to local Coriolis paramter, f (Hoskins, 1974). $\mathbf{k}$ is the local z-direction, $\mathbf{v}$ is the velocity vector, and ∇b is the buoyancy gradient. Weak stratification and strong horizontal fronts causes PV to shift towards anticyclonic values and results in symmetric instability. The symmetric instability might be a dominant mechanism in the cross-frontal direction mixing (Wenegrat et al., 2020) and it occurs on the scales of $O(10\text{ m} \sim 1\text{ km})$. These conditions for fronts exist in the

domain of OSOM.

KPP and GLS boundary layer mixing schemes are one dimensional along the vertical and do not include lateral effects or lateral variability. A range of processes arise when lateral density gradients are considered. OSOM resolves wavelengths for some instabilities such as baroclinic instabilities, while symmetric instability cannot be resolved with the current resolution. The SI scheme uses the symmetric instability paramterizations introduced in (Bachman et al., 2017). It has been implemented in CROCO by Dong et al. (2021). CROCO has GLS and KPP inherited from ROMS. The SI scheme modifies the existing KPP paramterization and switches between SI and KPP mode as per the physical constraints explained in Dong et al. (2021). The scheme detects negative PV and drives the flow towards neutral SI values by extracting energy from the geostrophic shear. More details can be found in Bachman et al. (2017). All the three schemes set the vertical diffusivities, and when conditions for SI are not met, the SI scheme reverts back to KPP until the conditions favor SI.

4.2 Methods

CROCO-OSOM was ran for the month of March (March 9 to 25). Winter durations show deeper mixed layer depths. December, January, and February simulations showed the presence of a mixed layer extending throughout the water column in the region. In well mixed columns in coastal systems, it would be difficult to detect the effects of SI scheme because vertical paramterizations modulate the mixed layer depth (and the boundary layer depth). To see differences in shallow water systems, the mixed layer or boundary layer depth should be observable, that is $0 < h_{mld} < h_o$, where h_o is the total depth at a location. Hence the month of March was chosen to observe the effects of

symmetric instability as the higher surface temperatures would strenghten the stratification in the water column. All the three cases were started with the same initial conditions.

A sub-domain of OSOM was chosen to observe the effects of different paramterizations. This sub-domain was chosen based on the differences in the vertical viscosities observed in the model output. The choice of subdomains have been explained in Figure 4.1. The bigger subdomain consisting of Rhode Island Shelf, shown in red color, has been used to compare surface temperature and boundary layer depth. The smaller subdomain which is a region near Aquinnah in Massachusetts, displayed in orange color, is used for PV. Difference in viscosity is an evidence of SI paramterization being active, hence symmetric instability is present.

For each time-stamp, the two dimensional or three dimensional spatial fields were"flattened" and converted to a single column vector and compared by using Shannon entropy and mutual information. The flattening approach has been described in Section 3.2.2. Shannon entropy has been found individually for every case, while mutual information was found between every two out of the three cases (GLS-KPP, KPP-SI, GLS-SI).

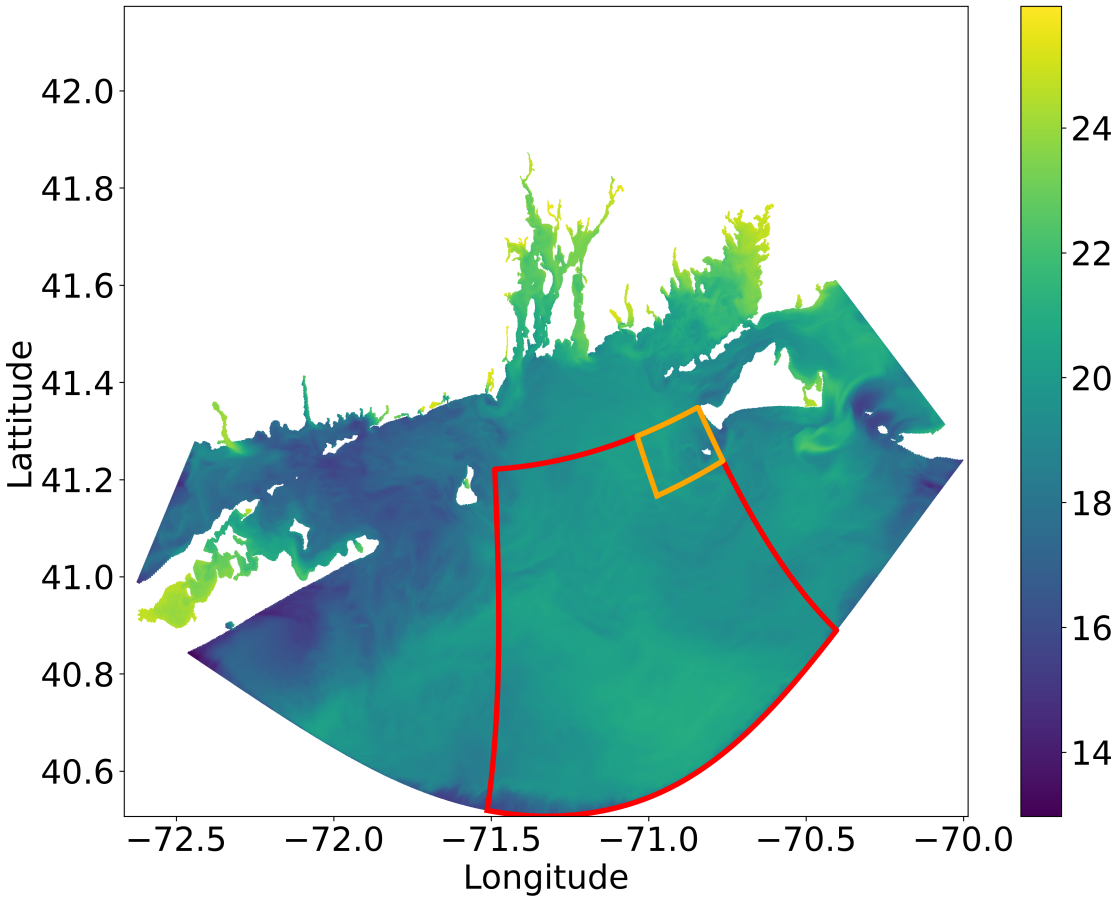

Figure 4.1: OSOM region modelled in CROCO. The Rhode Island Shelf region (red colored rectangle) extending from ≈ 40.5 to ≈ 41.3 lattitude is the subdomain used to compare surface temperature and boundary layer depth. The region near Aquinnah (orange colored rectangle) extending from ≈ 41.1 to ≈ 41.3 lattitude is used to compare PV.

4.3 Results

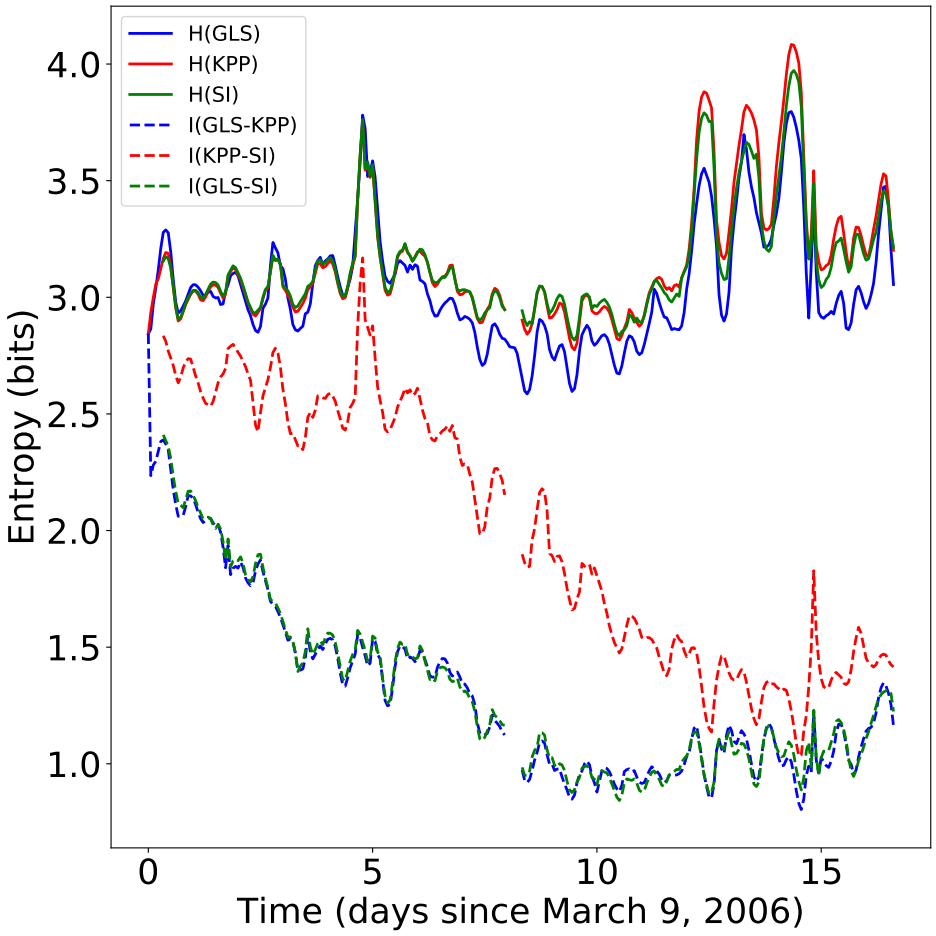

Figure 4.2: Shannon entropy and mutual information of surface temperature.

Figures 4.2 and 4.3 show the entropies of surface temperature and boundary layer depth for the region shown by orange colored rectangle in Figure 4.1. All the entropies start from the same value at $t = 0$ (March 9, 2006) since all the three cases have the same initial condition. For temperature, the total spatial variability given by Shannon entropy is close to each other for all the three cases. The mutual information between GLS-SI and GLS-KPP decreases indicating that GLS causes considerably different evolution of temperature. Mutual information between KPP-SI oscillates without a trend for $t < 5$ days which might indicate a background impact of SI, before

the SI paramterization effects accumulate enough to cause a deviation due to the intrinsic chaos. Beyond $t > 5$ days, MI drops down implying disagreement between KPP and SI.

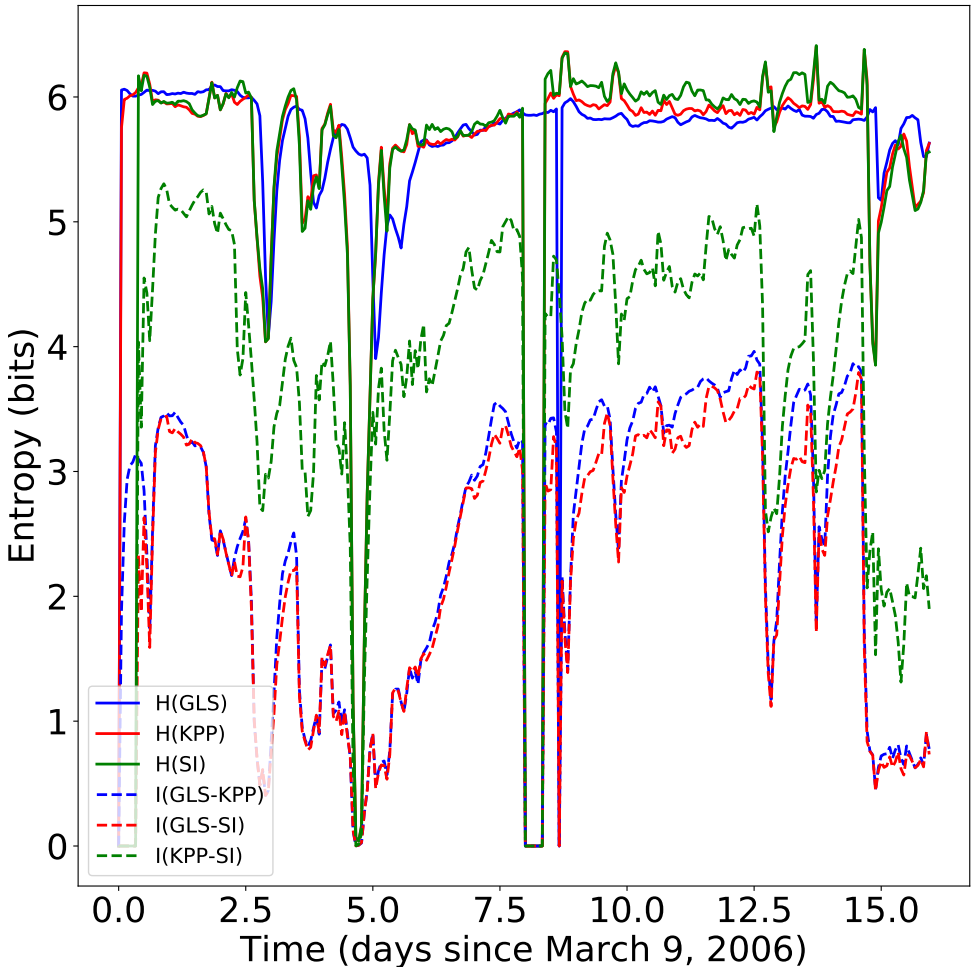

Figure 4.3: Shannon entropy and mutual information of boundary layer depth.

For the boundary layer depth, the Shannon entropy result shows similarities with temperature as shown by Figure 4.3. Shannon entropy of GLS, KPP, and SI attains similar values for the entire duration. The mutual information between KPP-SI is always higher than GLS-KPP and GLS-SI indicating the boundary layer depth from SI and KPP schemes is closer to each other than GLS scheme. The changes in the Shannon entropy seem to affect the mutual information for $t < 12.5$. For $t > 12.5$, mutual information is de-correlated from Shannon entropy suggesting changes in

mixing due to the intrinsic effects.

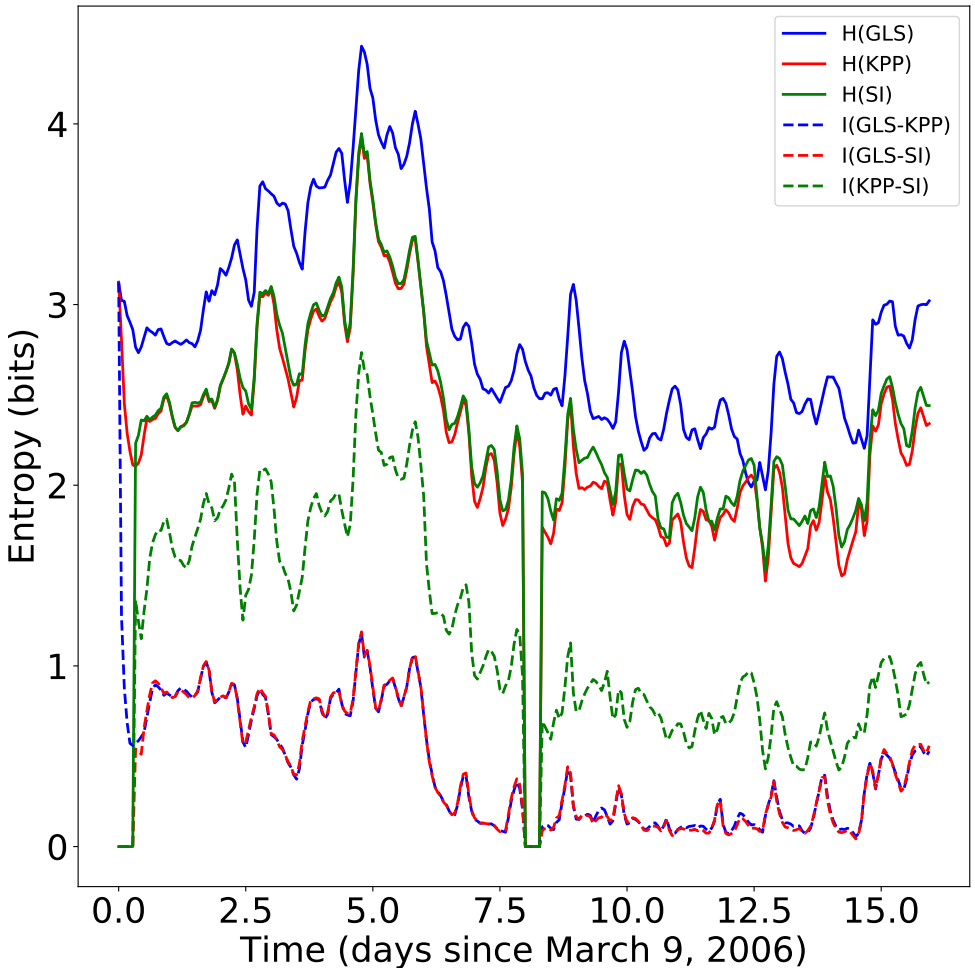

Figure 4.4: Shannon entropy and mutual information of PV.

The results for PV (Figure 4.4) are similar indicating GLS shares the least information with KPP or SI scheme. Shannon entropy for GLS is higher than KPP and SI implying wider distribution of PV under the GLS scheme. KPP and SI seem to contrain the Shannon entropy of the PV.

4.4 Discussion

GLS and KPP schemes use different approaches for parameterizing vertical mixing. The differences in surface temperature, PV, and boundary layer are due to the different vertical viscosities (diffusivities) set by the respective schemes. The SI scheme is a modification of the KPP scheme and gets activated only under certain physical constraints. These constrains involve the sign of PV and the location of the grid point below the surface (Bachman et al., 2017). Symmetric instability occurs when the sign of PV is negative, and SI scheme works to make PV positive and extracts kinetic energy from the mixed layer. Hence, the variation between SI and KPP occurs due to the treatment of PV. GLS is remarkably different from KPP and SI. $I(KPP; SI)$ shows high values, close to $H(KPP)$ or $H(SI)$ implying symmetric instability is not the dominant mixing mechanism in the bay. $\partial I(KPP; SI)/\partial t < 0$ for some points in the figures, which might substantiate the presence of symmetric instability. Hence, symmetric instability although not dominant, is definetely active in the region. $\partial I(KPP; SI)/\partial t > 0$ might indicate switching off of SI scheme and activation of KPP. GLS and KPP are vertical mixing schemes and only focus on effects in the vertical direction. SI scheme takes into account horizontal PV and is aware of strong horizontal fronts. The activation of SI scheme hints at the presence of strong fronts and strong horizontal buoyancy gradients. The changes in forcing at $t > 12.5$ affect the boundary layer depth agressively than surface temperature and PV. This requires a careful analysis of the forcing conditions for that duration.

Non parametric approaches like information entropy are useful for physical quantities which are bounded between a minimum value and a maximum value. In our case, the boundary layer depth is bounded by $z = 0$, the surface, and $z = h_o$, the sea floor. They have a strict cutoff and boundary layer depth (and mixed layer depth) can only vary between these two values. This is

similar to the Artic ocean temperature which is bounded on one side.

4.5 Conclusion

Symmetric instability is present in the Rhode Island sound, but might not be dominant mechanism of mixing. Distance as measured by information theoretic metric show that GLS is more distant from KPP and SI than SI is from KPP. In terms of mutual information, KPP and SI share more common information with each other than with GLS. As SI shows similar results to KPP, neglecting the effects of symmetric instability would not be detrimental to model the physcial processes happening in the domain, but this requires a thorough analysis and verification. It is necessary to exercise judgement and compare with observations when selecting either KPP or GLS, but not so in between KPP and SI as is evident from mutual information values of all the variables analyzed. The changes in the evolution of entropis are due to different vertical mixing schemes, but can also be due to advection and lateral mixing from the East-West-North-South boundaries of the subdomains (red and orange rectangles) displayed in Figure 4.1. As the regions outside the subdomains also evolve with the respective schemes, the dominant cause of difference among the three cases are the different parameterizations.

Chapter 5

Conclusions

5.1 General conclusions

Regional modeling is an emerging field and is gaining focus due to the importance of coastal systems in our daily lives. In contrast to global climate models, different regional models are unique in their own way and have utility in estimating the local impacts of climate change. As such, forecasting and predictability of coastal models is an emerging field. This present work provides a framework to find the predictability time scales of such coastal models. This is the first work of its kind where information theory metrics have been used on a regional model to estimate predictability, variability, impacts of forcing sensitivity and choice of turbulence parameterizations. Information theory holds a promise for providing us with a set of non parametric and dimension agnostic metrics. Although it has been generally known in the coastal community that the predictability of regional models is short (few days), the current work quantifies that predictability.

Focus has been on the practical application of information theory metrics. Previous literature

related to using information theory metrics in climate modeling does not clearly present the methodology especially for a limited number of ensemble members. This created a knowledge gap of how to use the information theory for analyzing outputs from regional models and climate models where forcings play a pertinent role and chaos is low to moderate. The present work has attempted to bridge this gap by providing a viable framework which can be easily replicated and improved upon.

Regional models are being refined towards finer spatial resolutions and same applies to global climate models. The methods presented in this manuscipt are future-proof, implying the techniques will work in more chaotic models under different types of forcings. As the methods introduced are not based on the type of the model, the techniques have very high fidelity. The techniques show high fideility as they are not dependent on the type of model (global or regional, high or low resolution, etc.)

5.2 Specific conclusions

1. Potential predictability timescale of OSOM has a range of 6.9 to 40.5 days for temperature and salinity. It varies with season and region.

2. Flushing time scales are consistent and quantitatively similar with the predictability timescales.

3. OSOM shows adequate skill. Improving model accuracy might not affect predictability time scale, but will increase forecast skill.

4. Mutual information captures differences between forecast and climatology and is useful to quantify predictability. Metrics can apply to physical, biogeochemical, etc. variables with

limited ensemble members.

5. For estimating intrinsic and extrinsic variability, a new metric has been proposed which uses mutual information and Shannon entropy. It is non-parametric, robust in the presence of outliers, and reveals regions of high or low intrinsic variability as compared to variance metric.

6. Intrinsic to total variability ratio γ is model specific. ROMS-OSOM shows less overall intrinsic variability than a global climate model. Unlike bias maps, γ captures both changes to mean and variance and can utilize multiple variables with different units to highlight major impacts.

7. Mutual information and Shannon entropy identify the cost of using one parameterization or one forcing over the other in the unit of bits. Changes in variability across different physical variables due to changes in forcings or parameterizations can be compared.

8. Symmetric instability is active but might not be the predominant mechanism of mixing in the domain modeled by OSOM.

9. Uncertainty in boundary layer mixing in OSOM is greater than the impact of symmetric instability.

5.3 Future Work

1. For ROMS-OSOM, results for point-wise predictability timescales show similarity with zone-averaged field's predictability timescale, hinting towards a well mixed and stirred oceanic conditions. It needs to be checked whether this is a feature of the ROMS-OSOM or Narra-

gansett Bay.

2. Flushing time scales assume the bay is a constantly stirred well mixed reactor. More detailed flushing time scales for fresh and saline water can be estimated by introducing passive tracers and floats inside OSOM. If ROMS-OSOM behaves as a well-mixed system, the flushing of passive tracer will happen on the same timescale as those evaluated in Chapter 2.

3. The fluxes shown in Figure B.1 in Appendix B warrants an investigation of the scaling law being followed in the estuary.

4. How closely is the intrinsic variability linked with predictability? Increasing the model resolution, might decrease the predictability time scale but needs more scrutiny.

5. Ensemble modelling of the biogeochemical (BGC) variables can be performed similar to the physical variables. Information theory metrics will reveal the sensitivity of BGC variables to perturbations in initial conditions. Mutual information can be applied between two variables having different units. For example, mutual information between phytoplankton and salinity will disclose correlations and can be compared with a different set of variables (say phytoplanton and temperature). A rich set of total correlations can be obtained for the entire OSOM domain. Time series data from the observations could also be employed.

6. A method to compare the effect of altered forcings on physical variables was demonstrated in Chapter 3. The same technique can be applied to BGC variables.

7. In Chapter 4, γ and γ_{std} disagreed except at the extremes, 0 and 1 correlation coefficient. Using an inverse method they can be matched by raising to higher (or lower) powers to investigate their significance.

8. CROCO-OSOM's skill with KPP and SI scheme should be investigated. Changes in vertical eddy viscosity in SI scheme were observed near the South edge of the OSOM's domain surmizing PV injection through the boundaries. Can expanding the domain by shifting southern boundary show more SI activity?

9. Porting OSOM to CROCO opens the possibility to perform non-hydrostatic simulations alongwith nested grids. Effect of non-hydrostatic modelling on model skill, predictability, variability, and mixing can be explored.

10. Use of information theory in geosciences is a growing field (Kumar and Gupta, 2020; Perdigão et al., 2020) and there is a potential for using recent advances such as information flow, information physics, etc. in analyzing coastal systems and regional and global ocean models.

Appendix A

Supplementary material for Chapter 2

Supporting Information for “Consistent Predictability of the Ocean State Ocean Model (OSOM) using Information Theory and Flushing Timescales"

Contents of this file

1. Figures S1 to S37.

2. Table S1

Introduction

Text S1. The supplementary information contains Figures A.1 to A.25. All the figures have been quoted in the main text. Also, Table A.1 shows root mean square error between model run and observations for surface temperature and salinity as well as bottom temperature and salinity.

Table A.1: Root mean square error between observation and a single unperturbed model run

	Temperature ^{o}C		Salinity	
	Surface	Bottom	Surface	Bottom
CP	1.55	1.43	2.69	0.91
BR	2.42	1.26	3.4	1.24
NP	1.13	0.75	2.38	0.74
MtV	1.01	1.07	1.88	0.86
MtHB	1.87	0.77	2.02	0.94
QP	1.03	2.34	2.34	0.43
PP	0.91	0.82	2.91	0.59
GB	0.89	1.21	3.28	1.7

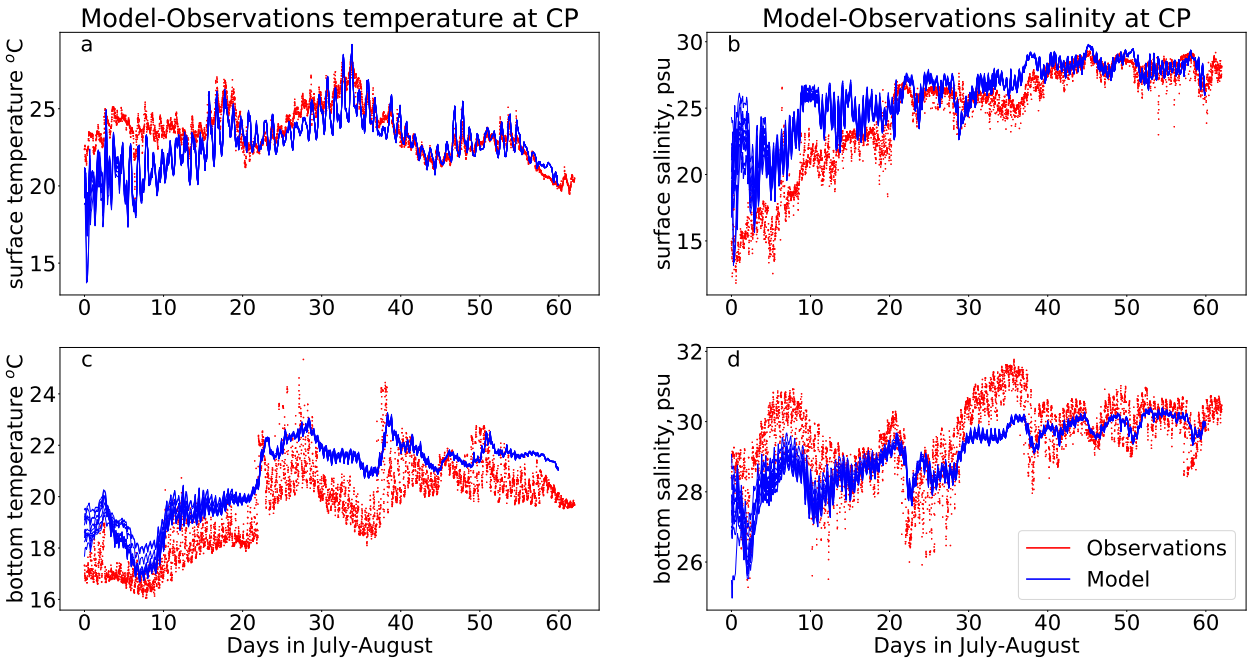

Figure A.1: Comparison of model with observations collected at Conimicut Point (CP).

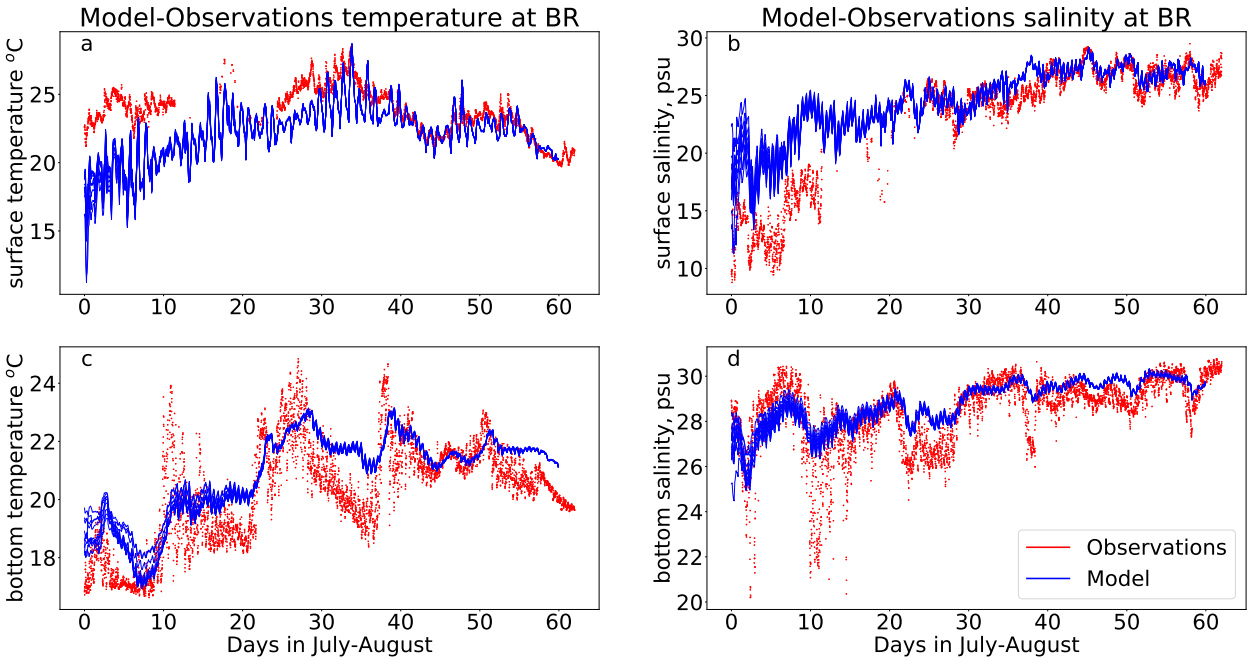

Figure A.2: Comparison of model with observations collected at Bullock's Reach (BR).

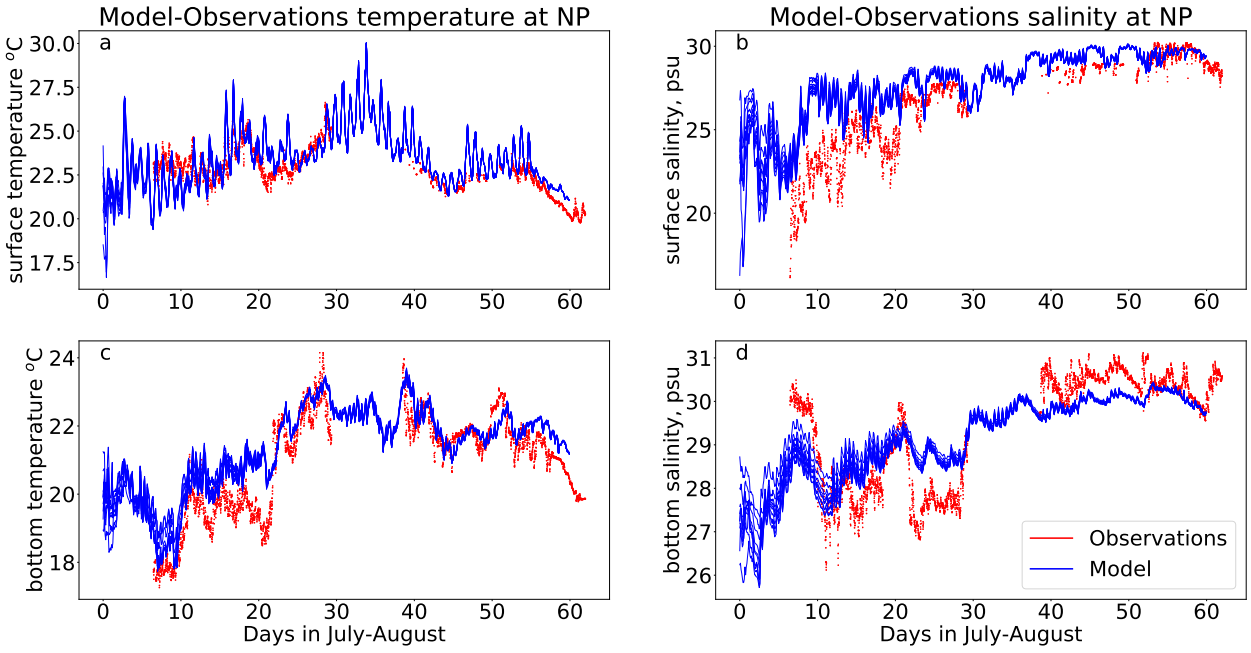

Figure A.3: Comparison of model with observations collected at North Passage (NP).

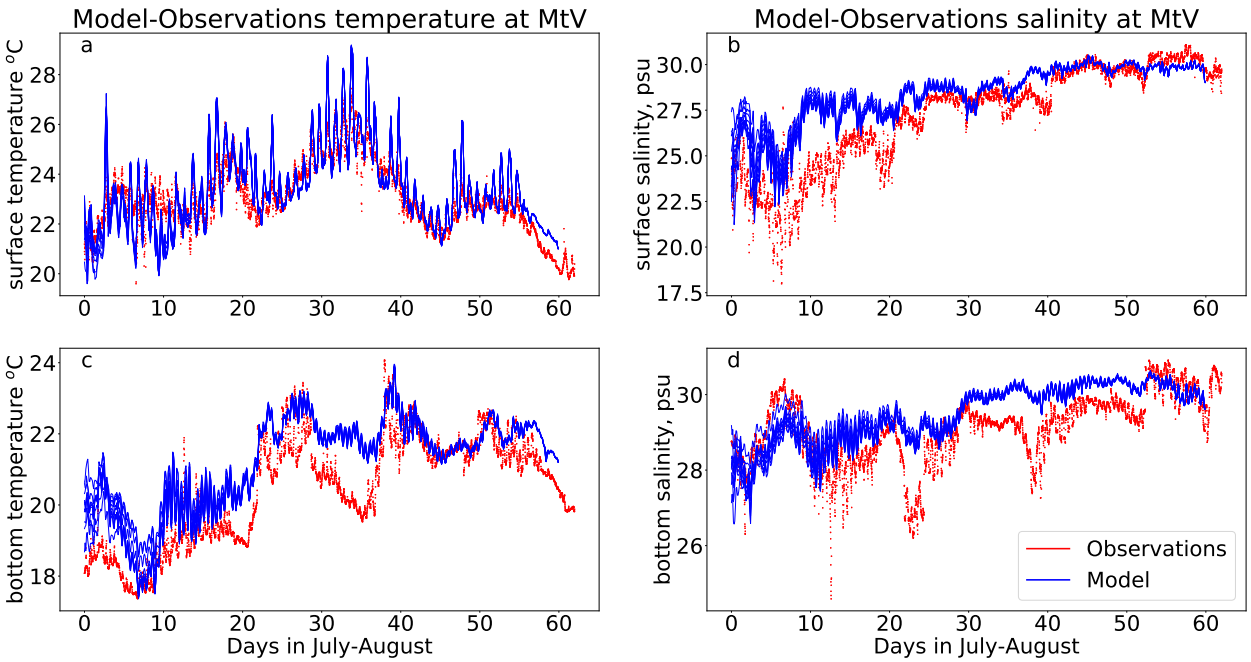

Figure A.4: Comparison of model with observations collected at Mount View (MtV).

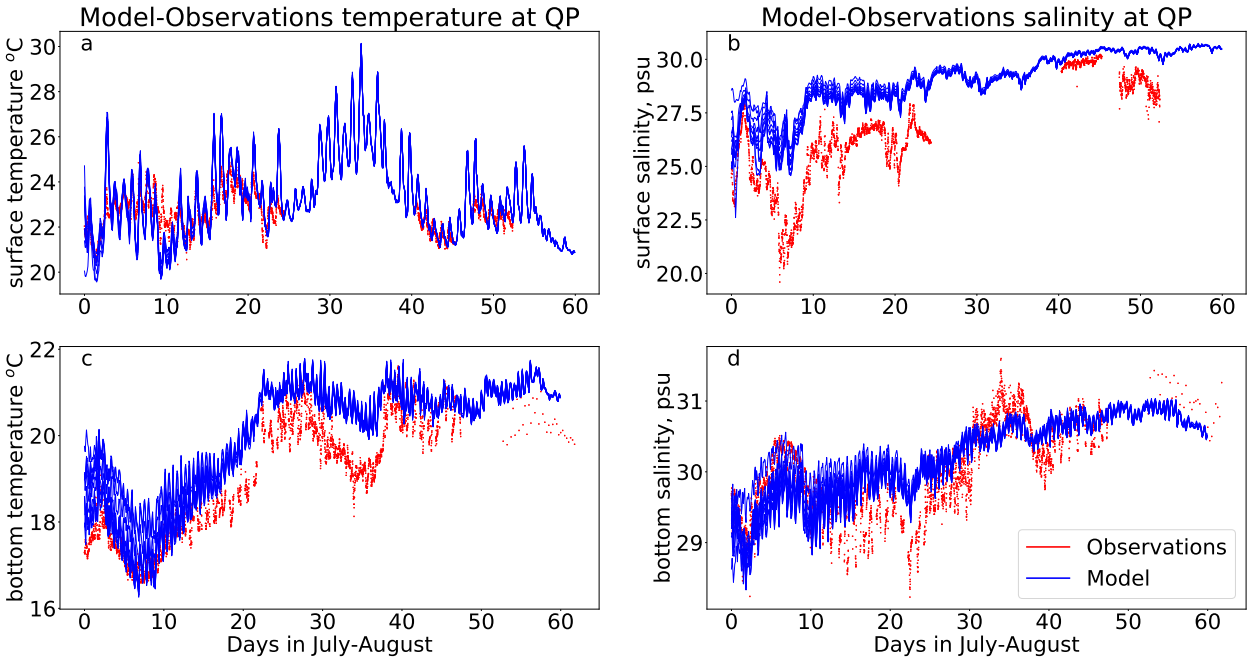

Figure A.5: Comparison of model with observations collected at Quonset Point (QP).

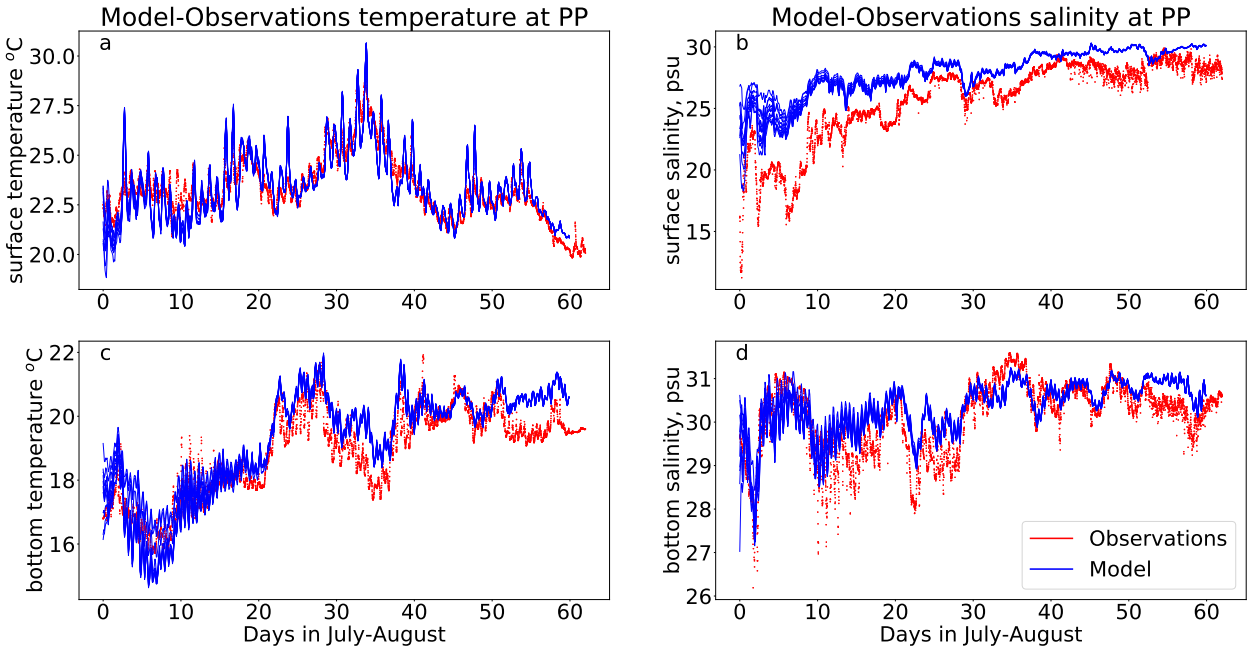

Figure A.6: Comparison of model with observations collected at Poppasquash Point (PP).

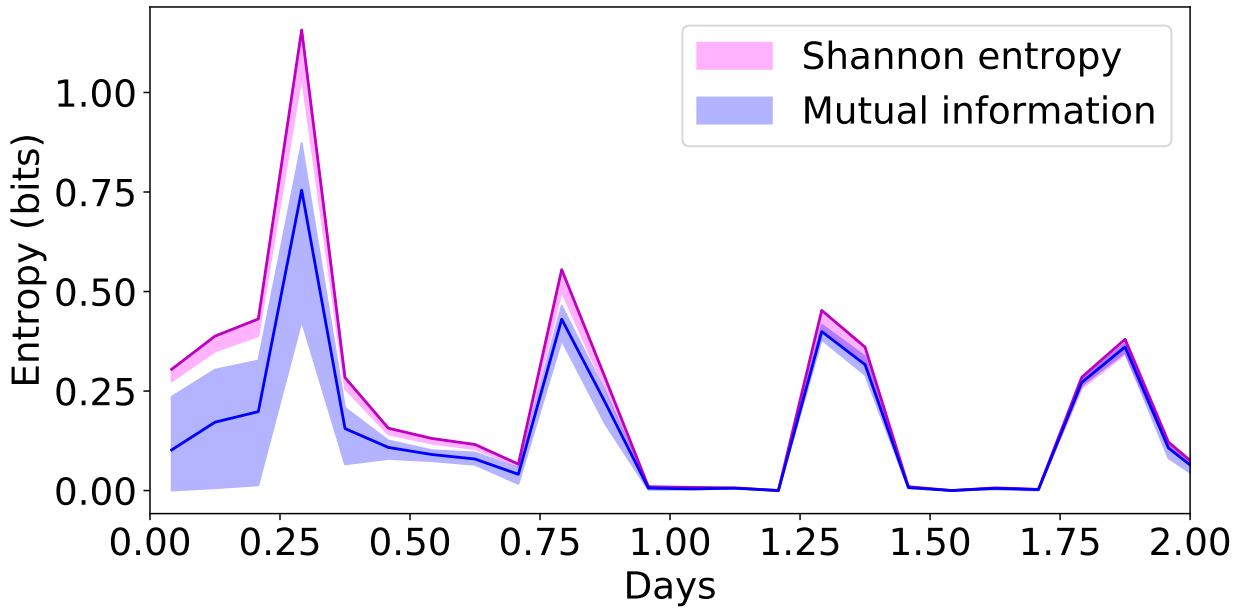

Figure A.7: Mutual information between members of climatology ensemble compared with Shannon entropy of the mean of ensemble of zone 1 for the months of July-August.

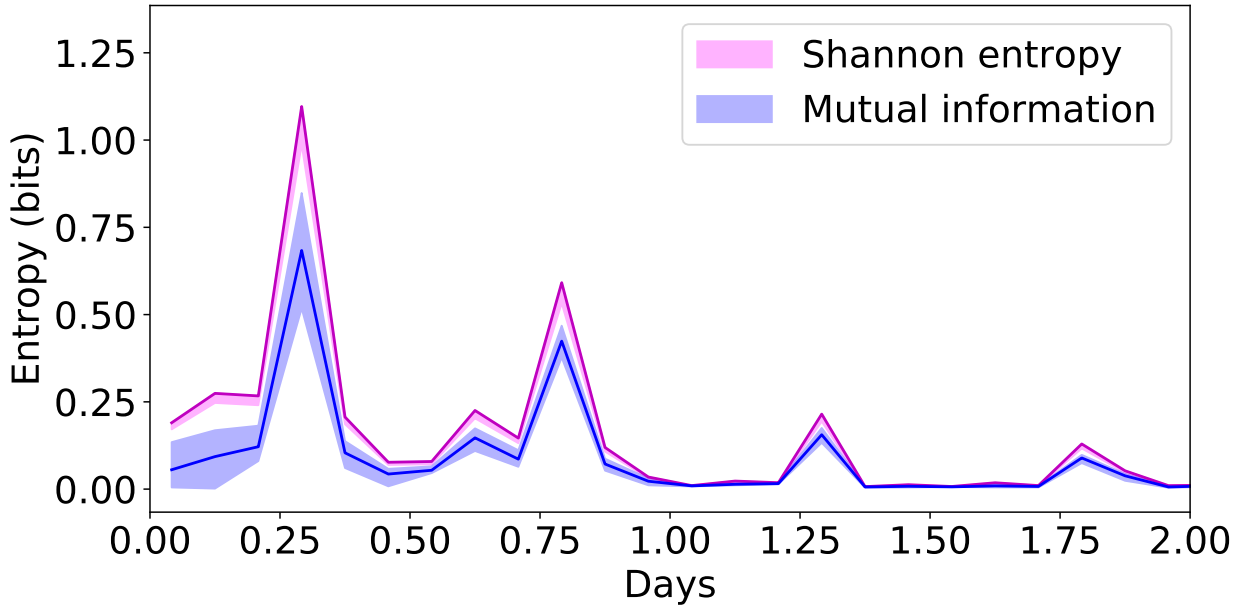

Figure A.8: Mutual information between members of climatology ensemble compared with Shannon entropy of the mean of ensemble of zone 2 for the months of July-August.

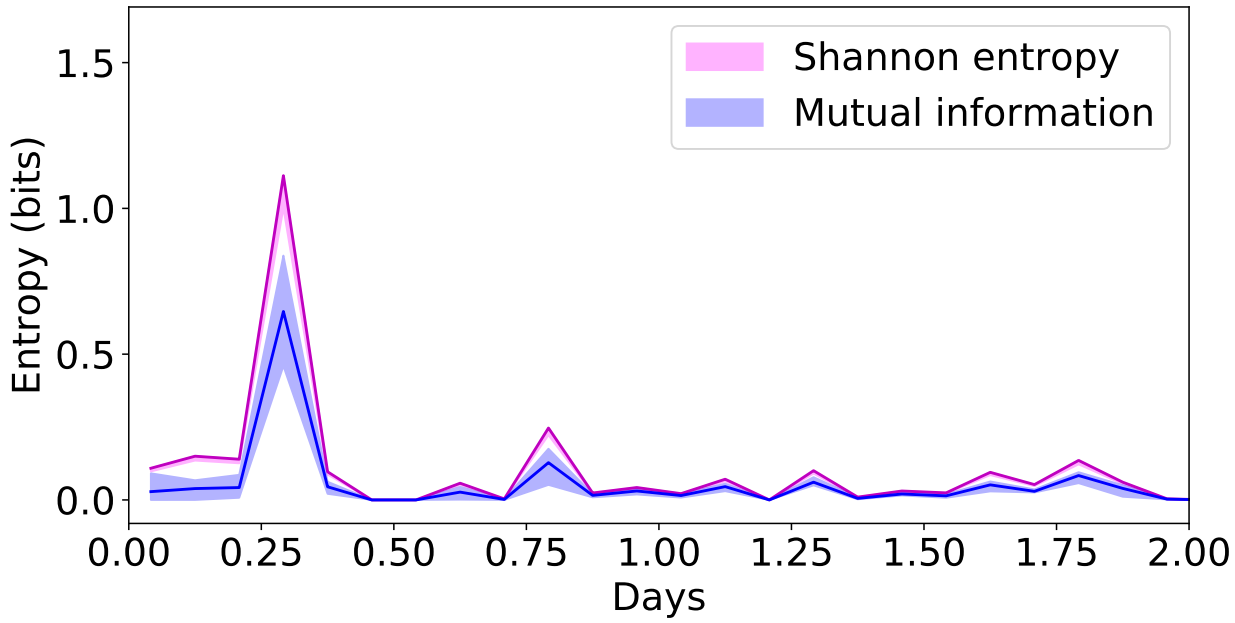

Figure A.9: Mutual information between members of climatology ensemble compared with Shannon entropy of the mean of ensemble of zone 3 for the months of July-August.

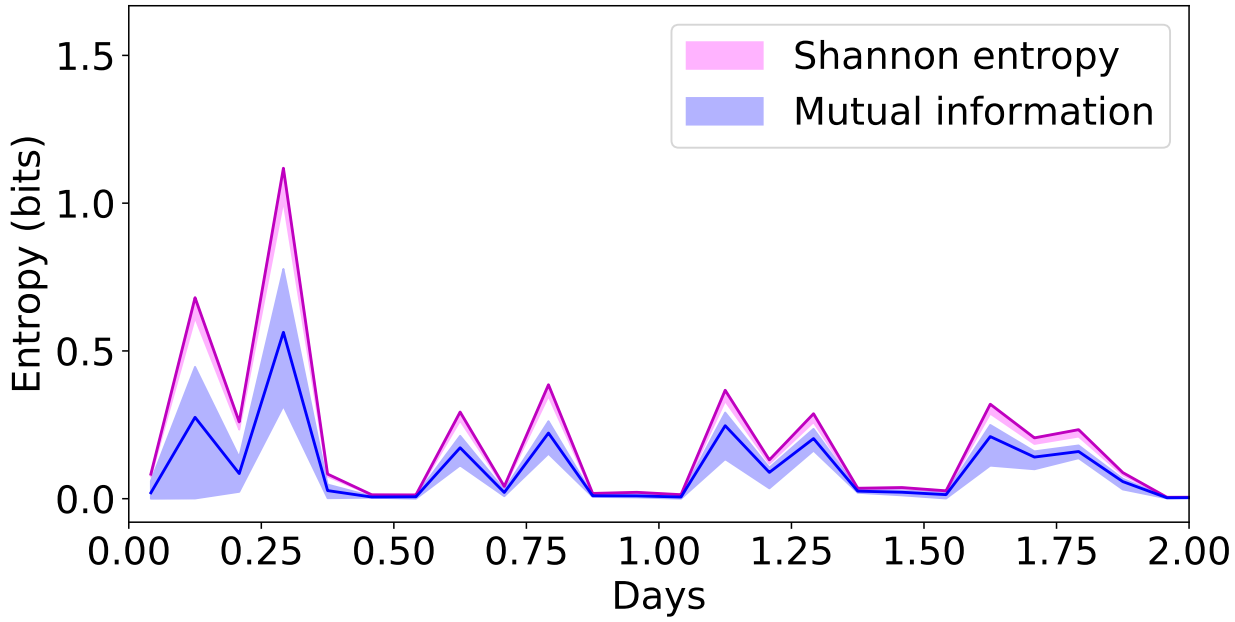

Figure A.10: Mutual information between members of climatology ensemble compared with Shannon entropy of the mean of ensemble of zone 4 for the months of July-August.

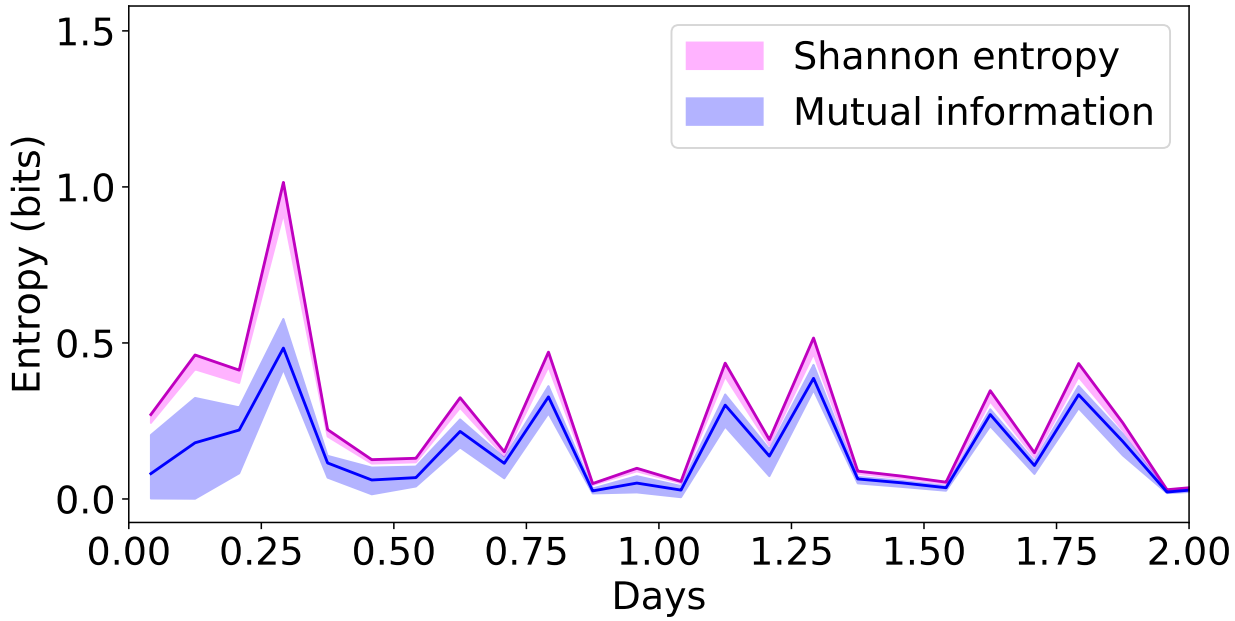

Figure A.11: Mutual information between members of climatology ensemble compared with Shannon entropy of the mean of ensemble of zone 5 for the months of July-August.

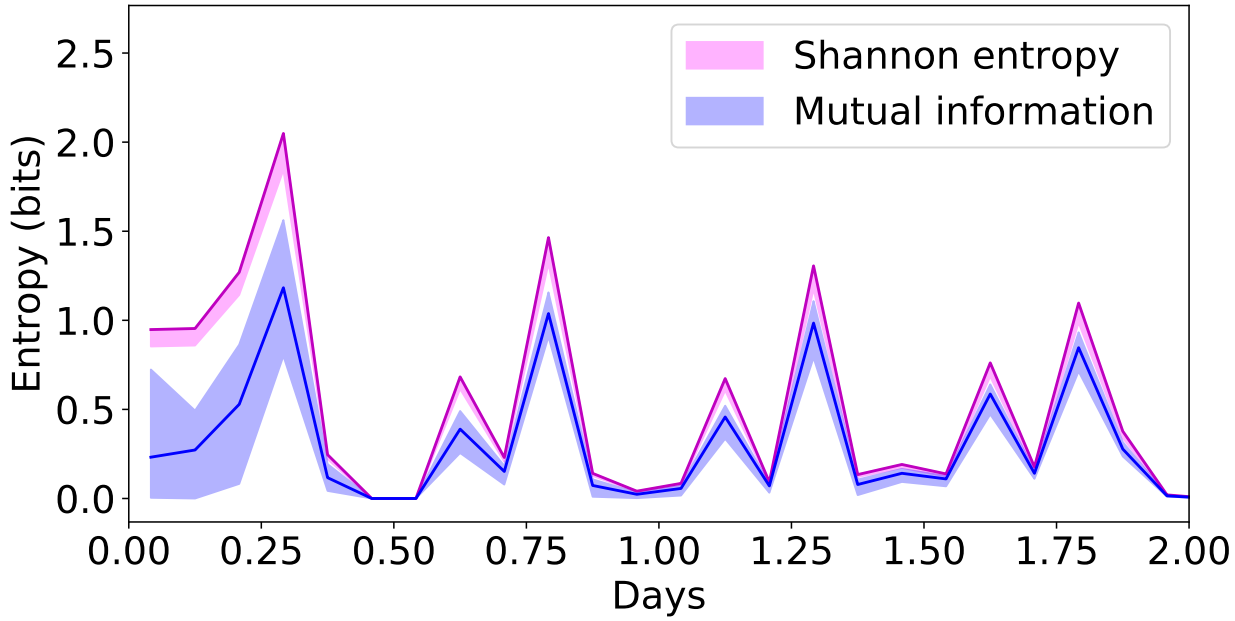

Figure A.12: Figure shows predictability of kinetic energy. Mutual information between members of climatology ensemble compared with Shannon entropy of the mean of ensemble of zone 7 for the months of July-August.

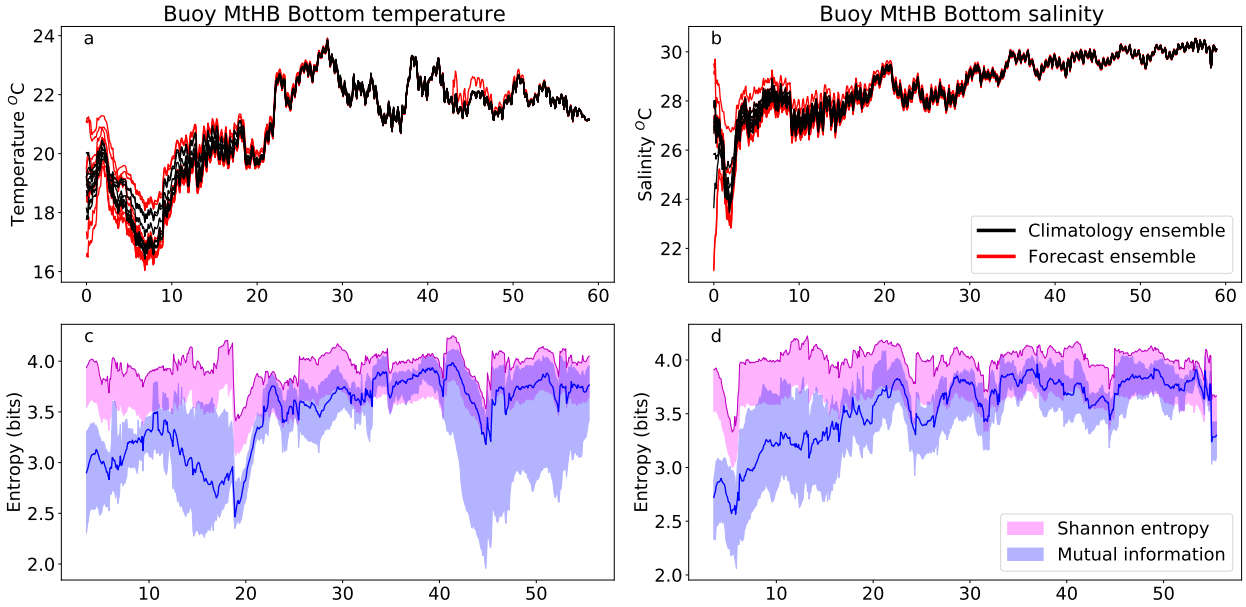

Figure A.13: Bottom temperature predictability at grid point closest to MtHB buoy

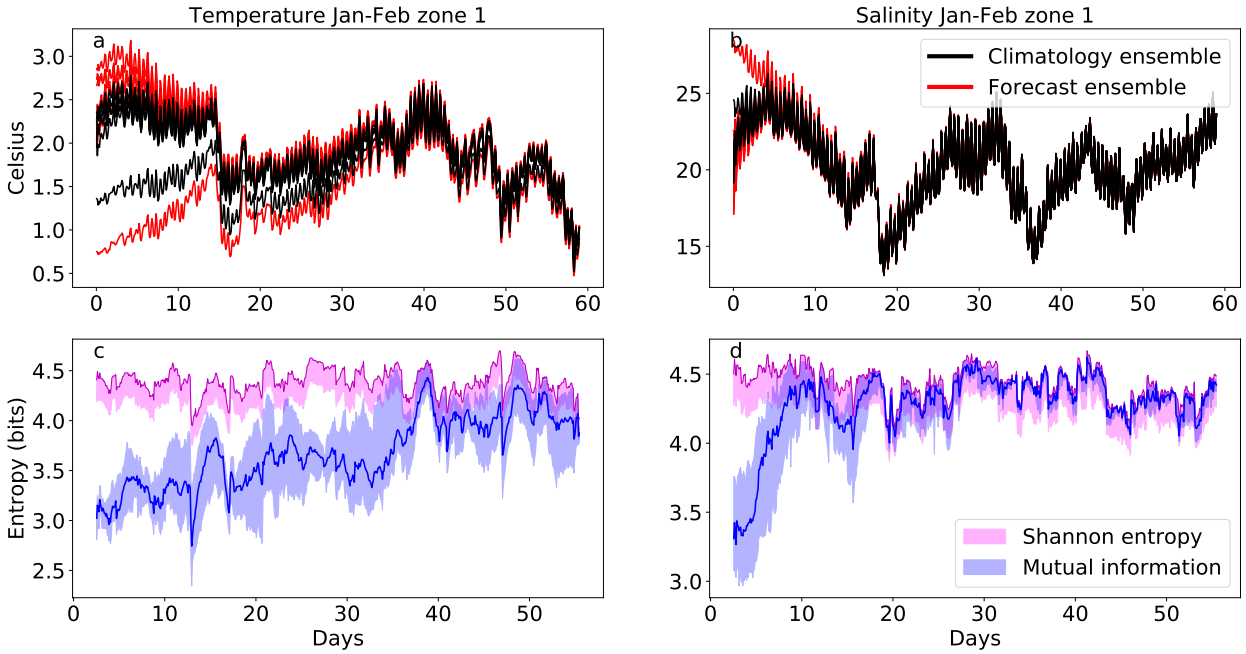

Figure A.14: Results of zone 1 for January-February. Top figures shows temperature and salinity ensembles. Bottom figures show information entropy metrics applied between forecast and climatology ensembles.

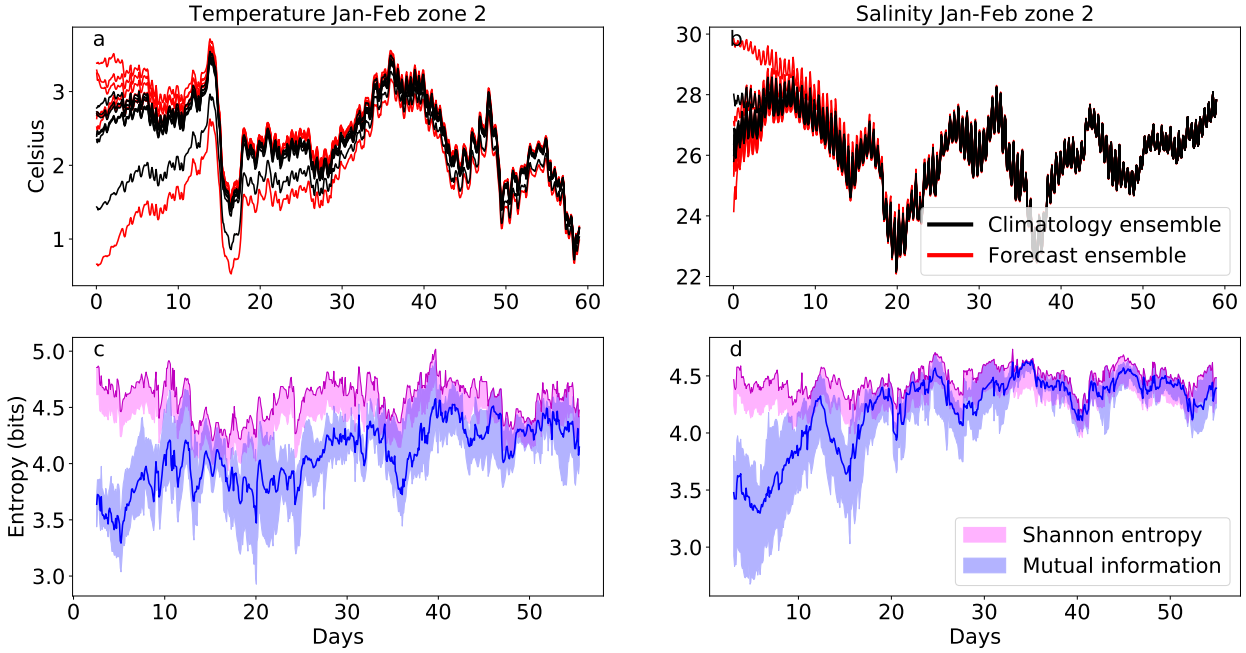

Figure A.15: Results of zone 2 for January-February. Top figures shows temperature and salinity ensembles. Bottom figures show information entropy metrics applied between forecast and climatology ensembles.

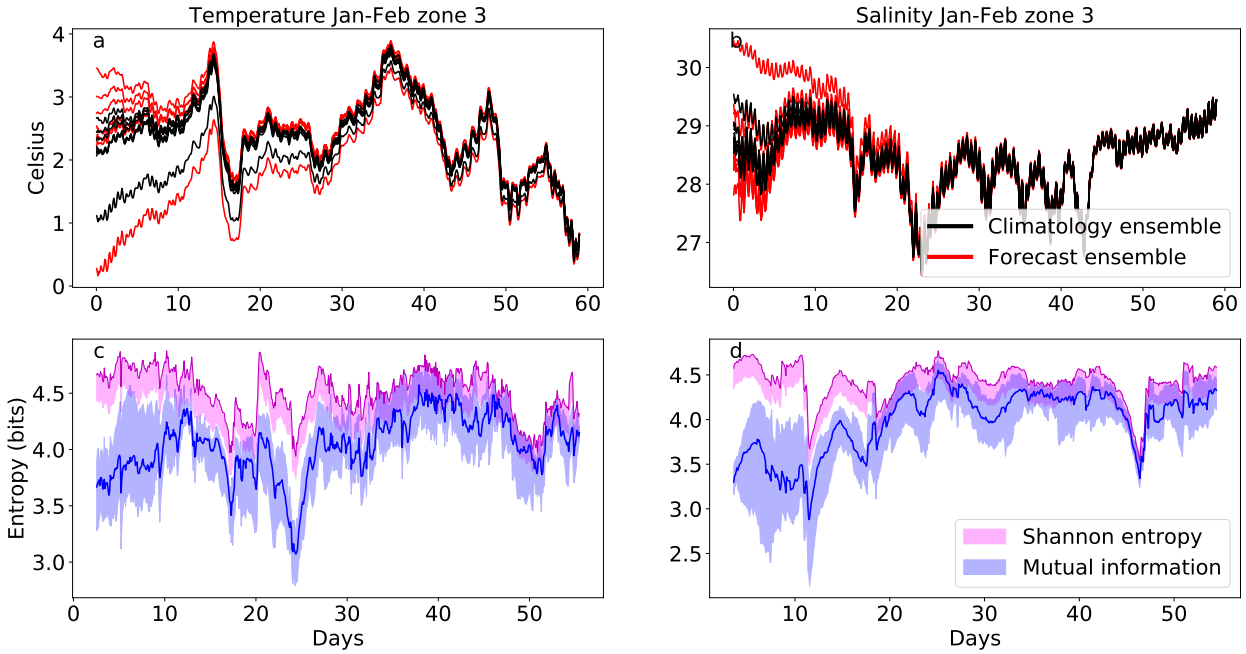

Figure A.16: Results of zone 3 for January-February. Top figures shows temperature and salinity ensembles. Bottom figures show information entropy metrics applied between forecast and climatology ensembles.

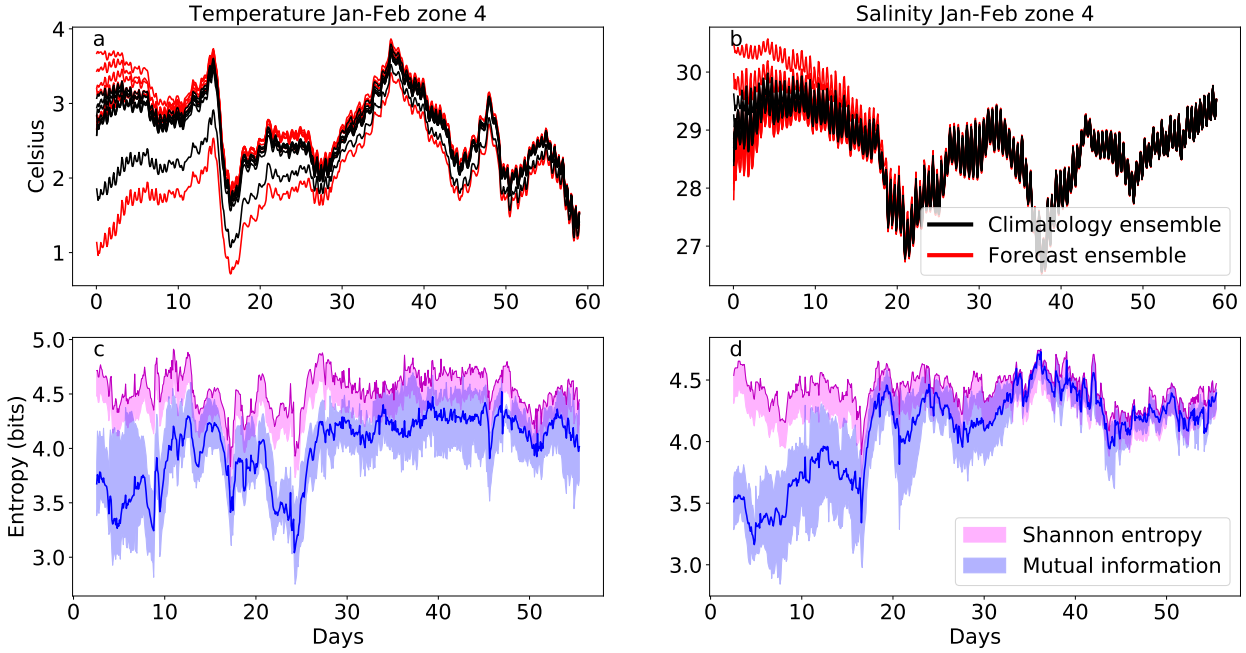

Figure A.17: Results of zone 4 for January-February. Top figures shows temperature and salinity ensembles. Bottom figures show information entropy metrics applied between forecast and climatology ensembles.

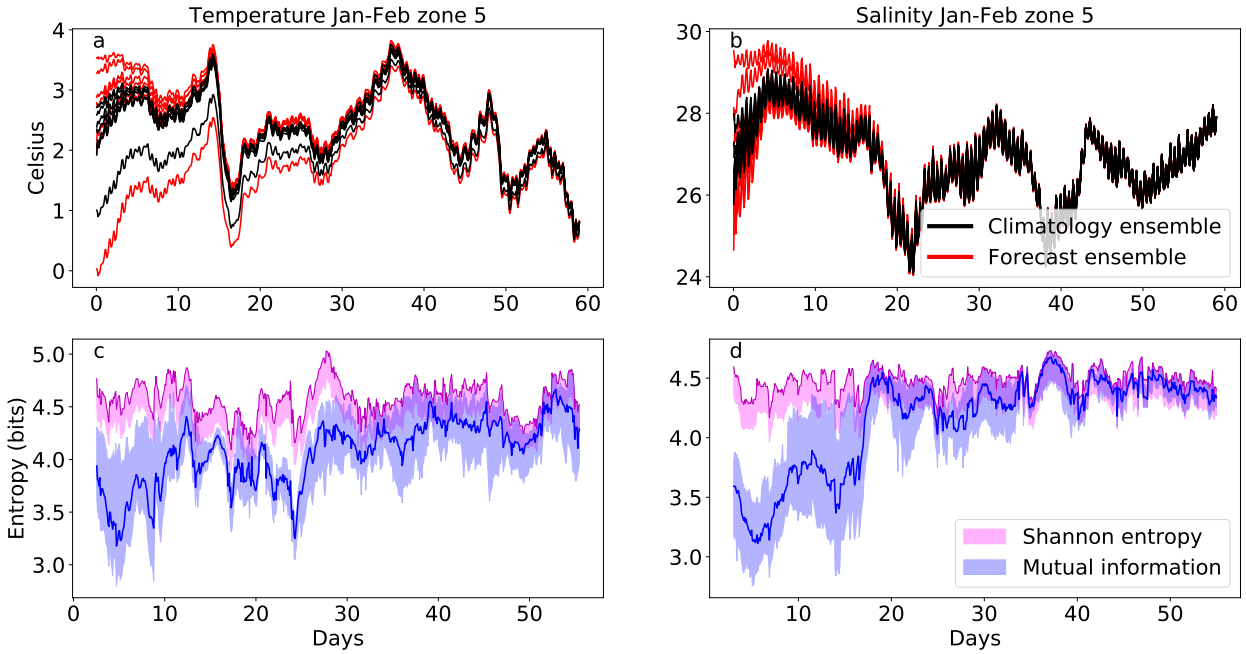

Figure A.18: Results of zone 5 for January-February. Top figures shows temperature and salinity ensembles. Bottom figures show information entropy metrics applied between forecast and climatology ensembles.

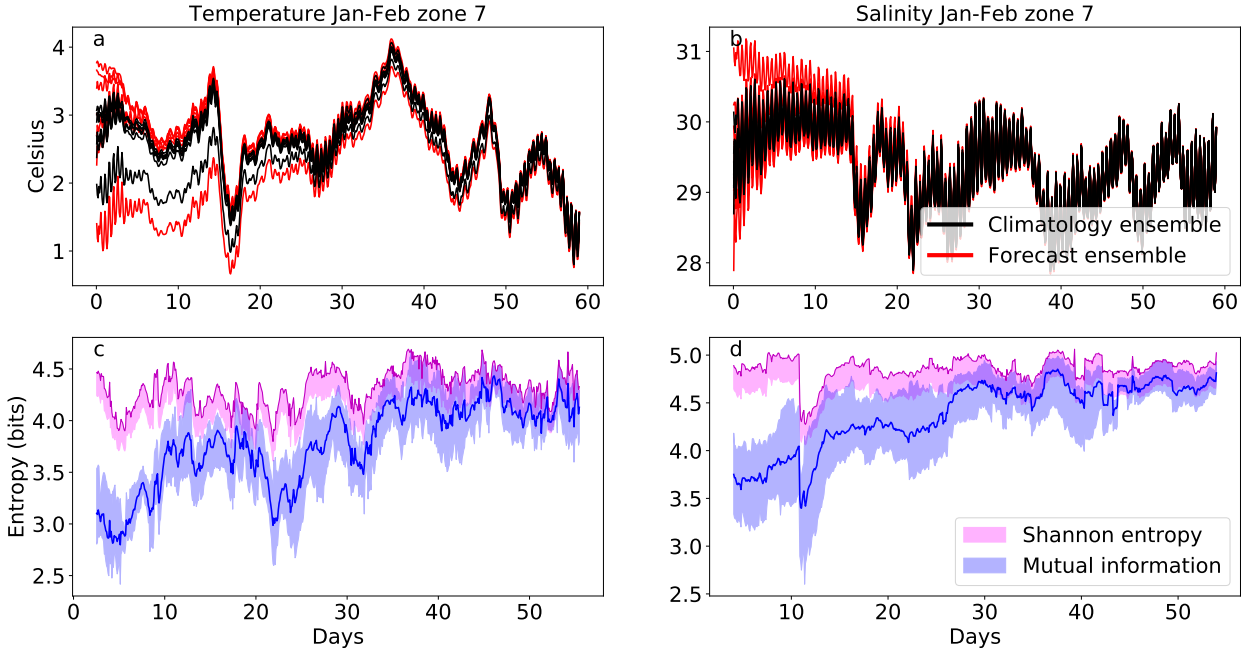

Figure A.19: Results of zone 7 for January-February. Top figures shows temperature and salinity ensembles. Bottom figures show information entropy metrics applied between forecast and climatology ensembles.

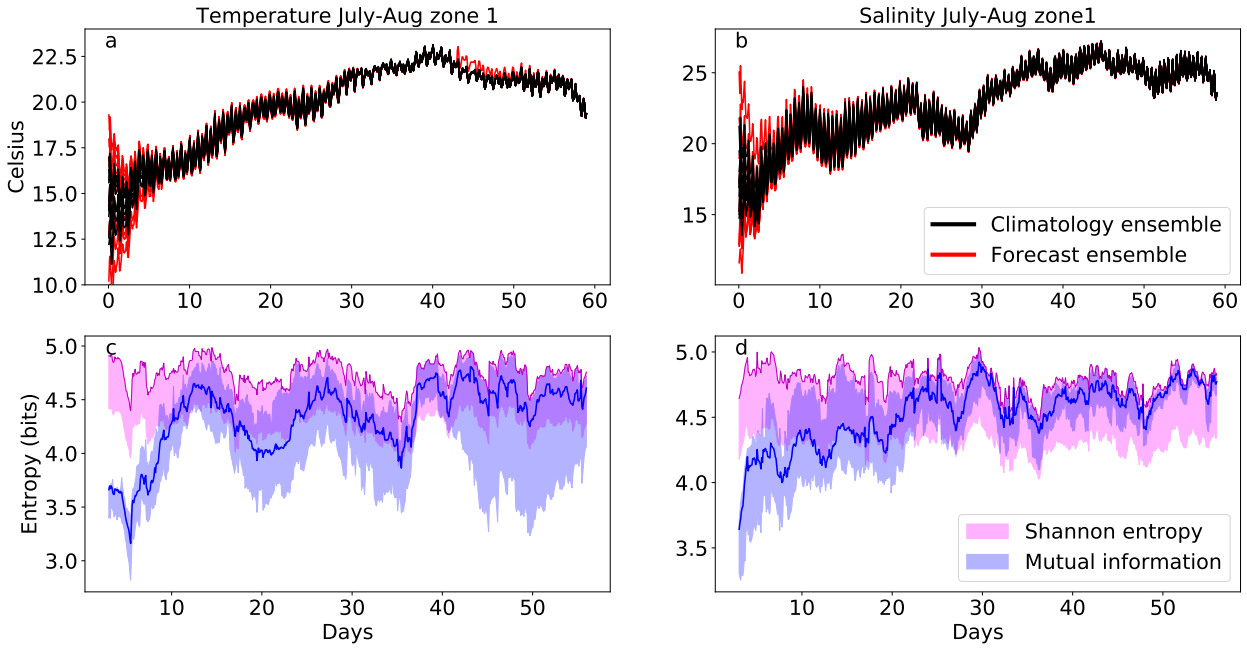

Figure A.20: Results of zone 1 for July - August. Top figures shows temperature and salinity ensembles. Bottom figures show information entropy metrics applied between forecast and climatology ensembles.

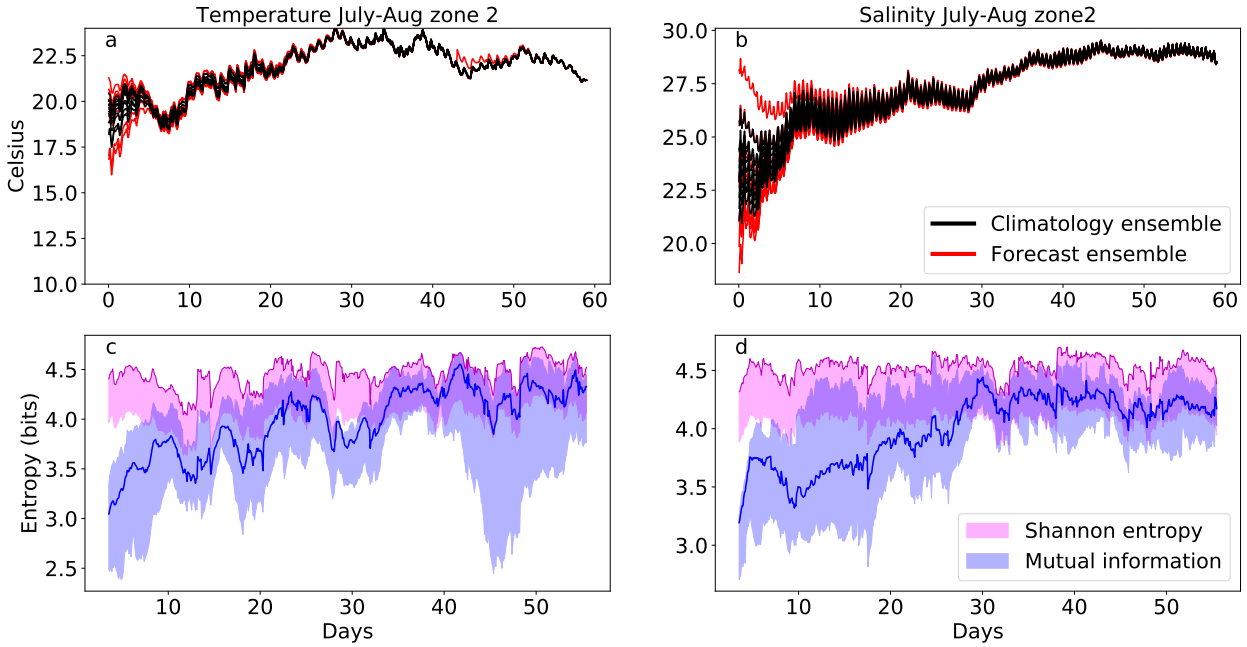

Figure A.21: Results of zone 2 for July - August. Top figures shows temperature and salinity ensembles. Bottom figures show information entropy metrics applied between forecast and climatology ensembles.

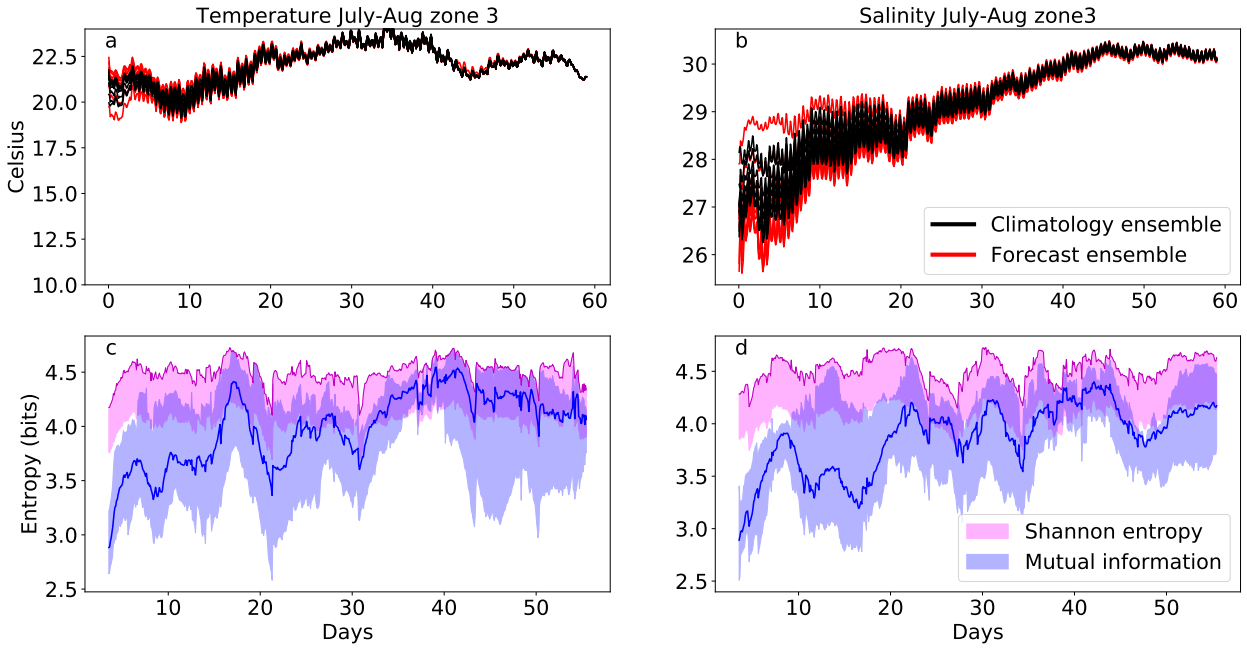

Figure A.22: Results of zone 3 for July - August. Top figures shows temperature and salinity ensembles. Bottom figures show information entropy metrics applied between forecast and climatology ensembles.

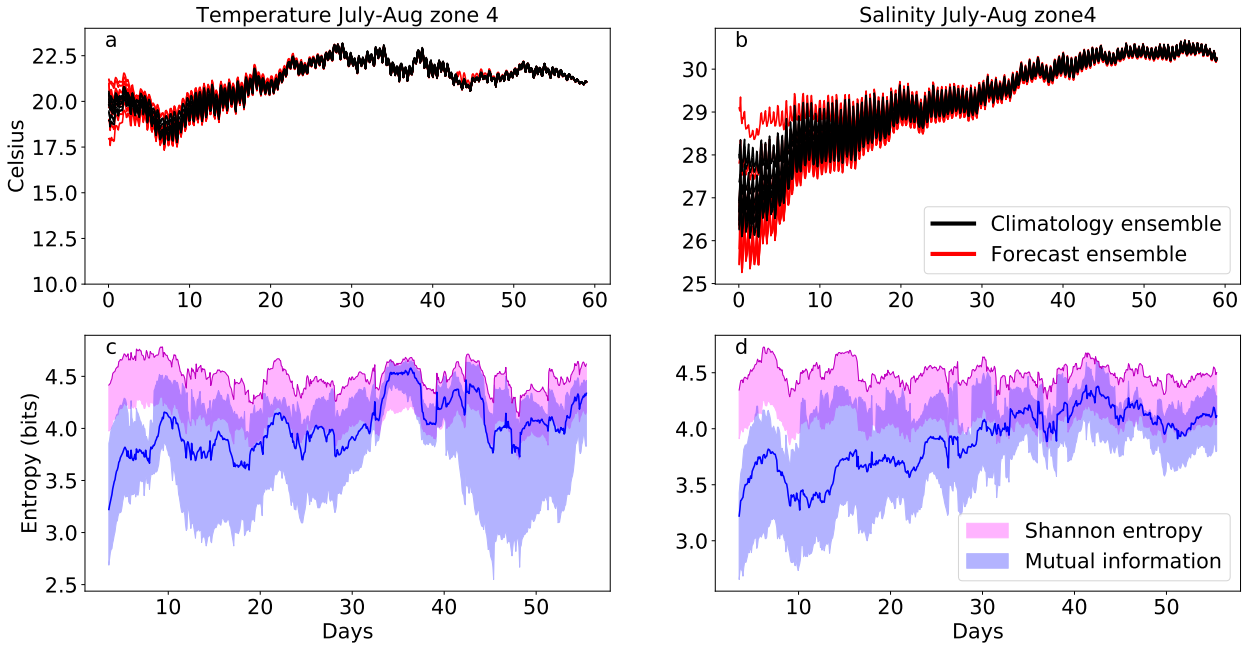

Figure A.23: Results of zone 4 for July - August. Top figures shows temperature and salinity ensembles. Bottom figures show information entropy metrics applied between forecast and climatology ensembles.

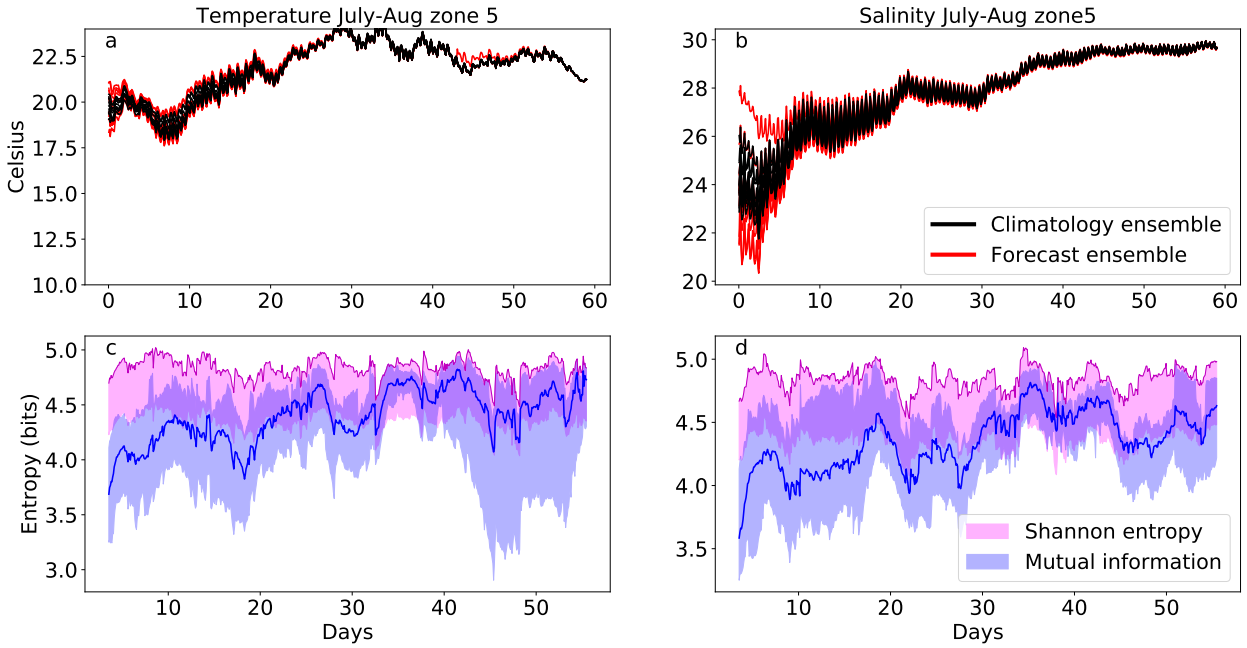

Figure A.24: Results of zone 5 for July - August. Top figures shows temperature and salinity ensembles. Bottom figures show information entropy metrics applied between forecast and climatology ensembles.

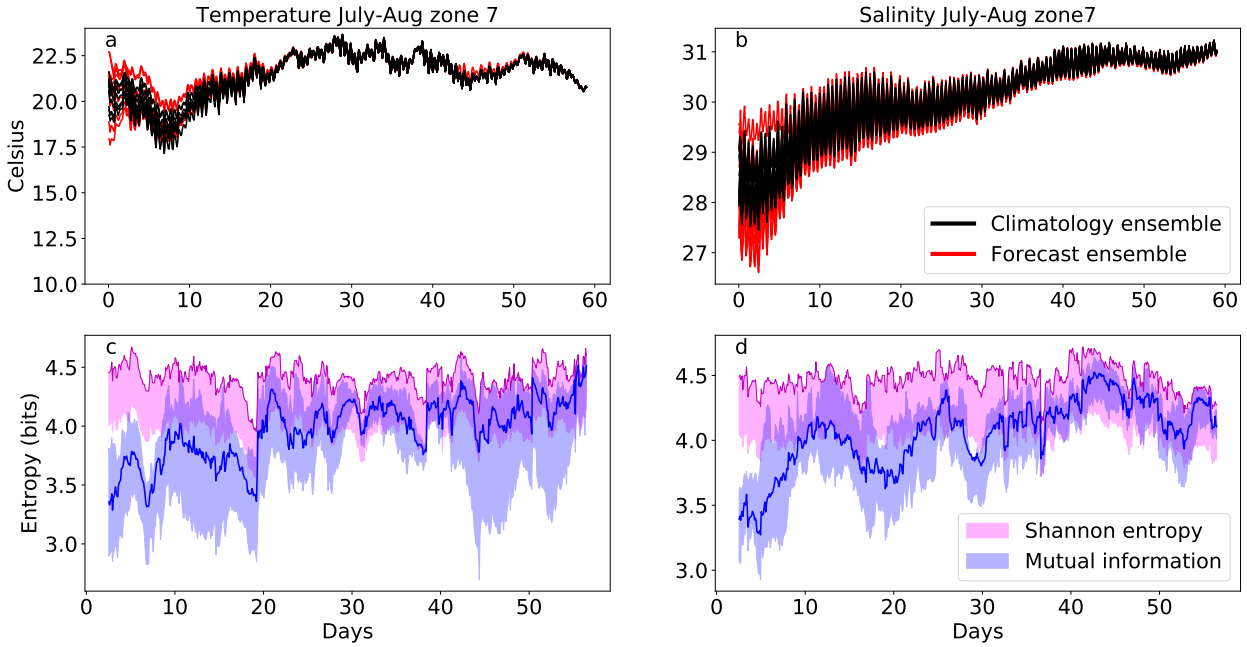

Figure A.25: Results of zone 7 for July - August. Top figures shows temperature and salinity ensembles. Bottom figures show information entropy metrics applied between forecast and climatology ensembles.

Appendix B

Fluxes in Narragansett Bay

Figure B.1 shows the fluxes going in and out of the bay as described in 2.6. X-axis has flow rate and y-axis is the distance from the North of the estuary. These fluxes have been calculated using Equation 2.6. The fluxes seem to be following an unknown scaling principle and has been observed in literature (see MacCready, 2011).

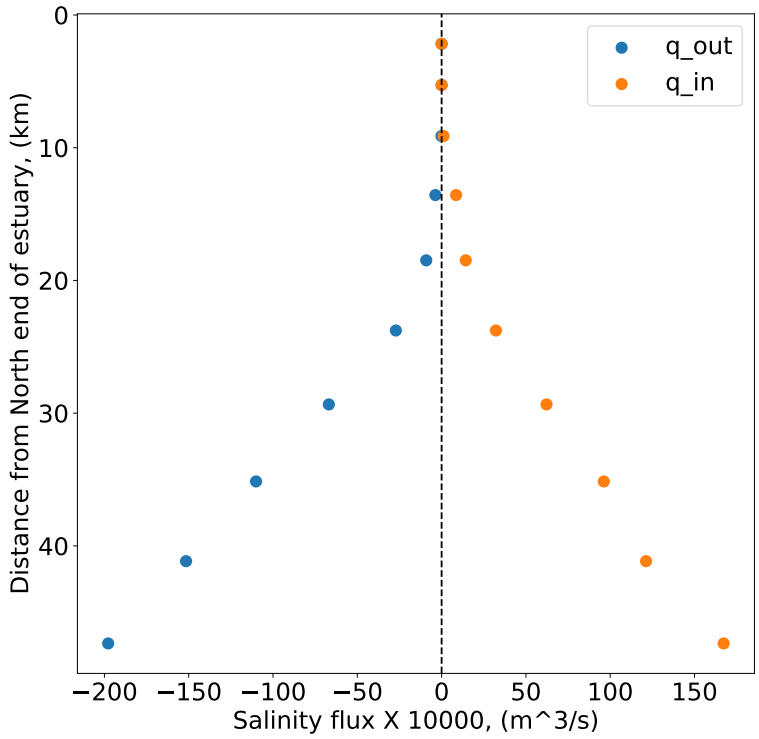

Figure B.1: Fluxes in Narragansett Bay calculated using ROMS-OSOM

Bibliography

Bachman, S., B. Fox-Kemper, J. Taylor, and L. Thomas (2017). Parameterization of frontal symmetric instabilities. i: Theory for resolved fronts. *Ocean Modelling 109*, 72–95.

Beardsley, R. C. and C. Chen (2014). Northeast Coastal Ocean Forecast System (NECOFS): A multi-scale global-regional-estuarine FVCOM model. In *2014 AGU Fall Meeting*. AGU.

Bergondo, D. (2004). *Examining the processes controlling water column variability in Narragansett Bay: Time series data and numerical modeling*. Ph. D. thesis, University of Rhode Island.

Bergondo, D. and C. Kincaid (2007). Development and calibration of a model for tracking dispersion of waters from narragansett bay commission facilities within the providence river and narragansett bay. Technical report, Narragansett Bay Commission.

Brissaud, J. B. (2005). The meanings of entropy. *Entropy 7*(1), 68–96.

Carcassi, G., C. A. Aidala, and J. Barbour (2019). Variability as a better characterization of shannon entropy. *arXiv preprint arXiv:1912.02012*.

Chapman, D. C. (1985). Numerical treatment of cross-shelf open boundaries in a barotropic coastal ocean model. *Journal of Physical oceanography 15*(8), 1060–1075.

Codiga, D. L., H. E. Stoffel, C. F. Deacutis, S. Kiernan, and C. A. Oviatt (2009). Narragansett bay hypoxic event characteristics based on fixed-site monitoring network time series: intermittency, geographic distribution, spatial synchronicity, and interannual variability. *Estuaries and coasts 32*(4), 621–641.

Correa, C. D. and P. Lindstrom (2013). The mutual information diagram for uncertainty visualization. *International Journal for Uncertainty Quantification 3*(3).

Cover, T. M. (1999). *Elements of information theory*. John Wiley & Sons.

Cover, T. M. and J. A. Thomas (2012). *Elements of information theory*. John Wiley & Sons.

Cushman-Roisin, B. and J.-M. Beckers (2011). *Introduction to geophysical fluid dynamics: physical and numerical aspects*. Academic press.

DelSole, T. (2004). Predictability and information theory. part i: Measures of predictability. *Journal of the atmospheric sciences 61*(20), 2425–2440.

DelSole, T. and J. Shukla (2010). Model fidelity versus skill in seasonal forecasting. *Journal of Climate 23*(18), 4794–4806.

DelSole, T. and M. K. Tippett (2007). Predictability: Recent insights from information theory. *Reviews of Geophysics 45*(4).

DelSole, T. and M. K. Tippett (2018). Predictability in a changing climate. *Climate Dynamics 51*(1), 531–545.

Demirtas, H. (2014). Generating bivariate uniform data with a full range of correlations and

connections to bivariate binary data. *Communications in Statistics-Theory and Methods 43*(17), 3574–3579.

Deser, C., F. Lehner, K. Rodgers, T. Ault, T. Delworth, P. DiNezio, A. Fiore, C. Frankignoul, J. Fyfe, D. Horton, J. E. Kay, R. Knutti, N. S. Lovenduski, J. Marotzke, K. A. McKinnon, S. Minobe, J. A. S. J. Randerson, I. R. Simpson, and M. Ting (2020). Insights from earth system model initial-condition large ensembles and future prospects. *Nature Climate Change*, 1–10.

Dong, J., B. Fox-Kemper, J. Zhu, and C. Dong (2021). Application of symmetric instability parameterization in the coastal and regional ocean community model (croco). *Journal of Advances in Modeling Earth Systems 13*(3). e2020MS002302 2020MS002302.

Engle, V. D., J. C. Kurtz, L. M. Smith, C. Chancy, and P. Bourgeois (2007). A classification of us estuaries based on physical and hydrologic attributes. *Environmental Monitoring and Assessment 129*(1-3), 397–412.

Ezer, T., H. Arango, and A. F. Shchepetkin (2002). Developments in terrain-following ocean models: intercomparisons of numerical aspects. *Ocean Modelling 4*(3-4), 249–267.

Fairall, C. W., E. F. Bradley, J. Hare, A. A. Grachev, and J. B. Edson (2003). Bulk parameterization of air–sea fluxes: Updates and verification for the coare algorithm. *Journal of climate 16*(4), 571–591.

Fano, T. (1961). *Transmission of Information, A Statistical Theory of Communications*. The M.I.T. Press, John Wiley & Sons.

Flather, R. A. (1976). *Practical aspects of the use of numerical models for surge prediction*. Institute of Oceanographic Sciences, Bidston Observatory.

Frankcombe, L. M., M. H. England, M. E. Mann, and B. A. Steinman (2015). Separating internal variability from the externally forced climate response. *Journal of Climate 28*(20), 8184–8202.

Franzke, C. L., S. Barbosa, R. Blender, H.-B. Fredriksen, T. Laepple, F. Lambert, T. Nilsen, K. Rypdal, M. Rypdal, M. G. Scotto, et al. (2020). The structure of climate variability across scales. *Reviews of Geophysics 58*(2), e2019RG000657.

Gomez, B. G. (2020). *Intrinsic ocean variability modulated by the atmosphere in the Gulf of Mexico: an ensemble modelling study*. Ph. D. thesis, Université Grenoble Alpes [2020-....].

Hacine-Gharbi, A., P. Ravier, R. Harba, and T. Mohamadi (2012). Low bias histogram-based estimation of mutual information for feature selection. *Pattern recognition letters 33*(10), 1302–1308.

Haidvogel, D. B., H. G. Arango, K. Hedstrom, A. Beckmann, P. Malanotte-Rizzoli, and A. F. Shchepetkin (2000). Model evaluation experiments in the north atlantic basin: simulations in nonlinear terrain-following coordinates. *Dynamics of atmospheres and oceans 32*(3-4), 239–281.

Hartley, R. V. (1928). Transmission of information 1. *Bell System technical journal 7*(3), 535–563.

Haven, K., A. Majda, and R. Abramov (2005). Quantifying predictability through information theory: small sample estimation in a non-gaussian framework. *Journal of Computational Physics 206*(1), 334–362.

Hawkins, E. and R. Sutton (2012). Time of emergence of climate signals. *Geophysical Research Letters 39*(1).

Hayward, S., M. R. Hashemi, M. Torres, A. Grilli, S. Grilli, J. King, C. Baxter, and M. Spaulding

(2018). Numerical simulation of coastal erosion and its mitigation by living shoreline methods: A case study in southern rhode island. *Shore & Beach 86*(4), 13.

Holton, J. R. *An introduction to dynamic meteorology* (4 ed.), Volume 88.

Hoskins, B. J. (1974). The role of potential vorticity in symmetric stability and instability. *Quarterly Journal of the Royal Meteorological Society 100*(425), 480–482.

Jaynes, E. T. (1962). Information theory and statistical mechanics.

Jin, Y., X. Rong, and Z. Liu (2018). Potential predictability and forecast skill in ensemble climate forecast: a skill-persistence rule. *Climate dynamics 51*(7-8), 2725–2742.

Kalra, T. S., X. Li, J. C. Warner, W. R. Geyer, and H. Wu (2019). Comparison of physical to numerical mixing with different tracer advection schemes in estuarine environments. *Journal of Marine Science and Engineering 7*(10), 338.

Kleeman, R. (2002). Measuring dynamical prediction utility using relative entropy. *Journal of the atmospheric sciences 59*(13), 2057–2072.

Knudsen, M. (1900). Ein hydrographischer lehrsatz. *Ann. Hydrogr. Marit. Meteorol. 28*, 316–320.

Knuth, K. H. (2019). Optimal data-based binning for histograms and histogram-based probability density models. *Digital Signal Processing 95*, 102581.

Kowal, R. R. (1971). 296. note: Disadvantages of the generalized variance as a measure of variability. *Biometrics 27*(1), 213–216.

Kowalski, A. M., M. T. Martin, A. Plastino, and G. Judge (2012). On extracting probability distribution information from time series. *Entropy 14*(10), 1829–1841.

Kumar, A., P. Peng, and M. Chen (2014). Is there a relationship between potential and actual skill? *Monthly Weather Review 142*(6), 2220–2227.

Kumar, P. and H. V. Gupta (2020). Debates—does information theory provide a new paradigm for earth science? *Water Resources Research 56*(2), e2019WR026398. e2019WR026398 2019WR026398.

Kundu, P. K., I. M. Cohen, and D. R. Dowling (2016). Chapter 12 - turbulence. In P. K. Kundu, I. M. Cohen, and D. R. Dowling (Eds.), *Fluid Mechanics (Sixth Edition)* (Sixth Edition ed.)., pp. 603–697. Boston: Academic Press.

Large, W. G., J. C. McWilliams, and S. C. Doney (1994). Oceanic vertical mixing: A review and a model with a nonlocal boundary layer parameterization. *Reviews of geophysics 32*(4), 363–403.

Lellouche, J.-M., E. Greiner, O. Le Galloudec, C. Regnier, M. Benkiran, C.-E. Testut, R. Bourdalle-Badie, M. Drevillon, G. Garric, and Y. Drillet (2018). Mercator ocean global high-resolution monitoring and forecasting system. *New Frontiers in Operational Oceanography*, 563–592.

Lemagie, E. P. and J. A. Lerczak (2015). A comparison of bulk estuarine turnover timescales to particle tracking timescales using a model of the yaquina bay estuary. *Estuaries and coasts 38*(5), 1797–1814.

Lemarié, F., L. Debreu, A. Shchepetkin, and J. C. Mcwilliams (2012). On the stability and accuracy of the harmonic and biharmonic isoneutral mixing operators in ocean models. *Ocean Modelling 52*, 9–35.

Lemarié, F., J. Kurian, A. F. Shchepetkin, M. J. Molemaker, F. Colas, and J. C. McWilliams

(2012). Are there inescapable issues prohibiting the use of terrain-following coordinates in climate models? *Ocean Modelling 42*, 57–79.

Leroux, S., T. Penduff, L. Bessières, J.-M. Molines, J.-M. Brankart, G. Sérazin, B. Barnier, and L. Terray (2018). Intrinsic and atmospherically forced variability of the amoc: insights from a large-ensemble ocean hindcast. *Journal of Climate 31*(3), 1183–1203.

Leung, L.-Y. and G. R. North (1990). Information theory and climate prediction. *Journal of Climate 3*(1), 5–14.

Li, Q., B. G. Reichl, B. Fox-Kemper, A. J. Adcroft, S. E. Belcher, G. Danabasoglu, A. L. M. Grant, S. M. Griffies, R. Hallberg, T. Hara, R. R. Harcourt, T. Kukulka, W. G. Large, J. C. McWilliams, B. Pearson, P. P. Sullivan, L. Van Roekel, P. Wang, and Z. Zheng (2019). Comparing ocean surface boundary vertical mixing schemes including langmuir turbulence. *Journal of Advances in Modeling Earth Systems 11*(11), 3545–3592.

Liang, X. S. (2013). The liang-kleeman information flow: Theory and applications. *Entropy 15*(1), 327–360.

Liang, X. S. (2014). Entropy evolution and uncertainty estimation with dynamical systems. *Entropy 16*(7), 3605–3634.

Liang, Y.-c., Y.-O. Kwon, C. Frankignoul, G. Danabasoglu, S. Yeager, A. Cherchi, Y. Gao, G. Gastineau, R. Ghosh, D. Matei, et al. (2020). Quantification of the arctic sea ice-driven atmospheric circulation variability in coordinated large ensemble simulations. *Geophysical Research Letters 47*(1), e2019GL085397.

Liu, Q., L. M. Rothstein, Y. Luo, D. S. Ullman, and D. L. Codiga (2016). Dynamics of the periphery current in rhode island sound. *Ocean Modelling 105*, 13–24.

Llovel, W., T. Penduff, B. Meyssignac, J.-m. Molines, L. Terray, L. Bessières, and B. Barnier (2018). Contributions of atmospheric forcing and chaotic ocean variability to regional sea level trends over 1993–2015. *Geophysical Research Letters 45*(24), 13–405.

Lorenz, E. N. (1963). Deterministic nonperiodic flow. *Journal of atmospheric sciences 20*(2), 130–141.

MacCready, P. (2011). Calculating estuarine exchange flow using isohaline coordinates. *Journal of Physical Oceanography 41*(6), 1116–1124.

Majda, A., R. Kleeman, D. Cai, et al. (2002). A mathematical framework for quantifying predictability through relative entropy. *Methods and Applications of Analysis 9*(3), 425–444.

Majda, A. J. and B. Gershgorin (2010). Quantifying uncertainty in climate change science through empirical information theory. *Proceedings of the National Academy of Sciences 107*(34), 14958–14963.

Marchesiello, P., L. Debreu, and X. Couvelard (2009). Spurious diapycnal mixing in terrain-following coordinate models: The problem and a solution. *Ocean Modelling 26*(3-4), 156–169.

Marchesiello, P., J. C. McWilliams, and A. Shchepetkin (2001). Open boundary conditions for long-term integration of regional oceanic models. *Ocean modelling 3*(1-2), 1–20.

McManus, M. C., D. S. Ullman, S. D. Rutherford, and C. Kincaid (2020). Northern quahog (mer-

cenaria mercenaria) larval transport and settlement modeled for a temperate estuary. *Limnology and Oceanography 65*(2), 289–303.

Mel, R. and P. Lionello (2014). Storm surge ensemble prediction for the city of venice. *Weather and forecasting 29*(4), 1044–1057.

Milinski, S., N. Maher, and D. Olonscheck (2019). How large does a large ensemble need to be. *Earth Syst. Dynam. Discuss., 2019, 1–19, doi: 10.5194/esd-2019 70*.

Monsen, N. E., J. E. Cloern, L. V. Lucas, and S. G. Monismith (2002). A comment on the use of flushing time, residence time, and age as transport time scales. *Limnology and oceanography 47*(5), 1545–1553.

Moore, A. M., H. G. Arango, G. Broquet, B. S. Powell, A. T. Weaver, and J. Zavala-Garay (2011). The regional ocean modeling system (roms) 4-dimensional variational data assimilation systems: Part i–system overview and formulation. *Progress in Oceanography 91*(1), 34–49.

Mukai, A. Y., J. J. Westerink, R. A. Luettich Jr, and D. Mark (2002). Eastcoast 2001, a tidal constituent database for western north atlantic, gulf of mexico, and caribbean sea. Technical report, Engineer Research and Development Center Coast and Hydraulics Lab, Vicksburg, MS.

Mustard, J., M. Carney, and A. Sen (1999). The use of satellite data to quantify thermal effluent impacts. *Estuarine, Coastal and Shelf Science 49*(4), 509–524.

Ménesguen, C., S. L. Gentil, P. Marchesiello, and N. Ducousso (2018). Destabilization of an oceanic meddy-like vortex: Energy transfers and significance of numerical settings. *Journal of Physical Oceanography 48*(5), 1151 – 1168.

Nixon, S. W., B. A. Buckley, S. L. Granger, L. A. Harris, A. J. Oczkowski, R. W. Fulweiler, and L. W. Cole (2008). Nitrogen and phosphorus inputs to narragansett bay: past, present, and future. In *Science for ecosystem-based management*, pp. 101–175. Springer.

Papana, A. and D. Kugiumtzis (2008). Evaluation of mutual information estimators on nonlinear dynamic systems. *Nonlinear Phenomena in Complex Systems 11*(2), 225–232.

Perdigão, R. A., U. Ehret, K. H. Knuth, and J. Wang (2020). Debates: Does information theory provide a new paradigm for earth science? emerging concepts and pathways of information physics. *Water Resources Research 56*(2), e2019WR025270. e2019WR025270 2019WR025270.

Pilson, M. E. (1985). On the residence time of water in narragansett bay. *Estuaries 8*(1), 2–14.

Pinardi, N. and G. Coppini (2010). Operational oceanography in the mediterranean sea: the second stage of development. *Ocean Sci 6*, 263–267.

Raboudi, N. F., B. Ait-El-Fquih, C. Dawson, and I. Hoteit (2019). Combining hybrid and one-step-ahead smoothing for efficient short-range storm surge forecasting with an ensemble kalman filter. *Monthly Weather Review 147*(9), 3283–3300.

Rayson, M. D., E. S. Gross, R. D. Hetland, and O. B. Fringer (2016). Time scales in galveston bay: An unsteady estuary. *Journal of Geophysical Research: Oceans 121*(4), 2268–2285.

Rodgers, K. B., J. Lin, and T. L. Frölicher (2015). Emergence of multiple ocean ecosystem drivers in a large ensemble suite with an earth system model. *Biogeosciences 12*(11), 3301–3320.

Roulston, M. S. and L. A. Smith (2002). Evaluating probabilistic forecasts using information theory. *Monthly Weather Review 130*(6), 1653–1660.

Sane, A., B. Fox-Kemper, and D. Ullman (2021). Internal vs forced variability metrics for geophysical flows using information theory. *Earth and Space Science Open Archive*, 34.

Sane, A., B. Fox-Kemper, D. S. Ullman, C. Kincaid, and L. Rothstein. Consistent predictability of the ocean state ocean model (osom) using information theory and flushing timescales. *Journal of Geophysical Research: Oceans n/a*(n/a), e2020JC016875.

Schneider, T. and S. M. Griffies (1999). A conceptual framework for predictability studies. *Journal of climate 12*(10), 3133–3155.

Schurer, A. P., G. C. Hegerl, M. E. Mann, S. F. Tett, and S. J. Phipps (2013). Separating forced from chaotic climate variability over the past millennium. *Journal of Climate 26*(18), 6954–6973.

Sethna, J. et al. (2006). *Statistical mechanics: entropy, order parameters, and complexity*, Volume 14. Oxford University Press.

Shannon, C. E. (1948). A mathematical theory of communication. *Bell system technical journal 27*(3), 379–423.

Shchepetkin, A. F. and J. C. McWilliams (1998). Quasi-monotone advection schemes based on explicit locally adaptive dissipation. *Monthly weather review 126*(6), 1541–1580.

Shchepetkin, A. F. and J. C. McWilliams (2005). The regional oceanic modeling system (roms): a split-explicit, free-surface, topography-following-coordinate oceanic model. *Ocean modelling 9*(4), 347–404.

Shukla, J. (1981). Dynamical predictability of monthly means. *Journal of the Atmospheric Sciences 38*(12), 2547–2572.

Smith, D. M., S. Cusack, A. W. Colman, C. K. Folland, G. R. Harris, and J. M. Murphy (2007). Improved surface temperature prediction for the coming decade from a global climate model. *science 317*(5839), 796–799.

Soufflet, Y., P. Marchesiello, F. Lemarié, J. Jouanno, X. Capet, L. Debreu, and R. Benshila (2016). On effective resolution in ocean models. *Ocean Modelling 98*, 36–50.

Stevenson, S., B. Rajagopalan, and B. Fox-Kemper (2013). Generalized linear modeling of the el niño/southern oscillation with application to seasonal forecasting and climate change projections. *Journal of Geophysical Research: Oceans*. In press.

Stone, J. V. (2015). *Information theory: a tutorial introduction*. Sebtel Press.

Ullman, D. S. (2019). Hydrodynamic modeling of Narragansett Bay in support of the EcoGEM ecological model. Technical Report GSO No. 2019-01, University of Rhode Island.

Umlauf, L. and H. Burchard (2003). A generic length-scale equation for geophysical turbulence models. *Journal of Marine Research 61*(2), 235–265.

Van Roekel, L., A. J. Adcroft, G. Danabasoglu, S. M. Griffies, B. Kauffman, W. Large, M. Levy, B. G. Reichl, T. Ringler, and M. Schmidt (2018). The kpp boundary layer scheme for the ocean: Revisiting its formulation and benchmarking one-dimensional simulations relative to les. *Journal of Advances in Modeling Earth Systems 10*(11), 2647–2685.

Waldman, R., S. Somot, M. Herrmann, F. Sevault, and P. E. Isachsen (2018). On the chaotic variability of deep convection in the mediterranean sea. *Geophysical Research Letters 45*(5), 2433–2443.

Warner, J. C., C. R. Sherwood, H. G. Arango, and R. P. Signell (2005a). Performance of four turbulence closure models implemented using a generic length scale method. *Ocean Modelling 8*, 81–113.

Warner, J. C., C. R. Sherwood, H. G. Arango, and R. P. Signell (2005b). Performance of four turbulence closure models implemented using a generic length scale method. *Ocean Modelling 8*(1), 81–113.

Watanabe, S. (1960). Information theoretical analysis of multivariate correlation. *IBM Journal of Research and Development 4*(1), 66–82.

Wenegrat, J. O., L. N. Thomas, M. A. Sundermeyer, J. R. Taylor, E. A. D'Asaro, J. M. Klymak, R. K. Shearman, and C. M. Lee (2020). Enhanced mixing across the gyre boundary at the gulf stream front. *Proceedings of the National Academy of Sciences 117*(30), 17607–17614.

Wertman, C. A. (2018). *Circulation & Exchange Within Shelf & Estuarine Waters Driven by the Atmosphere, Tides and Buoyancy*. Ph. D. thesis, University of Rhode Island.

Wilkin, J., J. Levin, A. Lopez, E. Hunter, J. Zavala-Garay, and H. Arango (2018). Coastal ocean forecast system for the us mid-atlantic bight and gulf of maine. *New Frontiers in Operational Oceanography*, 593–624.

Xiu, P., F. Chai, E. N. Curchitser, and F. S. Castruccio (2018). Future changes in coastal upwelling ecosystems with global warming: The case of the california current system. *Scientific reports 8*(1), 2866.

Yettella, V., J. B. Weiss, J. E. Kay, and A. G. Pendergrass (2018). An ensemble covariance

framework for quantifying forced climate variability and its time of emergence. *Journal of Climate 31*(10), 4117–4133.